



TECHNISCHE
UNIVERSITÄT
WIEN
Vienna University of Technology

DISSERTATION

Experimental studies of a Bell-like inequality and a which-way measurement in neutron interferometry

ausgeführt zum Zwecke der Erlangung des akademischen Grades eines
Doktors der technischen Wissenschaften unter der Leitung von

Assistant Prof. Dipl.-Ing. Dr. Yuji Hasegawa

E141 - Atominstitut

eingereicht an der Technischen Universität Wien

Fakultät für Physik

von

Dipl.-Ing. Hermann Geppert-Kleinrath

Matr. Nr. 0426329

Frauenberg 25

A-3500 Krems Stein

Wien, März 2017

Dipl.-Ing. Hermann Geppert-Kleinrath

Abstract

Quantum mechanics introduced new concepts into physics, such as wave-particle duality, contextuality, or the uncertainty relation. Matter-wave experiments are a fruitful approach to investigate the foundations of quantum mechanics. Neutron interferometry especially is a powerful tool for studying quantum mechanical phenomenons. In this thesis two experiments are presented: a measurement of a Bell-like inequality, and a which-way experiment. Prior to the execution of the experiments, improvements of the experimental setup, and newly designed and constructed spin manipulation devices, were implemented. This improved setup allows for more precise measurements. The first measurement shows a clear violation of a Bell-like inequality, and confirms contextual nature of quantum mechanics. It therefore proves, that no contextual hidden variable theory can reproduce all the predictions of quantum mechanics. The second experiment was able to shed light on the question which path the neutrons take in an interferometer. A which-way measurement is presented, utilizing time dependent which-way marking in a double-loop interferometer. Following the time-development of the wavefunction and considering interference terms, between the main components and the marked components of the neutron beam an accurate description of the experiment is given.

Kurzfassung

Durch die Quantenmechanik wurden neue Konzepte in die Physik eingeführt, wie der Welle-Teilchen Dualismus, Quantenkontextualität, oder die Unschärferelation. Für die Untersuchung von fundamentalen quantenmechanischen Effekten sind Masse behaftete Quantenexperimente besonders gut geeignet. Neutroneninterferometrie gilt als ein besonders nützliches Instrument um Quantenphänomenen zu ergründen. In dieser Dissertation werden zwei Experimente vorgestellt: das erste ist eine Messung einer Bellschen Ungleichung, und das zweite ist ein welcher-Weg Experiment. Vor der Durchführung der Experimente wurden Verbesserungen am Versuchsaufbau vorgenommen und neue Spinmanipulatoren konstruiert und gebaut. Dieser verbesserte Versuchsaufbau ermöglicht herheblich genauere Messungen. Das erste Experiment zeigt eine deutliche Verletzung einer Bellschen Ungleichung, wodurch die Quantenkontextualität bestätigt wird und beweist, dass Theorien, basierend auf nicht-kontextuellen versteckten Variablen, die Natur nicht korrekt beschreiben können. Das zweite Experiment befasst sich mit der Frage welchen Weg ein Teilchen in einem Doppelspaltexperiment gegangen ist. Um Informationen über den Weg, den die Neutronen genommen haben, zu bekommen, werden die einzelnen Pfade eines Dreiweginterferometers mit einem zeitabhängigen Signal markiert. Eine theoretische Behandlung des Experiments wird präsentiert, die sich einer zeitlichen Entwicklung der Wellenfunktion bedient. Interferenzterme zwischen den markierten Anteilen und den unmarkierten Hauptanteilen der Wellenfunktion werden genutzt um die Resultate des Experiments präzise vorherzusagen.

Acknowledgments

First, I want to express my deep gratitude towards my supervisor Yuji Hasegawa, and thank him for his thoughtful guidance through this PhD, the important support, and the ideas, which made the experiments of this thesis feasible.

Particular thanks go to my colleagues Stephan Sponar and Tobias Denkmayr, who were always willing to lend a hand. They shared their knowledge and experience, both in theoretical and experimental issues, with me, in fruitful discussions. Thank you for your cheerful mood, even after very long days at the experiment, and for making the time so enjoyable!

I want to thank Hartmut Lemmel, who helped me gain a deeper understanding of neutron interferometry, and for all his support during the experiments at the Institute Laue-Langevin. I want to thank the company Holm GmbH, for their cooperation and dedication to construct the new neutron interferometer.

My parents Gertrude and Ulf Geppert sparked my interest in science. I want to thank them for their constant encouragement and support during my studies.

And finally I want to thank my wife Verena. Thank you for always being there for me!

Contents

1	Introduction	1
1.1	Neutron interferometry	2
2	Elements of neutron optical experiments	7
2.1	Neutron sources	7
2.2	Neutron interferometry	8
2.2.1	Beam splitter; dynamical diffraction at the silicon perfect-crystal plate	9
2.2.2	Triple-Laue neutron interferometer	14
2.2.3	Phase shifter	17
2.2.4	Beam attenuators	19
2.2.5	Neutron detection	19
2.3	Neutron spin and electromagnetic interaction	21
2.3.1	Neutron spin polarization	24
2.3.2	Neutron spin analysis	26
2.3.3	Guide field	28
2.3.4	Larmor accelerators	28
2.3.5	Direct current spin-rotators	30
2.3.6	Resonance-frequency spin-rotator	31
2.3.7	3D printing	33

3	Bell measurement	37
3.1	Introduction	37
3.2	The EPR argument	39
3.3	Bell's inequality	42
3.3.1	Correlation measurements of photons	44
3.3.2	Classical and quantum mechanical correlation measurements of correlated spin-1/2 particles	48
3.3.3	Simple example given for Bell's inequality	50
3.3.4	CHSH-formulation of Bells inequality	52
3.3.5	Bell's inequality for a single spin-1/2 particle and quantum contextuality	54
3.4	Experiment: setup and improvement	56
3.4.1	Measurement concept	58
3.4.2	Setup design	62
	New guide field	64
	Monochromator	67
	New DC spin-rotators	68
3.5	Adjusting the setup	73
3.6	Results	86
3.7	Discussion	89
4	Which-way measurement	91
4.1	Introduction	91
4.2	Theory	94
4.3	Simulation	104
4.4	Preparations for the experiment	107
4.4.1	The new double-loop interferometer	108
	Design of the new double-loop neutron interferometer	108
	Principles of silicon etching	111

Interferometer etching process	113
4.4.2 Time-resolved measurement	119
4.5 Experiment realisation	122
4.6 Data analysis and results	132
4.7 Discussion	139
5 Conclusion and outlook	143
Bibliography	145
Curriculum Vitae	157

Chapter 1

Introduction

Quantum mechanics is probably the best verified physical theory, from an experimental point of view [Wheeler and Zurek, 1983, Sakurai, 1993, Haroche and Raimond, 2006]. From the emergence of quantum mechanics in the early 20th century up to this day numerous novel theoretical predictions were made and still are made, based on the frame work of quantum mechanics. Continuous test of these predictions using a variety of different quantum systems are essential for their experimental verification, which often led to practical and everyday application [Wilton, 2014].

Quantum mechanics introduced new physical concepts like the wave-particle duality, the probabilistic description of nature and the uncertainty relation. The famous debate between Bohr and Einstein is a pinnacle point for understanding the implications made by quantum mechanics [Bohr, 1949]. The wave-particle duality is best illustrated by the double-slit experiment, where interference fringes become visible on a screen in an appropriate distance to the double slit, which is a consequence the wave-nature of quantum mechanics. However, for every particle passing through the double-slit only one count is detected at a distinct location, which is the particle-nature of quantum mechanics. The Mach-Zehnder interferometer demonstrates the wave-particle dualism in a similar manner: A particle passes through two

spatially separated paths and can leave the interferometer in two different directions. Depending on the phase induced between the two paths the particle is detected only in one of the two outgoing paths. By altering the induced phase intensity modulations are visible at the outgoing beams, i.e. interference fringes.

Matter wave interferometry has proven to be a very capable and versatile tool to investigate the foundations of quantum mechanics. Countless experiments, using different measurement systems, such as neutrons, electrons, atoms, and even molecules, have been accomplished [Davisson and Germer, 1927, Jönsson, 1961, Rauch et al., 1974, Arndt et al., 1999]. By entangling particles or different degrees of freedom, e.g. polarization, spin, and energy, in an interferometer, fundamental aspects of quantum mechanics can be illuminated, such as quantum contextuality and weak values.

1.1 Neutron interferometry

Perfect-crystal neutron interferometry, introduced in 1974 by Rauch, Treimer and Bonse [Rauch et al., 1974], together with spin polarimetry has proven to be a very suitable tool for investigating fundamental quantum mechanics [Rauch and Werner, 2000, Hasegawa and Rauch, 2011, Klepp et al., 2014]. Since neither matter-wave interferometry nor spin-1/2 particles have a classical analogue, polarized neutron interferometry is a purely quantum mechanical system. Both the spin and the path state can be manipulated with high precision using devices as described in section 2. The large beam separation of usually about 50 mm allows for deployment of various neutron manipulation devices. To illustrate the wide range of application of neutron interferometry, several important measurements are presented below.

Right after the first successful test of neutron interferometry a very fundamental property of spin-1/2 particles was tested i.e. the first experimental

investigation of the 4π spinor symmetry [Rauch et al., 1975]. The wave function of a spin-1/2 particle under a rotation 2π gives $\psi(2\pi) = -\psi(0)$, this phase factor of $e^{i\pi}$, while predicted theoretically, was considered inaccessible and some how artificial. Only after a rotation of 4π the wave function is in the same state as initially $\psi(4\pi) = \psi(0)$. When a neutron beam passes a region where the magnetic field \vec{B} is applied, the neutron spin is rotated by an angle of

$$\alpha = \frac{2\mu}{\hbar} \int B dt, \quad (1.1)$$

with the magnetic moment μ . By applying a magnetic field in one path of the interferometer using an electromagnet and using the second path as reference the phase shift induced by the magnetic field can be observed. Surprisingly there is no polarized beam needed for this experiment, since both up-spin and down-spin component of the neutron beam obtain the same phase under rotation. The observation of the 4π -symmetry was first accomplished in 1975 using perfect-crystal neutron interferometry showing good agreement with theoretical predictions. Later on another experiments on 4π -symmetry using neutrons were successfully performed [Klein and Opat, 1976, Grigoriev et al., 2004].

Another interesting experiment deals with a non intuitive effect when one of the beams in the interferometer is reduced in intensity by absorption [Summhammer et al., 1987]. When the transmission in one path is reduced, the visibility of the interference fringes is reduced as well. At the point when the transmission reaches zero no interference fringes are visible any more. The way the absorption is accomplished is crucial to the outcome of the experiment. Quantum mechanical predictions for the visibility of the interference fringes differ whether stochastic or deterministic absorption is used. In the case of deterministic absorption (e.g. chopper with variable open/block ratio), one can tell where or when the neutron is absorbed, while

in the stochastic case (e.g. absorbing foil) the amplitude of the beam is reduced. The visibility in the deterministic case is proportional to the transmission T_d in respective beam, while in the stochastic case the visibility scales with $\sqrt{T_s}$. This can be seen in the intensity

$$\begin{aligned} I_{Det} &\propto |\psi|^2 \left[1 + T_d + 2T_d \cos(\chi) \right] \\ I_{Sto} &\propto |\psi|^2 \left[1 + T_s + 2\sqrt{T_s} \cos(\chi) \right], \end{aligned} \quad (1.2)$$

with χ being the phase shift between the paths induced by a phase shifter. The square root relation between transmission and visibility is remarkable especially at very low transmissions, which result in quite large interference patterns. For example a transmission of $T_s = 0.01$ results in a amplitude of the interference fringes of 0.1.

The use of a polarized neutron beam in neutron interferometry opened up a new era of experimental capabilities. For example spin superposition was investigated using polarized neutron interferometry [Summhammer et al., 1983]. This was experimentally realized by a neutron beam, polarized in positive z-direction (up-spin), entering the interferometer. In one path the spin is flipped into the negative z-direction (down-spin) at the third plate the beams are recombined. The resulting state is not a incoherent mixture of up-spin and down-spin, but a new coherently superposed spin state

$$|\psi\rangle = \frac{1}{\sqrt{2}} \left(|s_+\rangle + e^{i\chi} |s_-\rangle \right), \quad (1.3)$$

in the xy-plane. In forward direction the neutron beam is spin-analyzed in x-direction. When the phase χ between the paths is changed spin rotation is visible. The beam in reflected direction is not spin analyzed and does not show interference fringes when the phase χ is altered, which is a result of the orthogonal spin state. This experiment can also be accomplished using a resonance-frequency spin-flipper and stroboscopic measurement of the spin analyzed beam [Badurek et al., 1983].

The total phase induced during the evolution of a quantum system consists of two components a dynamical phase and a geometric phase. The peculiarity of the geometric phase, introduced by Berry in 1984 [Berry, 1984], is that it deepens purely on the evolution path of the state, and not on the dynamics of the system. The acquired phase is proportional to minus the half of the solid angles enclosed by the evolution path $\phi = -\Omega/2$. This geometric phase was observed in neutron interferometric experiments [Hasegawa et al., 2001, Filipp et al., 2005, Filipp et al., 2009, Sponar et al., 2010]

Recently weak value measurements have been performed successfully. The concept of weak measurements was introduced by Aharonov, Albert, and Vaidman in 1988 [Aharonov et al., 1988]. The weak value allows to extract information about a quantum system between pre-selection and post-selection, and is defined as

$$\langle A \rangle_w = \frac{\langle \psi_f | A | \psi_i \rangle}{\langle \psi_f | \psi_i \rangle}. \quad (1.4)$$

This measurement scheme was used successfully in neutron interferometry to observe the quantum Cheshire cat [Denkmayr et al., 2014], spin weak values [Sponar et al., 2015], and the quantum pigeonhole effect [Waegell et al., 2017].

Many different experiments have been successfully executed, which tested the very foundations of quantum mechanics since the introduction of neutron interferometry. Such as the gravitational phases in the neutron interferometer (COW) [Colella et al., 1975]. The Aharonov-Bohm and the Aharonov-Casher effect [Aharonov and Bohm, 1959, Aharonov and Casher, 1984] have been experimental confirmed [Werner and Klein, 2010, Lee et al., 1998]. Measurements of confinement induced phases [Rauch et al., 2002] have been performed, as well as entanglement between three different degrees of freedom [Hasegawa et al., 2010, Erdösi et al., 2013].

Chapter 2

Elements of neutron optical experiments

In this chapter we describe neutron sources, the function of the neutron interferometer, how spin-polarization and spin-analyzation are accomplished, as well as how the spin-manipulation is performed. Newly built spin-manipulation devices are presented, which are produced utilizing 3D-printing.

2.1 Neutron sources

A free neutron has a lifetime of ~ 880 s, consequentially free neutrons need to be produced on demand by extracting them from heavy atomic nuclei. The main ways to generate free neutrons are fusion as used in neutron generators or fission as used in spallation sources and nuclear reactors. Neutron generators are small devices generating a low neutron flux by accelerating and fusing hydrogen, deuterium or tritium into helium and free neutrons. Spallation sources provide neutrons by accelerating protons and shooting them on a target consisting of elements with high atomic weight, e.g. tungsten, prompting neutron emission. Neutron generators and spallation sources are

not suitable for neutron optical experiments since the first has too low flux and the latter provides high intensity neutron pulses, but not a constant neutron flux.

The third type of neutron source is the nuclear reactor. The high flux reactor at the Institut Laue-Langevin (ILL) in Grenoble, France is used as neutron source for the experiments presented in this thesis. The reactor at the ILL uses only one highly enriched fuel element with one control rod in the center of it. This allows for very high neutron flux of $1.5 \times 10^{15} \text{ cm}^{-2}\text{s}^{-1}$, since the neutrons are produced in a very small volume, i.e. a small source size, in respect to the thermal power of 58 MW. The produced neutrons are moderated to thermal energy and guided via neutron guides to the neutron interferometer instrument S18. The count rates in polarized neutron interferometry are in the order of $10^2 \text{ cm}^{-2}\text{s}^{-1}$ typically.

2.2 Neutron interferometry

The perfect-crystal neutron interferometer for thermal neutrons is a Mach-Zehnder-like interferometer. A scheme of a optical Mach-Zehnder interferometer is shown in Fig.2.1. The incoming beam is split up into two paths at the beam-splitter (BS). The mirrors reflect the beams towards a beam-analyzer (BA). A phase-shifter tunes the phase between the two paths. The two beams are recombined at the beam-analyzer and passed on into two directions. One direction is parallel to the incoming beam and ends up at the O-detector, the second ends up at the H-detector. By tuning the phase between the two paths the intensity can be divided between the two detectors. From the intensity measured at the detectors the relative phase of the interfering beams can be determined.

Perfect crystal neutron interferometry was first accomplished by Rauch, Treimer, and Bonse [Rauch et al., 1974] [Rauch and Werner, 2000] at the

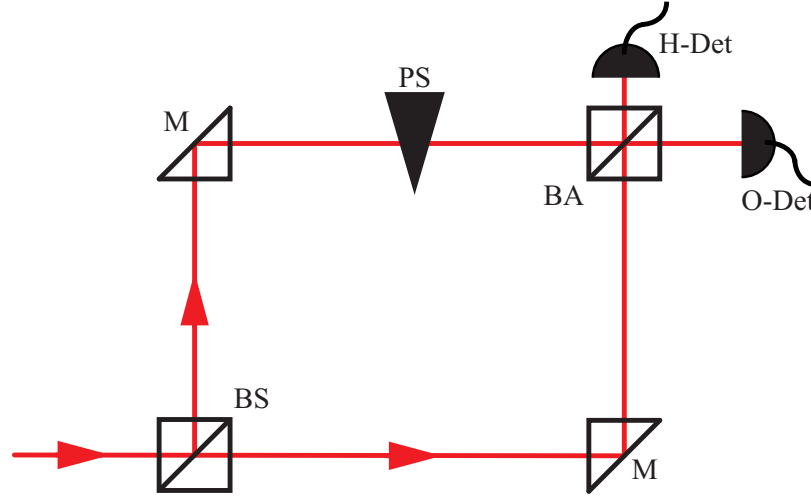


Figure 2.1: Scheme of an optical Mach-Zehnder interferometer, consisting of a beam-splitters (BS), two mirrors (M), a phase-shifter (PS), beam-analyzer (BA), and two detectors (O-Det and H-Det).

TRIGA Mark II research reactor at the Atominstitut at the Technische Universität Wien, in Vienna. It is constructed out of a single rod of a silicon perfect crystal, with a monolithic structure, which is cut into the shape of the interferometer. The interferometer has three parallel plates which are equally distanced and connected through a base as seen in Fig.2.2.

2.2.1 Beam splitter; dynamical diffraction at the silicon perfect-crystal plate

Each plate of the perfect-crystal neutron interferometer acts in principle as a beam splitter and divides each incoming beam into a transmitted beam and a reflected beam on the other side of the plate, by Laue-case diffraction. The two outgoing beams enclose an angle of twice the Bragg angle $2\theta_B$ to the incoming beam. This is depicted in Fig.2.3a. In contrast the Bragg-case diffraction (Fig.2.3b) where the refraction planes are parallel to the surface of

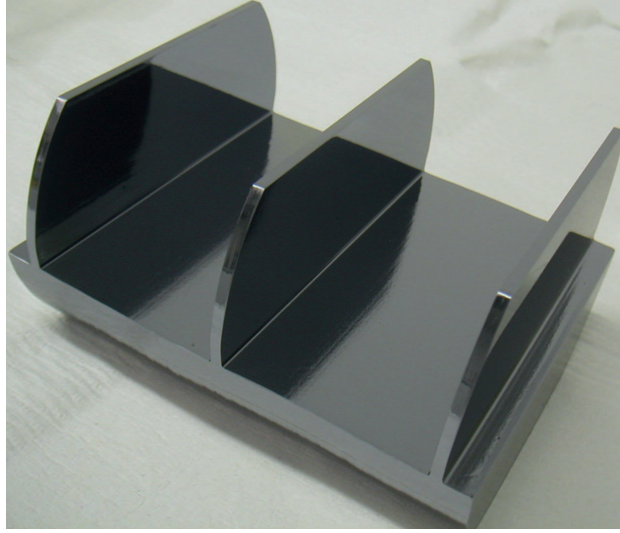


Figure 2.2: Picture of a triple Laue interferometer made out of a single silicon perfect-crystal. The overall length of this interferometer is 123 mm.

the crystal, Laue-case diffraction uses a crystal orientation with the reflection planes perpendicular to the surface of the crystal. Note that in the Bragg case total reflection of the neutron beam occurs while in the Laue case two beams emerge behind the crystal. Only the Laue case can be sufficiently used as a 50:50 beam splitter. The perfect crystal silicon interferometer is also referred to as a triple Laue (LLL) interferometer, because of the orientation of the three crystal planes. The reflection plane used in the presented experiments is the (2,2,0) crystal plane and a diffraction angle θ_B of 30 deg or $\theta_B = \pi/6$. The wave length λ of the neutrons can be calculated using Braggs law

$$n\lambda = 2d_{hkl} \sin(\theta_B), \quad d_{hkl} = \frac{d_0}{\sqrt{h^2 + k^2 + l^2}}, \quad (2.1)$$

with a lattice constant of silicon of $d_0 = 5.43 \cdot 10^{-10}$ m, and the Miller indexes $h = 2$, $k = 2$, and $l = 0$. This results in a neutron wave length of 1.92 Å. Suppose that the incoming beam is given by a plane wave

$$|\psi_{in}\rangle = A_{in} e^{i\vec{k}\vec{r}}, \quad (2.2)$$

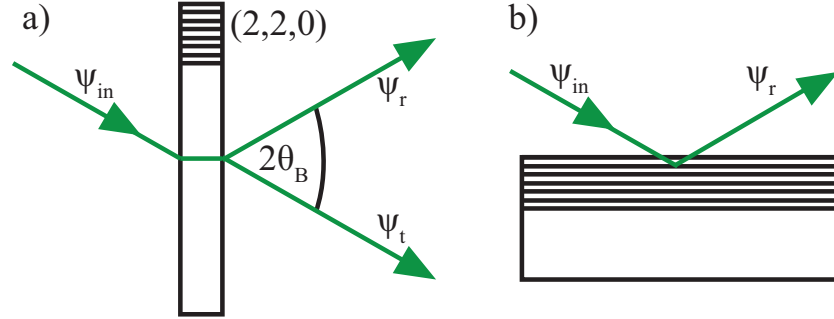


Figure 2.3: a) Depiction of a Laue-case diffraction beam splitter. The incoming wave function ψ_{in} is split up into a transmitted wave function ψ_t and a wave function ψ_r reflected from the $(2,2,0)$ crystal plane. b) Scheme of the Bragg-case diffraction with a incoming beam ψ_{in} and a reflected beam ψ_r .

with its position \vec{r} , momentum vector \vec{k} and amplitude A_{in} . Behind the beam splitter two wave functions are present

$$\begin{aligned} |\psi_t\rangle &= A_t e^{i\vec{k}\vec{r}} \\ |\psi_r\rangle &= A_r e^{i\vec{k}'\vec{r}}, \end{aligned}$$

with the wave vector of the reflected beam given by $\vec{k}' = \vec{k} + \vec{H}$, where \vec{H} is the reciprocal lattice vector corresponding to the $(2,2,0)$ crystal plane. A scheme of the vectors \vec{k} , \vec{k}' , and \vec{H} is given in Fig.2.4. This is why the beams leaving the interferometer at the third plate are referred to as the O-beam which is parallel to the incoming beam and the H-beam, which differs in direction by the reciprocal lattice vector \vec{H} to the incoming beam. It is worth noting that the transmitted wave function gets a phase shift of 0, while the reflected wave function gets a phase shift of π . For simple description of a perfect 50 : 50 beam splitter the amplitudes fulfill the relation

$$|A_t| = |A_r| = \frac{1}{\sqrt{2}} |A_{in}|. \quad (2.3)$$

However, the inevitable divergence of the angle of the incoming beam of

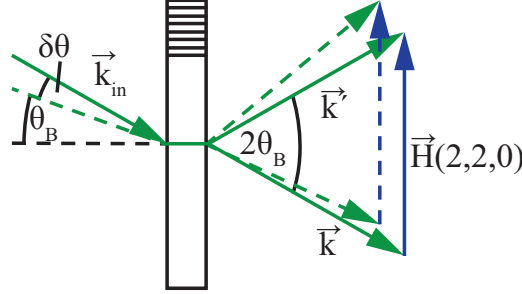


Figure 2.4: Depiction of the wave vectors \vec{k} , and \vec{k}' as well as the reciprocal lattice vector \vec{H} . A deviation $\delta\theta$ from the Bragg angle θ_B is depicted.

$\theta = \theta_B + \delta\theta$ needs to be taken into account as depicted in Fig.2.4. The deviation angle is expressed using the dimensionless parameter

$$y = \frac{\Delta_0 k}{\pi} \delta\theta \sin(\theta_B), \quad (2.4)$$

with the Pendellösungslänge $\Delta_0 = 68 \mu\text{m}$ for $\lambda = 1.92 \text{ \AA}$. When the parameter y is taken into account the amplitudes behind the beam splitter become functions of y , with the amplitude $t(y)$ for the transmitted beam, and the amplitude $r(y)$ for the reflected beam. The intensities behind the beam splitter as a function of y is given by

$$I_H = |r(y)|^2 = 1 - \frac{\sin^2 \left(B \sqrt{1 + y^2} \right)}{(1 + y^2)} \quad (2.5)$$

$$I_O = |t(y)|^2 = \frac{\sin^2 \left(B \sqrt{1 + y^2} \right)}{(1 + y^2)},$$

with B being the crystal thickness. In Fig.2.5 the intensities for the O-beam and the H-beam are plotted in dependence of y , and for different crystal thicknesses B given in multiples of the Pendelösungslänge Δ_0 . The intensity oscillates of the O-beam and the H-beam, as a function of y , for different thickness of the beam splitter. Only for crystal plates much thicker than the Pendelösungslänge Δ_0 the plate acts as a 50 : 50 beam splitter.

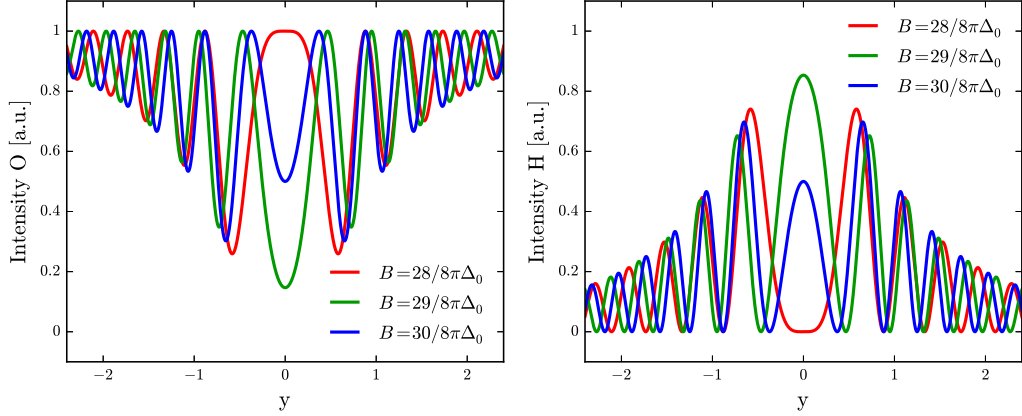


Figure 2.5: Plot of the intensity in dependence of the deviation y to the Bragg angle θ_B for the O-beam on the left and the H-beam on the right for different thicknesses B of the crystal plate.

The beam inside the crystal can be reflected several times as depicted in Fig.2.6, resulting in the Borrmann triangle, which is the space between the points A , B , and C . The point A is the position on the plate where the beam enters the crystal. Points B and point C are the furthestmost points the neutron beam can reach. The Borrmann triangle results in a widening of the beam at each plate of the interferometer by the thickness of the plate, for a Bragg-angle of $\theta_B = \pi/6$, as used in the experiment, since the neutrons can reach every position between point B and C . The angle Ω defines the point of exit of the beam and is used for the definition of the dimensionless parameter

$$\Gamma \equiv \frac{\tan(\Omega)}{\tan(\theta_B)}, \quad (2.6)$$

with $\Gamma = -1$ corresponds to point B and $\Gamma = 1$ corresponds to point C . The

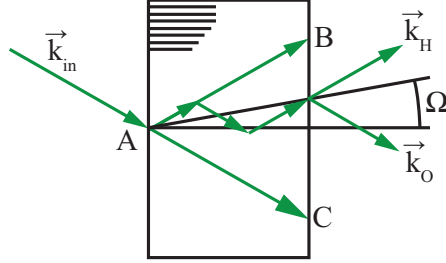


Figure 2.6: The Borrmann triangle spans between the point of incident A of the wave function, and points B and C , the furthest points the wave function is present. The angle Ω defines of the point of exit of the outgoing beams in direction parallel to the incident beam \vec{k}_o , and reflected direction \vec{k}_H .

intensity of the outgoing beams is given by

$$I_O = \frac{1 - \Gamma}{1 + \Gamma} \mathcal{J}_1^2 \left(\frac{\pi B}{\Delta_0} \sqrt{1 - \Gamma^2} \right)$$

$$I_H = \mathcal{J}_0^2 \left(\frac{\pi B}{\Delta_0} \sqrt{1 - \Gamma^2} \right),$$

with the Bessel functions \mathcal{J}_i , and Γ is in the range $-1 < \Gamma < 1$ [Suda, 2005, Lemmel, 2006]. The intensity distributions are shown in Fig.2.7. This is a lateral intensity distribution, in contrast to the angular distribution caused by the deviation $\delta\theta$ from the Bragg-angle of the incident beam, as discussed above.

2.2.2 Triple-Laue neutron interferometer

By combining three equidistant Laue-case beam splitter of equal thickness, one can build a Mach-Zehnder-like triple-Laue interferometer. In Fig.2.8 a scheme of the interferometer with an inserted phase shifter (PS) is depicted. The beam (green arrows) propagate through the interferometer and get transmitted (t) or reflected (r) at each plate respectively. Analogous to the optical

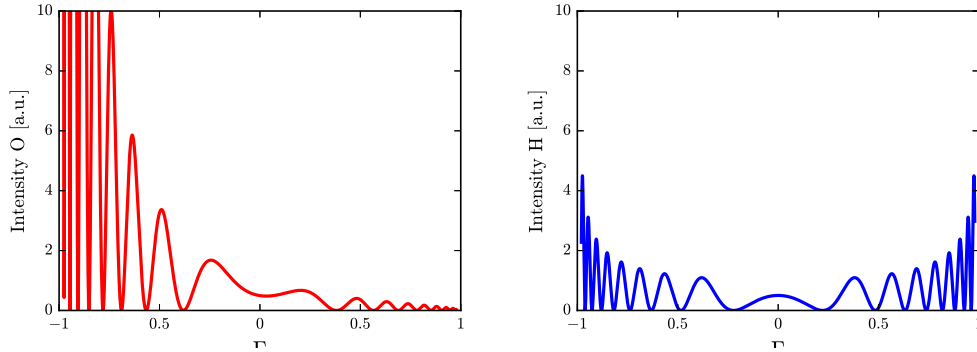


Figure 2.7: Plot of the intensity in the Borrmann triangle in dependence of Γ for the O-beam on the left and the H-beam on the right. The position in the graph for parameter $\Gamma = -1$ corresponding to point B, while $\Gamma = 1$ corresponds to point C in Fig. Fig.2.6.

interferometer the three plates of the neutron interferometer are referred to as beam splitter (BS), mirror (M), and beam analyzer (BA). The mirror of course acts as a beam splitter too and produces two outgoing beams, which are not of use and blocked by beam blockers (BB). The beam parallel to the incoming beam ends up at the O-detector, the beam in the reflected direction ends up at the H-detector. The neutrons can take two paths to end up at either the O-detector or the H-detector. The lower path is referred to as path I while the upper path is referred to as path II. The wave functions at the detectors are composed out of components coming from both paths and are given by

$$\begin{aligned}\psi_O &= (trr + rrt e^{i\chi}) e^{i\vec{k}\vec{r}} \\ \psi_H &= (trt + rrr e^{i\chi}) e^{i\vec{k}'\vec{r}},\end{aligned}$$

with the phase shift of χ induced by the phase shifter. Note that the beams ending up at the O-detector are both reflected twice and transmitted once, while the beam ending up at the H-detector is composed of one beam which is transmitted twice and reflected once and a second beam being reflected

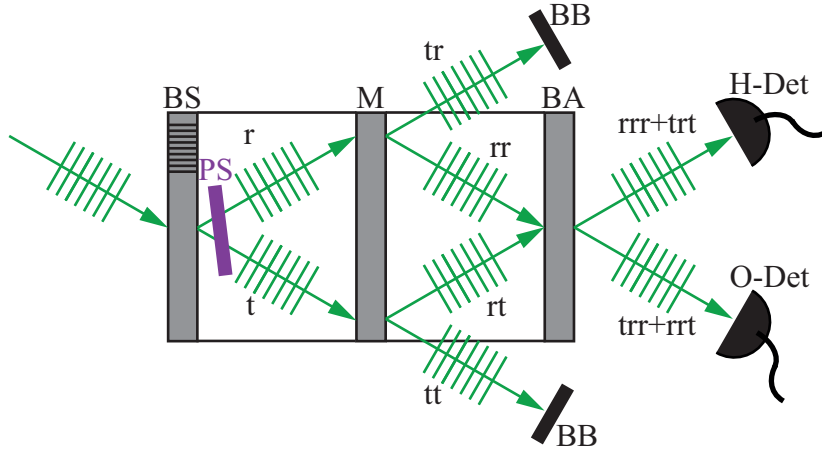


Figure 2.8: Beams of a perfect crystal neutron interferometer, passing through a beam-splitter plate (BS), a mirror plate (M), a beam-analyzer plate (BA), a phase-shifter (PS), and arriving at two detectors (O-Det and H-Det). The neutron beam is represented by the green arrows with crossbars representing the plane waves of the neutrons. Two beam blockers (BB) block beams going out of the interferometer, which are not of use. Each plate produces a transmitted (t) and a reflected (r) beam for each incoming beam.

three times. By calculating the intensities for each path, accounting for the beam divergence and the intensity profile caused by the Borrmann triangle, it can be shown, that only the O-beam can show full contrast, while the H-beam can not [Rauch and Suda, 1974]. The O-beam will only show full contrast if every plate is a perfect 50 : 50 beam splitter of equal thickness and equal spacing between the plates.

The neutron interferometer is very sensitive to external disturbances like vibration, temperature changes over time, or temperature gradients within the interferometer caused by external heat sources, as described in section 3.4. The interferometer is placed on a vibration damping optical bench in an insulated and temperature stabilized experiment chamber.

2.2.3 Phase shifter

The phase shifter induces a relative phase between the beams in the interferometer. The phase shifter is a slab of material which has a low absorption cross section such as silicon Si, aluminium Al, or sapphire Al_2O_3 . The faces of the phase shifter need to be smooth and parallel to avoid dephasing. Due to the optical potential of a material the neutrons path through a phase shift occurs. The phase shift χ is given by

$$\chi = (n - 1)kD = -Nb_c\lambda D, \quad (2.7)$$

with n is the refraction index, k is the wave vector, and D is the thickness of the slab, N being the atomic density, b_c the nuclear scattering length, and λ the wave length of the neutrons. When the phase shifter is placed

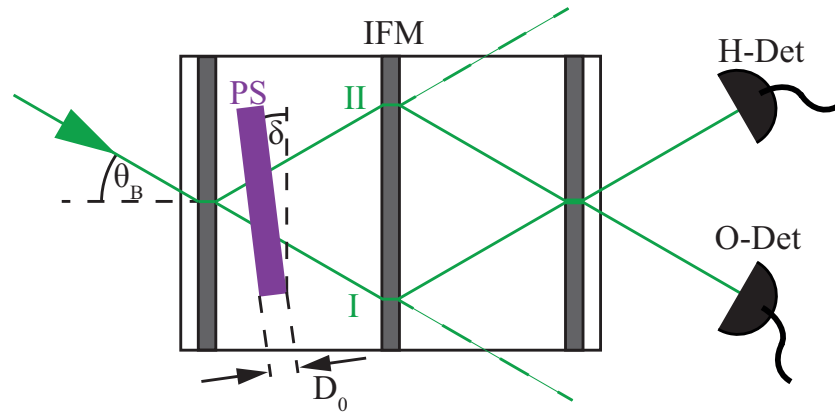


Figure 2.9: Scheme of the interferometer with a phase shifter inserted. The Bragg angle θ_B , the angle of the phase shifter δ , and the thickness of the phaseshifter D_0 are depicted.

in the interferometer as depicted in Fig.2.9 and rotated by an angle of δ , the neutrons in the two paths experience a relative phase shift due to the

different of the optical path length through the material, given by

$$\Delta D = \left[\frac{1}{\cos(\theta_B + \delta)} - \frac{1}{\cos(\theta_B - \delta)} \right] D_0, \quad (2.8)$$

with the Bragg angle θ_B , and δ being the angle between the phase shifter and the plates of the interferometer. The resulting phase shift is given by

$$\Delta\chi = -Nb_c\lambda\Delta D. \quad (2.9)$$

When the phase shifter encloses a small angle of rotation δ to the interferometer plates, the phase shift can be linear approximated $\Delta\chi \propto \delta$. In figure Fig.2.10 a comparison between the exact calculation of ΔD_{exact} , and a linear approximation with $\Delta D_{app}(\delta) = 4\delta/3$ is depicted. For typical phase shifter rotation angles of ~ 1 deg, as used in the experiment, the error of the linear approximation is $0.4 \cdot 10^{-3}$.

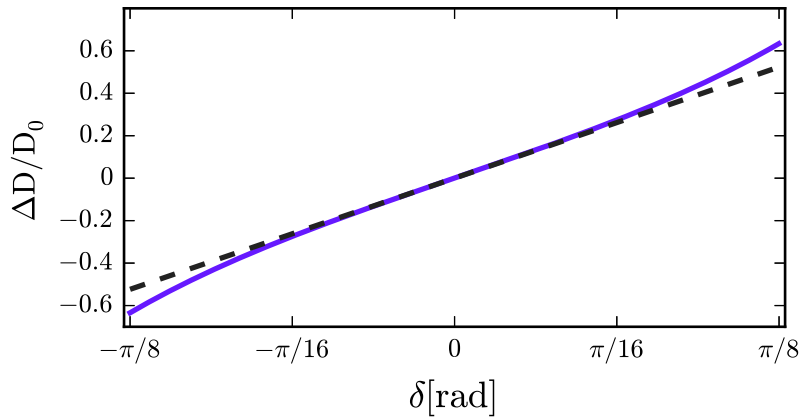


Figure 2.10: Comparison between the exact calculation of $\Delta D_{exact}(\delta)$ (purple line) using equation 2.8, and a linear approximation $\Delta D_{app}(\delta) = 4\delta/3$ (dashed gray line).

It is important to point out that the interferometer is very sensitive to material which is put into the beam path within the interferometer. If material is put into the neutron beam with a rough surface, uneven thickness, or

irregular composition the neutron beam receives different amounts of phase shift within the beam cross section, which leads in turn to reduced or vanishing interference effect.

2.2.4 Beam attenuators

Beam attenuators are used to reduce the neutron intensity in one path of the interferometer. In the which-way experiment described in chapter 4 beam attenuators are used to reduce the effect of a reference beam on the system probed by the reference beam. The transitivity T of an beam attenuator of thickness D , absorption cross section σ_{abs} , and atomic density N can be calculated using the Beer-Lambert law [Beer, 1852]

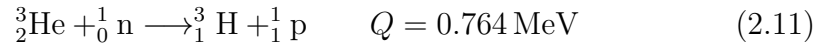
$$T = \frac{I_t}{I_i} = e^{-N\sigma_{abs}D}. \quad (2.10)$$

With I_i being the incoming neutron intensity and I_t being the transmitted neutron intensity. Cadmium is used to block a neutron beam because of its high absorption cross section of 2520 b, which results in an absorption coefficient of $N\sigma_{abs} = 12 \times 10^3 \text{ m}^{-1}$ and a transitivity of $T = 4 \times 10^{-6}$ for a 1 mm thick Cadmium slab. A slab of Indium with a thickness of 1 mm and an absorption cross section 785 b, which results in a transitivity of $T = 0.456$, is used for the which-way experiment presented in chapter 4. The scattering cross section is neglected in this calculation. This is justified by the small contribution of the scattering cross section for these two materials of less the 1% of the absorption cross section.

2.2.5 Neutron detection

The detectors used at the neutron interferometer instrument S18 are ^3He counter tubes. Since the neutron is not electrical charged it does not produce any electrical signal when passing through the detector. A conversion process

is needed to produce a detectable electrical signal in the detector. The ${}^3\text{He}$ counter tube is based on the nuclear reaction



The neutrons are absorbed by ${}^3_2\text{He}$, which then decays into triton (${}^3_1\text{H}$) and a

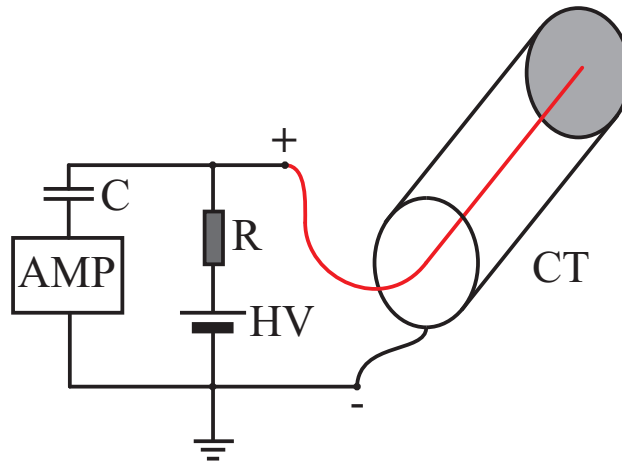


Figure 2.11: Scheme of counter tube and connected electronics. A high voltage source (HV) supplies the counter tube (CT). The intrinsic resistance is represented by R . The capacity (C) is put in front of the signal amplifier (AMP).

proton (${}^1_1\text{p}$). The energy yield of this reaction of 0.764 MeV is divided on the decay products. Due to the high absorption cross section of ${}^3_2\text{He}$ of 5333 b the efficiency of the detector is very high. The decay products ionize the gas in the counter tube. High voltage of about $\sim 1200 \text{ V}$ is applied between the housing of the tube and a wire in the middle of it, as depicted in Fig.2.11. Due to electric field applied, the electrons are accelerated to the wire and secondary ionization takes place. When the electrons are collected there is a small electrical pulse which passes through a capacity to an amplifier. The amplifier produces a square signal which is forwarded to the data acquisition system. The ${}^3\text{He}$ counter tube is insensitive to gamma radiation, but it

must be shielded against scattered background neutrons. This is achieved by putting neutron absorbing material as a shielding around the detector, such as Cadmium or borated paraffin wax.

2.3 Neutron spin and electromagnetic interaction

Neutrons have an intrinsic magnetic moment called spin. The spin vector is related to magnetic moment $\vec{\mu}_n$ of magnitude $|\vec{\mu}_n| = 9.65 \cdot 10^{-27}$ J/T and the gyro magnetic factor $\gamma = -1.8301 \cdot 10^8$ rad s⁻¹T⁻¹ [Abele, 2008] via the relation

$$\vec{S} = \frac{\vec{\mu}_n}{\gamma}. \quad (2.12)$$

The spin vector can be written in terms of expectation values of the Pauli spin operators $\langle \hat{\sigma}_i \rangle$ [Mezei, 1972] and the reduced Planck constant \hbar

$$\vec{S} = \frac{\hbar}{2} \begin{pmatrix} \langle \hat{\sigma}_x \rangle \\ \langle \hat{\sigma}_y \rangle \\ \langle \hat{\sigma}_z \rangle \end{pmatrix}. \quad (2.13)$$

The factor 1/2 above derive from the property of the neutron being a spin-1/2 particle. Subsequently resulting in the 4π -periodicity of the wave function as first shown by Rauch et al. [Rauch et al., 1975]. The three Pauli spin matrices $\hat{\sigma}_i$ are given by

$$\hat{\sigma}_x = \begin{pmatrix} 0 & 1 \\ 1 & 0 \end{pmatrix}, \hat{\sigma}_y = \begin{pmatrix} 0 & -i \\ i & 0 \end{pmatrix}, \hat{\sigma}_z = \begin{pmatrix} 1 & 0 \\ 0 & -1 \end{pmatrix}. \quad (2.14)$$

The Pauli spin matrices can be expressed via a two dimensional standard vector base

$$\begin{aligned}
 |s_{x+}\rangle &= \frac{1}{\sqrt{2}} \begin{pmatrix} 1 \\ 1 \end{pmatrix}, & |s_{y+}\rangle &= \frac{1}{\sqrt{2}} \begin{pmatrix} 1 \\ i \end{pmatrix}, & |s_{z+}\rangle &= \begin{pmatrix} 1 \\ 0 \end{pmatrix}, \\
 |s_{x-}\rangle &= \frac{1}{\sqrt{2}} \begin{pmatrix} 1 \\ -1 \end{pmatrix}, & |s_{y-}\rangle &= \frac{1}{\sqrt{2}} \begin{pmatrix} 1 \\ -i \end{pmatrix}, & |s_{z-}\rangle &= \begin{pmatrix} 0 \\ 1 \end{pmatrix},
 \end{aligned}$$

as

$$\begin{aligned}
 \hat{\sigma}_x &= |s_{x+}\rangle\langle s_{x+}| + |s_{x-}\rangle\langle s_{x-}| \\
 \hat{\sigma}_y &= i(|s_{y+}\rangle\langle s_{y+}| - |s_{y-}\rangle\langle s_{y-}|) \\
 \hat{\sigma}_z &= |s_{z+}\rangle\langle s_{z+}| - |s_{z-}\rangle\langle s_{z-}|.
 \end{aligned}$$

The Hamiltonian for a neutron with a mass of $m_n = 1.6749 \cdot 10^{-27}$ kg interacting with a magnetic field $\vec{B}(\vec{r}, t)$ is given by

$$\hat{H}_B = -\frac{\hbar}{2m} \nabla^2 - \vec{\mu} \vec{B}(\vec{r}, t) = -\frac{\hbar}{2m} \nabla^2 - \frac{1}{2} \hbar \gamma \vec{\sigma} \vec{B}(\vec{r}, t). \quad (2.15)$$

The solution of the Schrödinger equation

$$i\hbar \frac{\partial}{\partial t} \psi(\vec{r}, t) = \hat{H}_B \psi(\vec{r}, t), \quad (2.16)$$

can be written using $\psi = \psi_r \cdot \psi_s$, where ψ_r is the space dependent part and ψ_s the spin dependent part, as

$$\psi(\vec{r}, t) = \left(c_+ \cos\left(\frac{\theta}{2}\right) |s_{z+}\rangle + c_- \sin\left(\frac{\theta}{2}\right) e^{i\phi} |s_{z-}\rangle \right) \psi_r, \quad (2.17)$$

with the polar angle θ and the azimuth angle ϕ of the spin polarization vector on the Bloch-sphere, as seen in Fig.2.12.

The coefficients c_+ and c_- are weighting coefficients, which become 1 for a spin eigenstate $|s_{z\pm}\rangle$. When an external magnetic field \vec{B} interacts with the neutron spin a change in direction of the spin vector \vec{S} perpendicular to

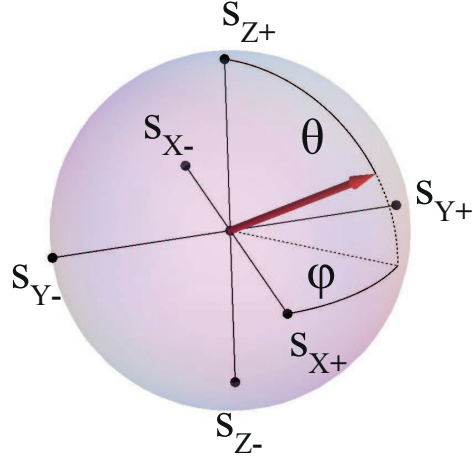


Figure 2.12: Representation of spin polarization vector for the polar angle θ , and the azimuth angle ϕ on the Bloch sphere.

the field and the spin direction appears

$$\frac{d\vec{S}}{dt} = \gamma\vec{S} \times \vec{B} = \vec{S} \times \vec{\omega}_L, \quad (2.18)$$

with $\vec{\omega}_L = \gamma\vec{B}$, being the Larmor frequency. The spin vector precesses around the external field at a frequency of ω_L . The action of a constant magnetic field \vec{B} acting for a duration of τ on a spin state can be expressed as a unitary transformation $\hat{U}(\vec{\alpha})$, with $\vec{\alpha} = \alpha\vec{n}$ being the rotation angle given by $\vec{\alpha} = 2\mu\vec{B}\tau/\hbar$, by

$$\hat{U}(\vec{\alpha}) = \cos\left(\frac{\alpha}{2}\right)\mathbb{1} - i\vec{n}\vec{\sigma}\sin\left(\frac{\alpha}{2}\right). \quad (2.19)$$

Which results for x, y, and z directions in the unitary rotation matrices:

$$\begin{aligned}\widehat{U}_x(\alpha) &= \begin{pmatrix} \cos\left(\frac{\alpha}{2}\right) & -i\sin\left(\frac{\alpha}{2}\right) \\ -i\sin\left(\frac{\alpha}{2}\right) & \cos\left(\frac{\alpha}{2}\right) \end{pmatrix} \\ \widehat{U}_y(\alpha) &= \begin{pmatrix} \cos\left(\frac{\alpha}{2}\right) & -\sin\left(\frac{\alpha}{2}\right) \\ \sin\left(\frac{\alpha}{2}\right) & \cos\left(\frac{\alpha}{2}\right) \end{pmatrix} \\ \widehat{U}_z(\alpha) &= \begin{pmatrix} e^{-i\alpha/2} & 0 \\ 0 & e^{i\alpha/2} \end{pmatrix}\end{aligned}\tag{2.20}$$

Every spin rotation which can be achieved in a neutron experiment can be constructed out of this rotation matrices.

2.3.1 Neutron spin polarization

The beam produced by the neutron source is unpolarized i.e. all spin directions are equally likely. If a spin measurement is performed along any direction half of the neutrons would be aligned parallel the other half anti parallel to the direction of measurement. For measurements utilizing the neutrons spin, the neutrons usually need to be spin-polarized. The degree of polarization is an important parameter of the used setup and is defined as

$$P = \frac{|N_+ - N_-|}{N_+ + N_-},\tag{2.21}$$

with N_+ being the number of neutrons aligned parallel and N_- the number of neutrons anti-parallel to the measurement direction.

The spin polarization can be achieved by two spin-dependent birefringent magnetic prisms in front of the interferometer, as done in the presented experiments. The prisms are permanent magnetic yolks, that produce a triangular shaped magnetic field in z-direction in a small gap, the neutrons can pass. The prisms refract the up-spin component s_{z+} and the down-spin component s_{z-} by a different angle as seen in Fig.2.13. This results

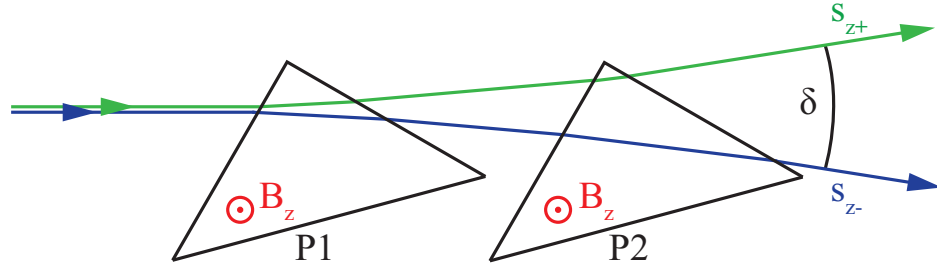


Figure 2.13: Scheme of the neutron beam passing the two birefringent magnetic prisms (P1,P2). The neutrons are refracted by the magnetic fields in z -direction (B_z) according to their spin direction (s_{z+} , s_{z-}). Behind the prisms the direction of the up-spin beam and down-spin beam differ by an angle δ .

in two polarized sub-beams. The angle difference between these two sub-beams is $\delta = 2.3 \cdot 10^{-5}$ rad for neutrons with a wave length of 1.92 Å. At the interferometer one of these sub beams can be selected by tuning the Bragg angle so that one sub-beam fulfills the Bragg-condition and is reflected, while the other passes through the interferometer with out interacting and therefore does not participate in the experiment any further.

A rocking curve is a plot of the angular distribution of the intensity, depending on the angle of the interferometer in respect to the incoming beam. The rotation axis is the z -axis. A typical expected rocking curve is depicted in Fig.2.14. By tuning the angle of the interferometer to the position corresponding to the center of the left peak, up-spin neutrons (s_{z+}) are selected and the down-spin neutrons (s_{z-}) pass trough the interferometer without interacting. When the interferometer is set to the position corresponding to the right peak it is the other way around.

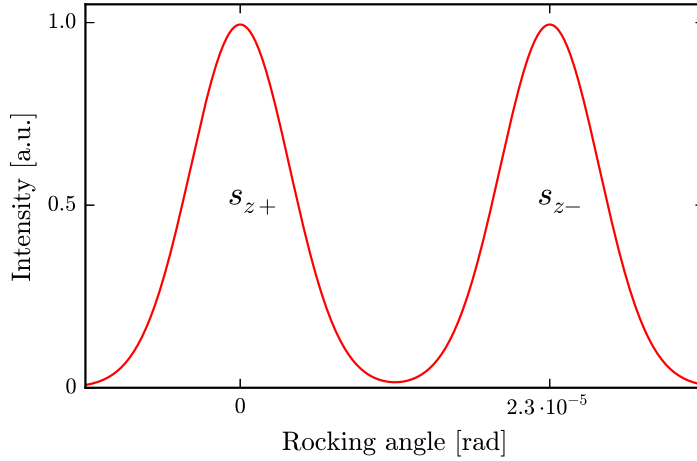


Figure 2.14: *Expected rocking curve of a neutron beam after passing through two birefringent magnetic prisms. The left peak consist of up-spin neutrons (s_{z+}) and the right peak consist of down-spin neutrons (s_{z-}).*

2.3.2 Neutron spin analysis

To measure specific spin states a spin analysis is needed. A super mirror in front of the detector allows only neutrons with one spin-component to pass trough and end up in the detector. In combination with a spin-rotation device, as described in section 2.3.5, any spin direction can by analyzed.

Typically the supermirror is constructed of many alternating thin layers of Nickel and Titanium as depicted in Fig2.15. Nickel is ferromagnetic with a magnetic permeability μ_{Ni} and has a coherent scattering length of $b_c(Ni) = 7.845$ b. Titanium is paramagnetic with a magnetic permeability μ_{Ti} and has a coherent scattering length of $b_c(Ti) = 1.485$. Note that depending on the alloy and production method the magnetic permeability can vary a lot. The total refraction index n of a material in a magnetic field is given by

$$n(B) = 1 - \lambda^2 \left(\frac{N b_c}{2\pi} \pm \frac{\mu_n m_n B}{h} \right), \quad (2.22)$$

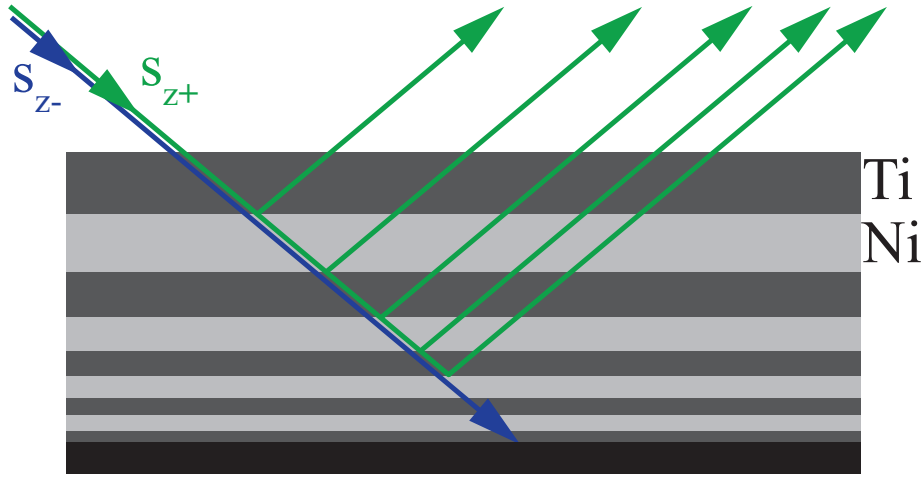


Figure 2.15: Scheme of a super mirror with alternating Ti layers (gray) and Ni layers (light gray) and an beam blocker on the backside (black). The up-spin neutrons are reflected. The down-spin neutrons are absorbed on the backside of the supermirror.

which is the sum of the nuclear and the magnetic refraction index. The \pm sign accounts for the two spin directions i.e. up-spin and down-spin. For a certain magnetic field B_{SM} the total refraction index n of Titanium and Nickel become equal in magnitude for the down-spin component of the neutrons only. Therefore the down-spin neutrons effectively "see" no layer structure, but the layer structure is still "visible" for the up-spin neutrons. The layers are designed to take advantage of Braggs law Eq.2.1 so that the critical reflection angle, until which total reflection occurs, is extended as far as possible for a neutron seeing the layer structure i.e. the up-spin component [Mezei, 1972]. While the down spin component passes through the layer structure and is absorbed by an neutron absorbing material at the back of the supermirror as shown in Fig.2.15. The supermirror is a device which filters out the down-spin component. Well constructed supermirrors achieve degrees of polarization of well above $P > 0.99$. Although the super mirror has

a high degree of polarization it can not be used in front of the interferometer because of the divergence of the neutron beam leaving the supermirror. This would lead to low count rates, since the acceptance angle of the interferometer is very small $< 10^{-6}$ rad, and low contrast as a direct consequence of the beam divergence.

2.3.3 Guide field

In polarimetric experiments usually a guide field $\vec{B}_{GF} = (0, 0, B_{GF})$ is applied in z-direction, over the whole experimental setup, to avoid depolarization. The guide fields are usually produced by Helmholtz like coil pairs. The ideal pair of Helmholtz coils consists of two circular coils with radius R , which are arranged coaxial with a distance of $d = R$ between them. Close to center line of the coil pair the field is nearly constant. In most neutron interferometric experiments a long guide field is needed, along the beam trajectory. To reduce the space required by the coils they are usually constructed in rectangular shape instead of a circular shape. In case of rectangular coils the distance d between the coils is half the width of the coils. The guide field strength is typically set between 10^{-3} T and $3 \cdot 10^{-3}$ T. The Larmor precession causes the neutrons polarization vector to rotate around the guide field in z-direction.

2.3.4 Larmor accelerators

The Larmor accelerator is a pair of Helmholtz like coils which apply a magnetic field parallel or anti-parallel to the guide field and accelerate or decelerate the Larmor precession, and therefore manipulate the azimuth angle ϕ of spin state. The action on the neutron spin can be expressed by the unitary transformation

$$\hat{U}_z(\alpha) = \begin{pmatrix} e^{-i\alpha/2} & 0 \\ 0 & e^{i\alpha/2} \end{pmatrix}, \quad (2.23)$$

with $\alpha = 2\mu B\tau/\hbar$. The coils are bent away from the neutron beam at the point of entrance and exit of the neutron beam. This reduces magnetic stray fields which could reduce efficiency of the device and also could lead to depolarization of the neutron beam. A depiction of a Larmor accelerator is given in Fig.2.16, as well as the first version built out of acrylic glass. Since the

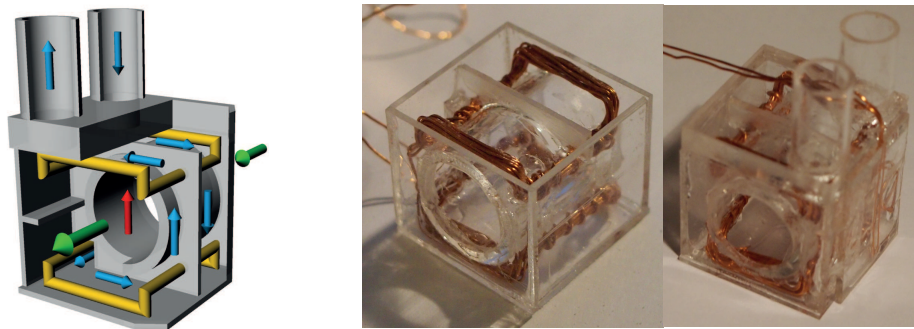


Figure 2.16: *Depiction of a Larmor accelerator. Left side: The copper wires coils are represented in yellow colored tubes. The green arrows represents the neutron beam passing through the Larmor accelerator, the red arrow represents the magnetic field, and the blue arrows represent the flow of the cooling water in the housing (gray). Right side: First version of Larmor accelerators built out of acrylic glass.*

neutron beam does not need pass through any material in this device, it can be used within the interferometer without any dephasing effect. When the Larmor accelerator is used within the interferometer it needs to be cooled to avoid thermal disturbance on the measurement. This is achieved by putting the coils into a water-tide box and pump water at a constant temperature through the box as depicted in Fig.2.16 by blue arrows. Recent versions of this device are built using 3D-printed boxes as described in section 2.3.7. This Larmor accelerators were deployed in the experiment measuring the Bell inequalities presented in chapter 3, as well as in the demonstration of the Quantum Cheshire cat [Denkmayr et al., 2014], a direct path measure-

ment experiment [Denkmayr et al., 2017], a measurement of general complex spin weak values [Sponar et al., 2015], and more experiments to come.

2.3.5 Direct current spin-rotators

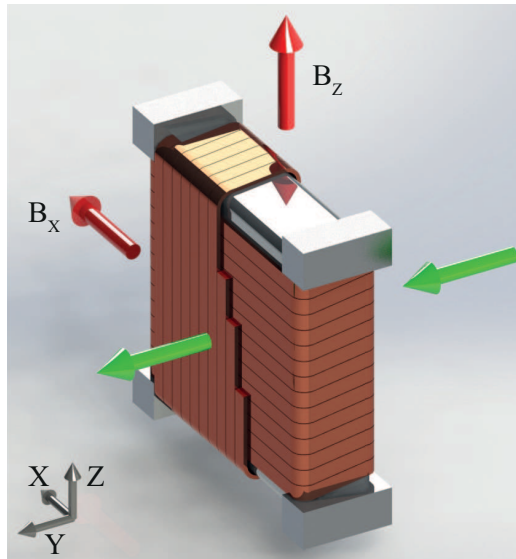


Figure 2.17: Schematic of a DC spin-rotator. Two coils made of copper wire are wound perpendicular to each other around an aluminium frame. The outer coil applying a field in z -direction B_z has a cutaway in the drawing to reveal the inner coil applying a field in x -direction B_x . The green arrows represent the neutron beam.

The direct current (DC) spin-rotator can manipulate the polar angle of the spin state, by applying a field in x -direction. Since a guide field is applied all over the setup, the DC spin-rotator needs a coil able to compensate the guide field $\vec{B}_{comp} = -\vec{B}_{GF}$, in addition to the coil generating the field in x -direction. The two coils are wound one onto the other as depicted in Fig.2.17, with the outer compensating coil applying a field of $\vec{B}_{comp} = (0, 0, B_z)$ and the actual spin-rotating inner coil applying a field of $\vec{B}_x = (B_x, 0, 0)$. The

action on the neutron spin can be expressed by the unitary transformation

$$\hat{U}_x(\alpha) = \begin{pmatrix} \cos\left(\frac{\alpha}{2}\right) & -i \sin\left(\frac{\alpha}{2}\right) \\ -i \sin\left(\frac{\alpha}{2}\right) & \cos\left(\frac{\alpha}{2}\right) \end{pmatrix}, \quad (2.24)$$

with $\alpha = 2\mu B\tau/\hbar$. The field transition from the guide field to the inner field needs to be non-adiabatic, or else the spin-polarization vector would just follow the changing field direction ending up in the same direction but with an added phase. This is why the DC spin-rotator is design so that the neutron beam passes through the coil material to achieve a instant change of the field direction.

2.3.6 Resonance-frequency spin-rotator

A resonance-frequency spin-rotator is another spin manipulation device, but in contrast to the spin-manipulators above it is operated using a time dependent field. Additional to the guide field $\vec{B}_{GF} = (0, 0, B_Z)$ a field $\vec{B}_{osc} = (0, B_{osc} \cos(\omega t), 0)$ oscillating parallel to the propagation direction of the neutron beam. The resulting magnetic field \vec{B}_{RF} , which is the sum $\vec{B}_{RF} = \vec{B}_{GF} + \vec{B}_{osc}$, can be rewritten as the sum of two fields of half the field strength of the oscillating field rotating around the z-axes, and the guide field, as given in

$$\vec{B}_{RF} = \begin{pmatrix} 0 \\ 0 \\ B_Z \end{pmatrix} + \begin{pmatrix} \frac{B_{osc}}{2} \sin(\omega t) \\ \frac{B_{osc}}{2} \cos(\omega t) \\ 0 \end{pmatrix} + \begin{pmatrix} -\frac{B_{osc}}{2} \sin(\omega t) \\ \frac{B_{osc}}{2} \cos(\omega t) \\ 0 \end{pmatrix}. \quad (2.25)$$

The oscillating field is set small compared to the guide field $|\vec{B}_{osc}| \ll |\vec{B}_{GF}|$, so that it can be neglected for all but one crucial case when the oscillation frequency is about the same as the Larmor frequency of the neutrons in the guide field $\omega \approx |\gamma|\vec{B}_{GF}$. In this case one rotating field of Eq.2.25 rotates in the same direction at the same frequency as the polarization vector \vec{S} of the

neutrons. The other rotating component can be neglected, which is known as the *rotating-wave approximation* (RWA) [Allen and Eberly, 1975]. Resulting in an approximated field

$$\vec{B}_{app} = \begin{pmatrix} 0 \\ 0 \\ B_Z \end{pmatrix} + \begin{pmatrix} B_{osc} \sin(\omega t) \\ B_{osc} \cos(\omega t) \\ 0 \end{pmatrix}. \quad (2.26)$$

The Shrödinger equation for a neutron interacting with the field \vec{B}_{app} is given by

$$\begin{aligned} i\hbar \frac{\partial}{\partial t} \psi(\vec{r}, t) = & -\frac{\hbar^2}{2m} \frac{\partial}{\partial r^2} \psi(\vec{r}, t) \\ & - (\mu\sigma_x B_{osc} \sin(\omega t) + \mu\sigma_y B_{osc} \cos(\omega t) + \mu\sigma_z B_{GF}) \psi(\vec{r}, t) \end{aligned} \quad (2.27)$$

Using the separation ansatz $\psi = \phi(\vec{r}) \cdot \zeta(t)$ the equation Eq.2.27 can be decomposed into two equations

$$\begin{aligned} -\frac{\hbar^2}{2m} \frac{1}{\phi(\vec{r})} \frac{\partial^2}{\partial r^2} \phi(\vec{r}) = C \\ i\hbar \frac{1}{\zeta(t)} \frac{\partial}{\partial t} \zeta(t) + (\mu\sigma_x B_{osc} \sin(\omega t) + \mu\sigma_y B_{osc} \cos(\omega t) + \mu\sigma_z B_{GF}) = C \end{aligned} \quad (2.28)$$

The solution of the first equation in Eq.2.28 is a plane wave

$$\phi(\vec{r}) = \frac{1}{\sqrt{2\pi}} e^{i\vec{k}\vec{r}}, \quad (2.29)$$

with $C = \hbar^2 k^2 / 2m$. The second equation in Eq.2.28 can be solved leading to the equation

$$\zeta(t) = e^{i\frac{\hbar k^2}{2m} t} \zeta(0) e^{-i\omega t \sigma_z / 2} \left[\cos(\alpha(t)/2) - i\vec{\sigma} \hat{\alpha} \sin(\alpha(t)/2) \right], \quad (2.30)$$

with $\alpha(t) = \gamma t \sqrt{(B_{GF} + \omega/\gamma)^2 + B_{osc}}$. A detailed calculation is presented in [Rabi, 1937, Ramsey, 1940, Bloch and Siegler, 1940, Suda, 2005]. Because of the approximation of the field B_{RF} by the rotating field B_{app} there is a small error in the calculation. The field oscillating in the opposite direction to the

Larmor precession cause a shift in the resonance frequency called the Bloch-Siegert shift [Bloch and Sieger, 1940], resulting in a resonance frequency of

$$\omega_{res} = \frac{2|\mu|B_{GF}}{\hbar} \left(1 + \frac{B_{osc}^2}{16B_{GF}^2} \right), \quad (2.31)$$

instead of $\omega = \frac{2|\mu|B_{GF}}{\hbar}$. The action of a resonance-frequency spin-rotator on the neutrons spin can be written using the unitary transformations in Eq.2.20, as

$$\begin{aligned} \hat{U}_{RF}(\omega, \alpha) &= \hat{U}_z^{-1}(\omega t) \hat{U}_x(\alpha) \hat{U}_z(\omega t) \\ &= \begin{pmatrix} \cos(\alpha/2) & -ie^{i\omega t} \sin(\alpha/2) \\ -ie^{-i\omega t} \sin(\alpha/2) & \cos(\alpha/2) \end{pmatrix}, \end{aligned} \quad (2.32)$$

with the oscillation frequency of the resonance-frequency spin-rotator ω , and the polar angle of rotation α . This is a rotation around x-axes which is transformed into a frame rotating around the z-axes at a frequency of ω_{RF} . The phase ϕ_{RF} of the resonance-frequency spin-rotator can be taken into account additionally, by an other unitary transformation $\hat{U}_z(\phi_{RF})$.

Note that a time dependent magnetic field $B(t)$ does not keep the total energy of the neutrons constant, since

$$\frac{d}{dt} \langle \hat{H}(t) \rangle \neq 0. \quad (2.33)$$

Therefore a small energy shift of $\Delta E = \hbar\omega_{res}$ occurs.

In the experiments a local guide field is put around the resonance-frequency spin-rotator so that the resonance frequency can be adjusted locally. A picture of a resonance-frequency spin-rotator is shown in Fig.2.18.

2.3.7 3D printing

3D-printing was invented in the 80s, but due to patent laws and complicated machinery 3D-printers were expensive and needed high amounts of maintenance work. With the start of the RepRap project, newly developed

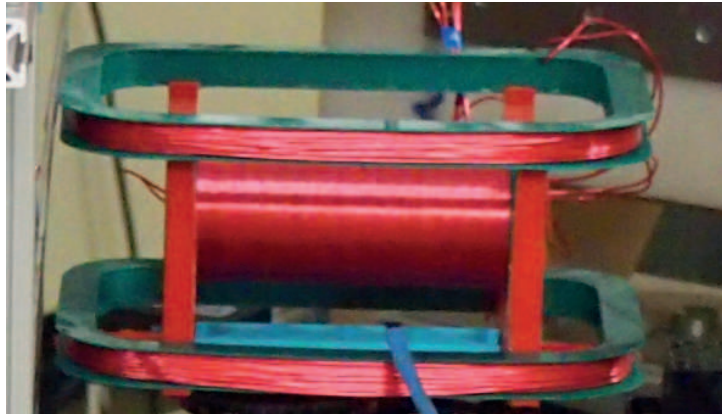


Figure 2.18: *Picture of a resonance-frequency spin-rotator and a pair of Helmholtz coils providing a local guide field for resonance adjustment.*

single board mini computers such as arduino and raspberry pi were utilized, leading to cheaper 3D printers. The RepRap project is an open source developer project, which lead to an accelerated evolution of both hard ware and software for extrusion deposit 3D-printers citePearce10, Jones11,Joshua12. In this process a plastic filament (a string of printing material) is forced by a gear drive into a heated nozzle, which melts the plastic and produces a thin layer of material as shown in Fig.2.19. The first successful print by the RepRap was performed in 2006, By printing one layer on top of the other the 3D-printer builds any desired structure as depicted in Fig.2.19. Designs can be more complicated and finer in structure than CNC-milling would allow for. In the year 2012 the price for 3D-printer kits for was still high, and the built quality of the printers and the print quality itself was poor. That is why I decided to built my own 3D-printer, which is depicted in Fig.2.19.

This printer was used for fabricating many parts of the experimental setup such as the Larmor accelerators, the RF spin-rotators, mounts for the supermirror, mounts for phase shifters, DC coils and many more. The printed parts are designed in a 3D-CAD program. The design files are converted into

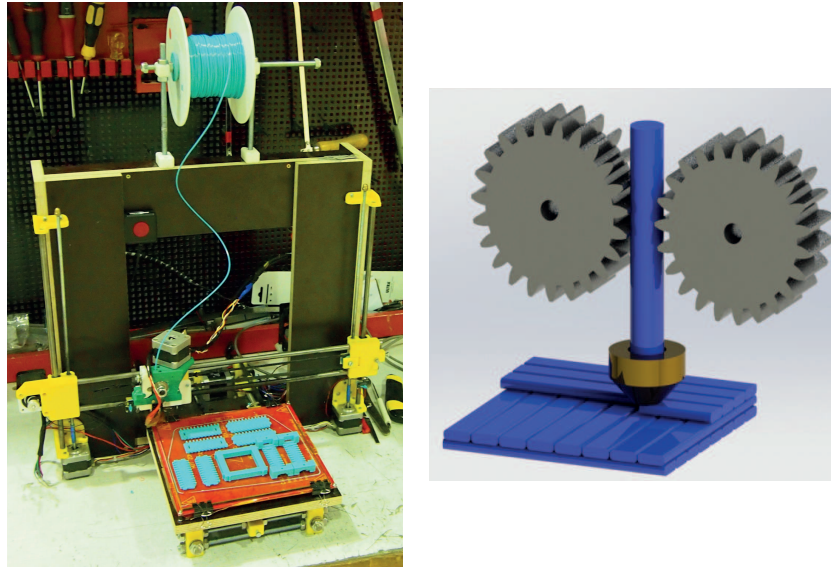


Figure 2.19: *Picture of the home built 3D-printer on the left. Illustration of the printing process on the right. The plastic string (filament) is forced through a heated brass nozzle by a set of gears. Beneath the nozzle the material is deposit in thin layers.*

a machine code called g-code, by a special software called Cura. The g-code controls the actual 3D printing process. A picture of a set of RF spin-rotators for use in the interferometer is depicted in Fig.2.20. The 3D printed parts have several advantages over machine milled metal parts. They are cheaper and faster to produce, therefore a large variety of designs can be manufactured and tested. The parts made of plastic have no electrical conductivity, have a low thermal conductivity, and are not magnetic so that remanence and short currents are not a problematic issue. 3D printed spin manipulators provide a better thermal stability than metal spin manipulators, since they are thermal insulators. Which is helpful when trying to improve the performance of the setup. The precision of the 3D-printed parts is better than 0.1 mm.

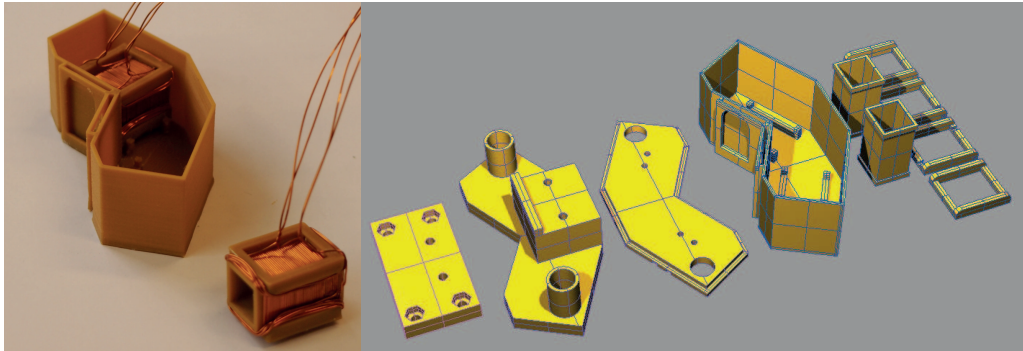


Figure 2.20: *The 3D-printed RF-spin rotator. Left: Picture of a 3D-printed box with two RF spin-rotators. Each spin-rotator has a small guide field to adjust the resonance frequency. Right: CAD-drawing of the RF-spin rotator.*

Chapter 3

Bell measurement

3.1 Introduction

At the beginning of the 20th century scientist believed that the world can be explained by one theory describing everything in a deterministic way and by knowing the exact state of a system at a given time, e.g. position and momentum of every particle of the system, the past and the future can be calculated precisely. Laplace's demon could even have known past and future of the whole universe [Laplace, 1814]. With the introduction of quantum mechanics the theoretical possibility of knowing everything, including past and future of a system, localism, and the exact predictability down to the smallest detail were ruled out on a very fundamental level. Because of the probabilistic nature of quantum mechanics, quantum contextuality, and the uncertainty principle introduced by Heisenberg [Heisenberg, 1927]. Only a probability on the outcome of an experiment can be given, but the outcome of the single event can not be predicted with certainty.

The uncertainty principle eliminates the possibility to know position and momentum of a particle at a certain time with arbitrary accuracy. Many physicists believed that quantum mechanics is incomplete and a new under-

lying theory would overcome the restrictions of quantum mechanics. Einstein was the best known critic of quantum mechanic, by saying '*He does not play dice*' he pointed out, that he did not believe in a probabilistic nature of physics as described by quantum mechanics [Born, 1971].

In their famous paper Einstein, Podolsky and Rosen [Einstein et al., 1935] argue that a complete physical theory must provide an arbitrarily accurate discription of the system at any given time. Since quantum mechanics does not, this theory is considert incomplete. To resolve this problem hidden variable theories have been presented which would resolve the shortcomings of quantum mechanics and give deterministic results [Bohm, 1952]. However, at the time no test could be made to decide, whether quantum mechanics or hidden variable theories provide a correct picture of nature. In 1964 John Bell presented his famous theorem [Bell, 1964], which pointed out a conflict between local hidden variable theories and quantum mechanics, providing a possibility to test which description actually coincides with nature.

Bell's inequality was introduced to give a limit for local hidden variable theories, which can be violated by quantum mechanics. Violaton of Bell's inequality in experiments, means that local hidden variable theories can not reproduce nature but quantum mechanics can. Such experiments have been accomplished using various physical systems, such as atomic cascade [Freedman and Clauser, 1972, Aspect et al., 1982], downconversion of laser [Kwiat et al., 1995, Weihs et al., 1998, Tittel et al., 1998], correlated photon pairs [Bertlmann and Zeilinger, 2002]. Furthermore neutron interferometric experiments confirmed a wider class of basic properties [Mermin, 1990], i.e. quantum contextuality [Hasegawa et al., 2003, Geppert et al., 2014].

3.2 The EPR argument

In quantum mechanics the state of a system is completely characterized by a wave function ψ , with variables such as position x and momentum p describing the state of the system. Any other set of variables can also be used to describe the system, given it provides the same predictions. For every measurable quantity A of the system there is a corresponding operator \hat{A} . When ψ is in an eigenstate of \hat{A} , which is the case if

$$\hat{A}\psi = a\psi, \quad (3.1)$$

then the observable A has with certainty the real value a . When ψ is in an eigenstate of A it is considered an element of reality, by the authors. For example, when the momentum operator

$$\hat{P} = \frac{\hbar}{i} \frac{\partial}{\partial x} \quad (3.2)$$

acts on the wave function

$$\psi = e^{\frac{ip_0x}{\hbar}}, \quad (3.3)$$

with a constant p_0 and an independent variable x , the result

$$\hat{P}\psi = p_0\psi \quad (3.4)$$

is obtained, i.e. the value p_0 is measured with certainty.

Heisenberg's uncertainty relation can be summarized as follows [Kennard, 1927]: for every measurement of the position X of a particle with a precision $\epsilon(X)$ a disturbance of the momentum P of $\eta(P)$ is caused, which satisfies the relation

$$\epsilon(X)\eta(P) \geq \frac{\hbar}{2}. \quad (3.5)$$

So by increasing the accuracy of the position measurement the disturbance on the momentum is increased and therefore the momentum can be known

less precisely. On the other hand a precise measurement of the momentum would lead to a less precise measurement of the position of the particle. The authors argue that a complete theory must represent both the position and the momentum of a particle at any time with arbitrary accuracy. Since quantum mechanics does not it is considered an incomplete theory by Einstein, Podolsky and Rosen.

The main argument, however, is the quantum mechanical description of two space like separated particles, as pointed out by Bohr [Bohr, 1935]. Two systems I and II interact for a given time $0 \leq t \leq T$ and the states of each system at a time $t < 0$ are well known. After the interaction $t > T$ the systems are separated and no further interaction can take place. Using the Schrödinger equation the wave function ψ of the combined system $I + II$ can be calculated. The state of either of the systems after the interaction can not be calculated. According to quantum mechanics further measurements are required. The wave function of the combined systems is given by

$$\Psi(x_1, x_2) = \int_{-\infty}^{\infty} e^{(2\pi i/h)(x_1 - x_2 + x_0)p} dp, \quad (3.6)$$

where x_0 is a constant, x_1 describes the first system, and x_2 the second. The observable is now the momentum \hat{P} of the first system, given by

$$\hat{P}\psi = \frac{\hbar}{2\pi i} \frac{\partial}{\partial x_1} \psi = p\psi, \quad (3.7)$$

then the eigenfunction to the eigenvalue p is given by

$$u_p(x_1) = e^{(2\pi i/h)x_1 p}. \quad (3.8)$$

The wave function of the combined system can now be written as

$$\Psi(x_1, x_2) = \int_{-\infty}^{\infty} \psi_p(x_2) u_p(x_1) dp \quad (3.9)$$

using

$$\psi_p(x_2) = e^{2\pi i/h(-x_2 + x_0)p}, \quad (3.10)$$

which is the eigenfunction of the operator

$$\hat{P} = \frac{h}{2\pi i} \frac{\partial}{\partial x_2} \quad (3.11)$$

corresponding to the momentum $-p$ of the second system. However, if we choose the observable to be the position of the position of the first particle with the eigenfunction

$$v_x(x_1) = \delta(x - x_1), \quad (3.12)$$

with the eigenvalue x , the wave function in Eq.3.6 can be written as

$$\Psi(x_1, x_2) = \int_{-\infty}^{\infty} \phi_x(x_2) v_x(x_1) dx, \quad (3.13)$$

where

$$\phi_x(x_2) = \int_{-\infty}^{\infty} e^{2\pi i/h(x-x_2+x-0)p} dp = \delta(x - x_2 + x - 0)h, \quad (3.14)$$

which is the eigenfunction of the operator $\hat{X} = x_1$, with the eigenvalue $x + x_0$ of the second particle. The operators \hat{X} and \hat{P} are non-commuting

$$[\hat{X}\hat{P}] = \hat{X}\hat{P} - \hat{P}\hat{X} = \frac{h}{2\pi i}. \quad (3.15)$$

So it is possible to assign two eigenfunction ϕ_x and ψ_p of non-commuting operators, corresponding to physical quantities. Depending on which measurement is performed first on the first system, the second system is left in a state with different wave function, even if no interaction between the two systems is possible since they are spatially separated. This is what Einstein referred to as the '*spooky action at a distance*'. In the first case \hat{P} is an element of reality in the second \hat{X} is an element of reality, in both cases the other is not, but both wave functions ϕ_x and ψ_p are part of the same reality. The authors conclude from the calculation above, that the description of quantum mechanics is not complete.

In the paper by Einstein, Podolsky and Rosen state that: '*... when the*

momentum of a particle is known, its coordinate has no physical reality... From this follows either (1) the quantum mechanical description of reality given by the wave function is not complete or (2) when the operators corresponding to two physical quantities do not commute the two quantities cannot have simultaneous reality. [Einstein et al., 1935]

If quantum mechanics is not complete there must be some kind of underlying mechanism, to give rise to the observed behavior of non-commuting quantum observables. One of the candidates to give such predictions is the so called hidden variable theory [Wheeler and Zurek, 1983].

There are two major assumptions in the EPR claim, which are realism and locality. Physical realism states that the value of an observable can be predicted before a measurement is made. The value of a physical quantity exists without the measurement and is therefore an element of reality. Physical localism states that the properties of a system must be independent from any interaction (measurement) on a spatially separated system. The properties of the system can be described locally. These assumptions conflict with the predictions of quantum mechanics.

3.3 Bell's inequality

In his paper '*On the einstein podolsky Rosen paradox*' [Bell, 1964] Bells starts at the example given in the paper by Bohm and Aharonov [Bohm and Aharonov, 1957], where an two spin one half particles in a singlet spin state propagate in opposite directions. Two Stern-Gerlach magnets perform measurements on each particle in direction α and β on particle a and B respectively. As in the example given above a measurement of the spin $\vec{\sigma}$ on the first particle in direction $\vec{\alpha}$ yielding $+1$ infers the result of -1 when a spin measurement in direction $\vec{\alpha}$ is performed on the second particle. This kind of predetermination is not valid in quantum mechanics, Bell states in

his paper *'this predetermination implies the possibility of a more complete specification of the state.'* He then introduces λ , which could be a parameter, a set of variables, or even a set of functions, and gives rise to a complete specification of the state. The parameter is also not limited to be discrete or continuous. A measurement of the spin of the first particle $\vec{\sigma}_A$ only depends on the direction \vec{a} and λ , the measurement of the spin of the second particle $\vec{\sigma}_B$ only depends on the direction \vec{b} and λ .

$$\begin{aligned} A(\vec{a}, \lambda) &= \pm 1 \\ B(\vec{b}, \lambda) &= \pm 1 \end{aligned} \tag{3.16}$$

The expectation value of the product of the components $\vec{\sigma}_1 \vec{a}$ and $\vec{\sigma}_2 \vec{b}$ is given by

$$P(\vec{a}, \vec{b}) = \int \rho(\lambda) A(\vec{a}, \lambda) B(\vec{b}, \lambda) d\lambda, \tag{3.17}$$

with the probability distribution $\rho(\lambda)$, that fulfills

$$\int \rho(\lambda) d\lambda = 1. \tag{3.18}$$

This should be equal to the quantum mechanical expectation value for the singlet state

$$\langle \vec{\sigma} \cdot \vec{a} \vec{\sigma} \cdot \vec{b} \rangle = -\vec{a} \cdot \vec{b}. \tag{3.19}$$

Because of the anti-correlation of $A(\vec{a}, \lambda) = -B(\vec{a}, \lambda)$, the equation Eq.3.17 can be written as

$$P(\vec{a}, \vec{b}) = - \int \rho(\lambda) A(\vec{a}, \lambda) A(\vec{b}, \lambda) d\lambda, \tag{3.20}$$

By introducing another unity vector \vec{c} the relation

$$\begin{aligned} P(\vec{a}, \vec{b}) - P(\vec{a}, \vec{c}) &= - \int \rho(\lambda) \left[A(\vec{a}, \lambda) A(\vec{b}, \lambda) - A(\vec{a}, \lambda) A(\vec{c}, \lambda) \right] d\lambda \\ &= \int \rho(\lambda) A(\vec{a}, \lambda) A(\vec{b}, \lambda) \left[A(\vec{b}, \lambda) A(\vec{c}, \lambda) - 1 \right] d\lambda, \end{aligned} \tag{3.21}$$

can be formulated with,

$$|P(\vec{a}, \vec{b}) - P(\vec{a}, \vec{c})| \leq \int \rho(\lambda) [1 - A(\vec{b}, \lambda)A(\vec{c}, \lambda)] d\lambda. \quad (3.22)$$

This can be written as

$$|P(\vec{a}, \vec{b}) - P(\vec{a}, \vec{c})| \leq 1 + P(\vec{b}, \vec{c}). \quad (3.23)$$

It is then shown that this relation prohibits, that $P(\vec{b}, \vec{c})$ can not reproduce the quantum mechanical value from equation Eq.3.19, by introducing the functions

$$\overline{P}(\vec{a}, \vec{b}), \quad \text{and} \quad \overline{-\vec{a}, \vec{b}}, \quad (3.24)$$

where the bar denotes averaging over vectors $\vec{a}' \cdot \vec{b}'$ within small angles of \vec{a} and \vec{b} . Under the assumption that there are boundaries ϵ and δ , with

$$|\overline{P}(\vec{a}, \vec{b}) + \overline{ab}| \leq \epsilon \quad \text{and} \quad |\overline{ab} - \overline{ab}| \leq \delta, \quad (3.25)$$

it is shown that the boundaries, i.e. the difference between classical description and a quantum mechanical description, can not be made arbitrary small

$$4(\epsilon + \delta) \geq |\vec{a} \cdot \vec{c} - \vec{a} \cdot \vec{b}| + \vec{b} \cdot \vec{c} - 1. \quad (3.26)$$

Therefore the quantum mechanical expectation value from equation Eq.3.19 can not be represented in the form of equation Eq.3.17.

3.3.1 Correlation measurements of photons

In 1951 Bohm published a paper [Bohm, 1951] reformulating the EPR argument, in which he replaced position and momentum measurements, by polarization measurements of two entangled spatially separated particles. This paper illustrated the essential features of the EPR argument and presents the paradox in the way it is found in many books today.

To describe correlation measurements, let us consider a source, which

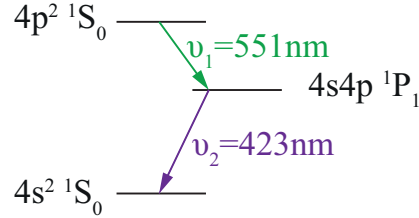


Figure 3.1: Scheme of the cascade decay in an calcium atom. Two photons are emitted at 551 nm and 423 nm wave length [Freedman and Clauser, 1972].

produces two entangled photons, for instance, by an atomic cascade decay of calcium [Freedman and Clauser, 1972, Aspect et al., 1982] as depicted in Fig.3.1, which are emitted in opposite direction. Since they are a decay product of an initial state with an angular momentum of $J = 0$ the photons must have opposite angular momentum one to the other. That is for example, one photon is emitted along the positive z-axis \vec{e}_z and the other along the negative z-axis $-\vec{e}_z$, as depicted in Fig.3.2. The resulting state is given by

$$|\Phi^{AB}\rangle = \frac{1}{\sqrt{2}}(|R^A, R^B\rangle + |L^A, L^B\rangle), \quad (3.27)$$

with $|R\rangle$ is right hand circular polarization and $|L\rangle$ is left hand circular polarization. This is a so called Bell state.

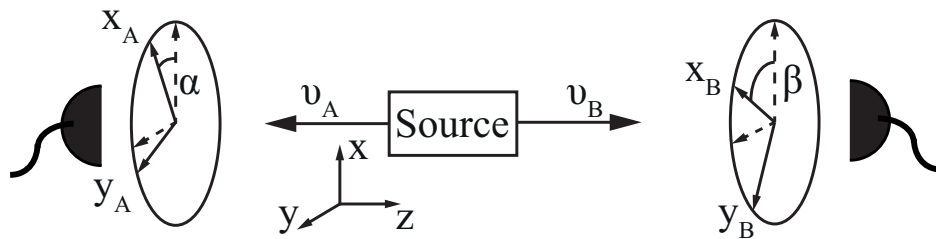


Figure 3.2: Source of entangled photons sending two photons (ν_A, ν_B) towards two polarization filters and detectors. On the left hand side the polarization filter can be rotated by an angle α on the right hand side by an angle β

This equation can be transformed into the laboratory frame in terms of measurement directions x_A, y_A and x_B, y_B resulting in

$$|R_A\rangle = \frac{1}{\sqrt{2}}(|x_A\rangle + i|y_A\rangle) \quad (3.28)$$

$$|L_A\rangle = \frac{1}{\sqrt{2}}(|x_A\rangle - i|y_A\rangle) \quad (3.29)$$

$$|R_B\rangle = \frac{1}{\sqrt{2}}(|x_B\rangle - |y_B\rangle) \quad (3.30)$$

$$|L_B\rangle = \frac{1}{\sqrt{2}}(|x_B\rangle + |y_B\rangle) \quad (3.31)$$

⇓

$$|\Phi^{AB}\rangle = \frac{1}{\sqrt{2}}(|x_A, x_B\rangle + |y_A, y_B\rangle), \quad (3.32)$$

with $|x_i\rangle$ and $|y_j\rangle$ representing linear polarized states. Two polarization filters and detectors are placed along the flight path of ν_A and ν_B . The polarization filters can be rotated around the z -axes as depicted in Fig.3.2, filter A by an angle of α and filter B by an angle of β . Using projection operators depending on the angle α of the polarization filter [Scully and Suhail Zubairy, 1997],

$$\hat{P}_x(\alpha) = |\alpha_x\rangle\langle\alpha_x| \quad (3.33)$$

$$\hat{P}_y(\alpha) = |\alpha_y\rangle\langle\alpha_y|, \quad (3.34)$$

with

$$|\alpha_x\rangle = \cos \alpha |x\rangle + \sin \alpha |y\rangle \quad (3.35)$$

$$|\alpha_y\rangle = -\sin \alpha |x\rangle + \cos \alpha |y\rangle \quad (3.36)$$

the probabilities for the outcome of a measurement at the left and the right

side can be calculated

$$P_+(\alpha) = \langle \Phi^{AB} | \hat{P}_x(\alpha) | \Phi^{AB} \rangle = \langle \Phi^{AB} | \alpha_x \rangle \langle \alpha_x | \Phi^{AB} \rangle = \frac{1}{2} \quad (3.37)$$

$$P_-(\alpha) = \langle \Phi^{AB} | \hat{P}_y(\alpha) | \Phi^{AB} \rangle = \langle \Phi^{AB} | \alpha_y \rangle \langle \alpha_y | \Phi^{AB} \rangle = \frac{1}{2} \quad (3.38)$$

$$P_+(\beta) = \langle \Phi^{AB} | \hat{P}_x(\beta) | \Phi^{AB} \rangle = \langle \Phi^{AB} | \beta_x \rangle \langle \beta_x | \Phi^{AB} \rangle = \frac{1}{2} \quad (3.39)$$

$$P_-(\beta) = \langle \Phi^{AB} | \hat{P}_y(\beta) | \Phi^{AB} \rangle = \langle \Phi^{AB} | \beta_y \rangle \langle \beta_y | \Phi^{AB} \rangle = \frac{1}{2}. \quad (3.40)$$

These single measurement give random results of equal probability. But when joint measurements are performed the probability for each set of joint measurement becomes a function of the difference in angles to which the polarization filters are set to.

$$P_{++}(\alpha, \beta) = \langle \Phi^{AB} | \hat{P}_x(\alpha) \hat{P}_x(\beta) | \Phi^{AB} \rangle = \frac{1}{2} \cos^2(\beta - \alpha) \quad (3.41)$$

$$P_{+-}(\alpha, \beta) = \langle \Phi^{AB} | \hat{P}_x(\alpha) \hat{P}_y(\beta) | \Phi^{AB} \rangle = \frac{1}{2} \sin^2(\beta - \alpha) \quad (3.42)$$

$$P_{-+}(\alpha, \beta) = \langle \Phi^{AB} | \hat{P}_y(\alpha) \hat{P}_x(\beta) | \Phi^{AB} \rangle = \frac{1}{2} \sin^2(\beta - \alpha) \quad (3.43)$$

$$P_{--}(\alpha, \beta) = \langle \Phi^{AB} | \hat{P}_y(\alpha) \hat{P}_y(\beta) | \Phi^{AB} \rangle = \frac{1}{2} \cos^2(\beta - \alpha). \quad (3.44)$$

The probability for finding both photons in the same polarization is given

$$P_{same}(\alpha, \beta) = P_{++}(\alpha, \beta) + P_{--}(\alpha, \beta) = \cos^2(\beta - \alpha). \quad (3.45)$$

The probability for finding both photons in the different polarization is given

$$P_{diff}(\alpha, \beta) = P_{+-}(\alpha, \beta) + P_{-+}(\alpha, \beta) = \sin^2(\beta - \alpha). \quad (3.46)$$

When the polarization filters are set parallel ($\alpha = \beta$) the probabilities for joint measurements become

$$\begin{aligned} P_{++}(\alpha, \alpha) &= P_{--}(\alpha, \alpha) = \frac{1}{2} \\ P_{+-}(\alpha, \alpha) &= P_{-+}(\alpha, \alpha) = 0. \end{aligned} \quad (3.47)$$

This means for parallel polarization filters, that when the photon ν_A is found

in the + channel, the photon ν_B must be found in the plus channel too. When photon ν_A is found in the - channel, then the photon ν_B is also found in the - channel. Thus full correlation occurs and by measuring on one side the outcome on the other side is instantly known with certainty. This can also be expressed using the correlation coefficient for polarization

$$E_{QM}(\alpha, \beta) = P_{++}(\alpha, \beta) + P_{--}(\alpha, \beta) - P_{+-}(\alpha, \beta) - P_{-+}(\alpha, \beta) \quad (3.48)$$

$$E_{QM}(\alpha, \alpha) = 1, \quad (3.49)$$

for parallel polarization filters the correlation becomes 1, or fully correlated. When the measurement is performed on one side first in direction α and the photon is found in the + channel, then a measurement of the photon in direction α on the other side has to be found in the + channel with certainty, even when the latter is measured much later. In quantum mechanics the outcome of the measurement is defined in the moment when the measurement is performed on one side, and the collapse of the wave function specifies the outcome of the measurement on the other side instantly. At the first glance this seems to violate the laws of relativity since the outcome on the second side is known instantly regardless of the distance between the photons. Never the less it is not, since no actual information transport has happened, just the collapse of the wave function.

3.3.2 Classical and quantum mechanical correlation measurements of correlated spin-1/2 particles

For simplicity of the argument λ is chosen to be a continuous parameter. Every particle is emitted with a random λ which holds the relation

$$\int \rho(\lambda) d\lambda = 1. \quad (3.50)$$

As an example the parameter λ is now chosen to be an angle in the xy-plane measured from the x-axis in the range 0 to 2π . A pair of particles emitted at the same time have the same parameter λ assigned randomly. The probability distribution becomes

$$\rho(\lambda) = \frac{1}{2\pi}, \quad (3.51)$$

which results in each possible direction of the polarization is equally likely. There must also be an unambiguous function $S_A^\lambda(\alpha)$ that assigns the outcome of a measurement to be either $+1$ or -1 , according to the parameters λ and α , to give deterministic outcomes. The same is true for the second particle with $S_B^\lambda(\beta)$. The functions giving an unambiguous outcome for every λ can be chosen to be

$$S_A^\lambda(\alpha) = \begin{cases} +1 & (\alpha - \lambda) \geq 0 \\ -1 & (\alpha - \lambda) < 0 \end{cases} \quad (3.52)$$

$$S_B^\lambda(\beta) = \begin{cases} +1 & (\beta - \lambda) \geq 0 \\ -1 & (\beta - \lambda) < 0 \end{cases} . \quad (3.53)$$

Using the definitions above, which give deterministic results just like classical mechanics, the probability for measuring $+1$ and -1 respectively can be calculated by

$$P_+^{CL}(\alpha) = \int \rho(\lambda) \frac{S_A^\lambda(\alpha) + 1}{2} d\lambda = \frac{1}{2} \quad (3.54)$$

$$P_-^{CL}(\alpha) = \int \rho(\lambda) \frac{1 - S_A^\lambda(\alpha)}{2} d\lambda = \frac{1}{2} \quad (3.55)$$

Accordingly the probabilities for the other side can be calculated by

$$P_+^{CL}(\beta) = \int \rho(\lambda) \frac{S_B^\lambda(\beta) + 1}{2} d\lambda = \frac{1}{2} \quad (3.56)$$

$$P_-^{CL}(\beta) = \int \rho(\lambda) \frac{1 - S_B^\lambda(\beta)}{2} d\lambda = \frac{1}{2}. \quad (3.57)$$

The probabilities for joint measurements can be calculated

$$P_{++}^{CL}(\alpha, \beta) = \int \rho(\lambda) \frac{S_A^\lambda(\alpha) + 1}{2} \frac{S_B^\lambda(\beta) + 1}{2} d\lambda \quad (3.58)$$

$$P_{+-}^{CL}(\alpha, \beta) = \int \rho(\lambda) \frac{S_A^\lambda(\alpha) + 1}{2} \frac{1 - S_B^\lambda(\beta)}{2} d\lambda \quad (3.59)$$

$$P_{-+}^{CL}(\alpha, \beta) = \int \rho(\lambda) \frac{1 - S_A^\lambda(\alpha)}{2} \frac{S_B^\lambda(\beta) + 1}{2} d\lambda \quad (3.60)$$

$$P_{--}^{CL}(\alpha, \beta) = \int \rho(\lambda) \frac{1 - S_A^\lambda(\alpha)}{2} \frac{1 - S_B^\lambda(\beta)}{2} d\lambda. \quad (3.61)$$

The correlation function for this system can be given by

$$E_{CL}(\alpha, \beta) = \int \rho(\lambda) S_A^\lambda(\alpha) S_B^\lambda(\beta) d\lambda = \frac{2|\beta - \alpha - \pi|}{\pi} - 1. \quad (3.62)$$

The fact that $E_{CL}(\alpha, \beta)$ is given by using the product of the functions $S_A^\lambda(\alpha)$ and $S_B^\lambda(\beta)$ reflects the locality inherent in this description, i.e. independence of a measurement on A from a measurement on B , and the other way around.

The equation Eq.3.49, which is calculated for spin-1 particles can be calculated in the same manner above for spin-1/2 particles yielding

$$E_{QM}(\alpha, \beta) = \cos^2\left(\frac{\beta - \alpha}{2}\right) - \sin^2\left(\frac{\beta - \alpha}{2}\right) = \cos(\beta - \alpha). \quad (3.63)$$

In Fig.3.3 a comparison between the correlation function for the classical hidden-variables model given by Eq.3.62 and the quantum mechanical correlation function given by Eq.3.63 is depicted. Note that the correlation functions differ by small amounts. This small derivations between the hidden-variable model and quantum mechanical description seemed to be resolvable, but are not as Bell has proven in his paper.

3.3.3 Simple example given for Bell's inequality

The discussion above shows, under special circumstances, a fundamental deviation between classic and quantum mechanical description of the EPR paradox. However, in his famous paper Bell presented a general approach to this

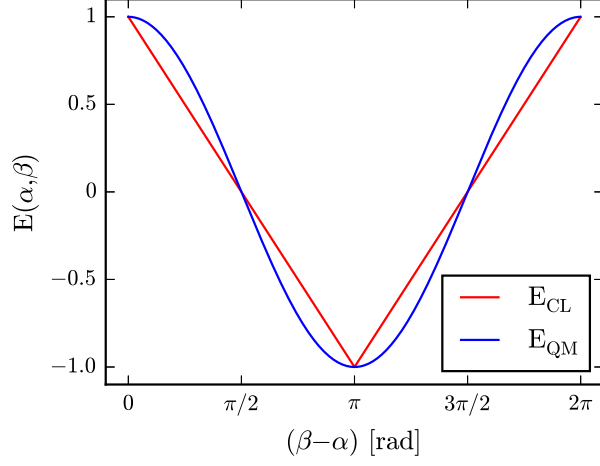


Figure 3.3: Polarization correlation coefficients for hidden-variable correlation $E_{CL}(\alpha, \beta)$ in red and quantum mechanical correlation $E_{QM}(\alpha, \beta)$ in blue, as a function of the relative angle $\beta - \alpha$ of the Stern-Gerlach magnets.

problem deriving Bell's inequality, which is an so called 'no-go theorem', disproving all local hidden variable theories at once. Starting with three pairs of measurements with all three having the same functional dependency of the parameter λ and an arbitrary measurement angle δ

$$S_A^\lambda(\delta) = S_B^\lambda(\delta) = S_C^\lambda(\delta) = S^\lambda(\delta). \quad (3.64)$$

The three measurements are performed at pairs of angles (α, β) , (α, γ) , and (β, γ) . Starting with this the equation Eq.3.21 results in

$$\begin{aligned} E_{CL}(\alpha, \beta) - E_{CL}(\alpha, \gamma) &= - \int \rho(\lambda) \left[S^\lambda(\alpha) S^\lambda(\beta) - S^\lambda(\alpha) S^\lambda(\gamma) \right] d\lambda \\ &= \int \rho(\lambda) S^\lambda(\alpha) S^\lambda(\beta) \left[S^\lambda(\beta) S^\lambda(\gamma) - 1 \right] d\lambda \end{aligned} \quad (3.65)$$

Which leads to

$$\begin{aligned} |E_{CL}(\alpha, \beta) - E_{CL}(\alpha, \gamma)| &\leq \int \rho(\lambda) \left[1 - S^\lambda(\beta) S^\lambda(\gamma) \right] d\lambda \\ |E_{CL}(\alpha, \beta) - E_{CL}(\alpha, \gamma)| &\leq 1 + E_{CL}(\beta, \gamma), \end{aligned} \quad (3.66)$$

this inequality corresponds to equation 3.23. This equation conflicts with quantum mechanical predictions, which can be shown by setting the measurement angles to $\alpha = \pi/3$, $\beta = 2\pi/3$, and $\gamma = \pi$ in an experiment using spin-1/2 particles. The correlation functions for the given angles give

$$E_{QM}(\alpha, \beta) = \frac{1}{2}, \quad E_{QM}(\alpha, \gamma) = -\frac{1}{2}, \quad \text{and} \quad E_{QM}(\beta, \gamma) = \frac{1}{2}, \quad (3.67)$$

and result in a violation of the inequality

$$1 \leq \frac{1}{2}. \quad (3.68)$$

This incompatibility of local hidden variables with the results of nature and quantum mechanics results in the foreclose all local hidden variable theories.

3.3.4 CHSH-formulation of Bells inequality

In 1969 Clauser, Horne, Shimony and Holt (CHSH-form) reformulated Bells inequalities [Clauser et al., 1969]. This new formulation is suitable for the first experimental test of quantum non-locality [Freedman and Clauser, 1972, Aspect et al., 1982]. The inequality given by CHSH is

$$|S| \leq 2, \quad (3.69)$$

where

$$S(a, a'b, b') = E(a, b) - E(a, b') + E(a', b) + E(a', b'). \quad (3.70)$$

This algebraic sum $S(a, a'b, b')$ is constructed from correlation functions $E(\alpha, \beta)$, with analysis angles $\alpha = a, a'$ for detector A and analysis angles $\beta = b, b'$ for detector B. The measurement results can be $\eta_A(\alpha) = +1, -1$ and $\eta_B(\beta) = +1, -1$. Calculating the $S(a, a'b, b')$ using classical expectation

values as given in Eq.3.62 leads to the result

$$|S_{CL}(a, a'b, b')| = |E_{CL}(a, b) - E_{CL}(a, b') + E_{CL}(a', b) + E_{CL}(a', b')| \leq 2. \quad (3.71)$$

While a quantum mechanical calculation using Eq.3.63 results in

$$S_{QM} = \cos(b - a) - \cos(b' - a) + \cos(b - a') + \cos(b' - a'). \quad (3.72)$$

When we use $\theta_{\alpha\beta} = \alpha - \beta$ and setting the angles $a = 0$, $a' = \pi/2$, $b = \pi/4$, and $b' = 3\pi/4$ which leads to equidistant $\theta_{\alpha\beta} = \theta = \pi/4$ the result of the algebraic sum becomes

$$S_{QM}(\theta) = 3 \cos(\theta) - \cos(3\theta) = 2\sqrt{2}, \quad (3.73)$$

which is the largest result for S_{QM} possible. A comparison between the classical limit $-2 \leq S_{CL} \leq 2$ and the quantum mechanical limit $2\sqrt{2} \leq S_{QM} \leq 2\sqrt{2}$ is given in Fig.3.4, where the green hatch part is the area of values not allowed classical but quantum mechanical. When the result of

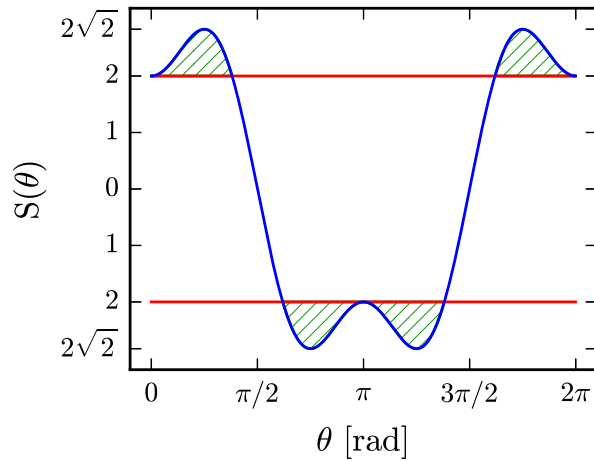


Figure 3.4: Comparison of the S value between local hidden variable theories (red) and quantum mechanics (blue). The green hatched areas are regions prohibited by local hidden variable theories but allowed in quantum mechanics.

an experimental measurement of S exceeds the classical limit of $|S| \leq 2$, as done in many experiments [Freedman and Clauser, 1972, Aspect et al., 1982, Bertlmann and Zeilinger, 2002, Kwiat et al., 1995, Weihs et al., 1998], this proves that no local hidden variable theory can reproduce nature and quantum mechanics ever. In the experiments the correlation functions are contracted as follows

$$E(\alpha, \beta) = \frac{N_{++}(\alpha, \beta) - N_{+-}(\alpha, \beta) - N_{-+}(\alpha, \beta) + N_{--}(\alpha, \beta)}{N_{++}(\alpha, \beta) + N_{+-}(\alpha, \beta) + N_{-+}(\alpha, \beta) + N_{--}(\alpha, \beta)}, \quad (3.74)$$

with the coincidence rates $N_{\pm\pm}(\alpha, \beta)$ at the detectors.

3.3.5 Bell's inequality for a single spin-1/2 particle and quantum contextuality

All discussions above are base on some source of entangled particles, propagating in opposite directions. However, there exists no neutron source available, which emits pairs of entangled neutrons with sufficient intensity.

In the paper '*Bell's inequality for a single spin-1/2 particle and quantum contextuality*' [Basu et al., 2001] a different approach is presented, that utilizes entanglement of two different degrees of freedom spaces of a single spin-1/2 particle, instead of entangled entangled pairs of particles. It is shown that noncontextual models [Mermin, 1993] can be tested, with out a localilty assumption given by Bell in his equality.

The spin-1/2 particle is described in terms of a tensor product $H = H_1 \otimes H_2$, where H_1 and H_2 correspond to the mutual disjoint Hilbert spaces for spin degree of freedom and path degree of freedom. They argue the experimental arrangement is given, as depicted in figure Fig.3.5.

A beam of neutrons polarized in $+z$ direction enters a Mach-Zehnder interferometer. The wave functions ψ_1 and ψ_2 are manipulated by a spin-flipper and a phase shifter, and the outgoing wave functions ψ_3 and ψ_4 leave

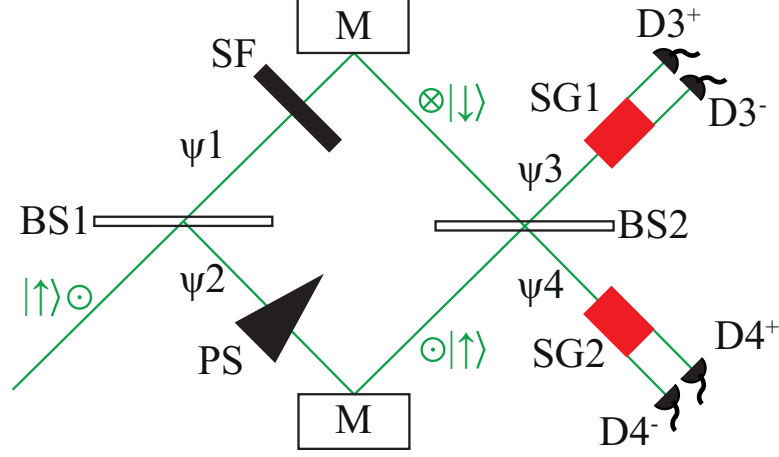


Figure 3.5: *Experimental arrangement using a Mach-Zehnder interferometer, with two beam splitters (BS1, BS2) and two mirrors (M). A neutron beam, polarized in $+z$ direction, passes through the first beam splitter (BS1). In one path the spin is flipped by spin-flipper (SF). A phase shifter (PS) induces the phase shift ϕ . The beams are recombined at the second beam splitter (BS2). Each outgoing beam passes a Stern-Gerlach device and four detectors ($D3^\pm$ and $D4^\pm$) are coupled to the four channels of the Stern-Gerlach devices.*

the interferometer.

The Bell-like state

$$\Psi = \frac{1}{\sqrt{2}}(|\downarrow\rangle \otimes |I\rangle + e^{i\phi} |\uparrow\rangle \otimes |II\rangle) \quad (3.75)$$

is generated, with $|I\rangle$ and $|II\rangle$ corresponding to the upper and the lower beam path, and $|\uparrow\rangle$ and $|\downarrow\rangle$ being the spin polarizations parallel or anti-parallel to the z -axes. For measuring the Bell-like inequality given by Basu, et al.

$$|\langle A_1 B_1 \rangle + \langle A_1 B_2 \rangle + \langle A_2 B_1 \rangle - \langle A_2 B_2 \rangle| \leq 2, \quad (3.76)$$

joint measurements of the path observable A_i and B_j need to be performed.

The path observable A_i and the spin observable B_j can be deduced from the count rates (N_3^\pm and N_4^\pm) of the four detectors (D3 $^\pm$ and D4 $^\pm$). For example:

$$\begin{aligned}\langle A_1 \rangle &= N_3^+ + N_3^- - (N_4^+ + N_4^-) \\ \langle B_1 \rangle &= (N_3^+ - N_3^-) + (N_4^+ + N_4^-) \\ \langle A_1 B_1 \rangle &= [N_3^+ + N_3^- - (N_4^+ + N_4^-)] [(N_3^+ - N_3^-) + (N_4^+ + N_4^-)]\end{aligned}\tag{3.77}$$

Similar relations can be derived for $\langle A_1 B_2 \rangle$, $\langle A_2 B_1 \rangle$, and $\langle A_2 B_2 \rangle$. By choosing suitable orientations of the Stern-Gerlach devices and phase shifter settings for the joint measurements $\langle A_i, B_j \rangle$, the result of a measurement of equation Eq.3.76 is larger than 2: a violation of Bell's inequality is achieved, and therefore noncontextual models are falsified. This measurement arrangement is suitable for showing a violation of this Bell-like inequality using perfect-crystal neutron interferometry.

3.4 Experiment: setup and improvement

To show the violation of Bell's inequality a setup is needed that provides high degree of polarization, high contrast of the interferometer, thermal stability, efficient spin-manipulation, and efficient spin-analysis. Since the classical limit for local hidden variable theories is $|S_{CL}| \leq 2$ and the quantum mechanical predicts is $|S_{QM}| = 2\sqrt{2}$, an overall efficiency ξ of the setup of less than $\xi \leq 0.707$ makes a violation of Bell's inequality not achievable. The efficiency of the setup ξ is a product of all imperfections of the setup, such as degree of polarization and contrast of the interferometer of less than 1, or the efficiency of the spin manipulation devices. To obtain a violation as high as possible every element of the setup must be optimized to highest possible performance. For example if the degree of polarization is $P = 0.9$ and the contrast is $C = 0.78$ it is impossible to show a violation of Bell's inequality, since the highest result achievable would be $2\sqrt{2} \cdot \xi = 1.98$, which would be

within the classic boundaries.

Previously used neutron interferometry setups [Hasegawa et al., 2003, Erdösi and Hasegawa, 2011] had drawbacks that degrade the quality of the measurement results. The devices used were designed for one measurement only, and could not be used for other experiments. In many other experiments contrast and degree of polarization were not as big as an issue, as they are for Bell measurements. The spin manipulators used were often constructed in a way so that the beam inside the interferometer passed through material such as Mu-metal sheets [Hasegawa et al., 2003], anodized aluminum [Allman et al., 1997] or magnetic foils [Abutaleb et al., 2012], causing dephasing and therefore loss in contrast.

To avoid depolarization the spin-turners need to provide a homogeneous magnetic field over the whole beam cross section and well defined magnetic field transitions between the guid field and the field of the spin manipulation device. Devices lacking this properties [Werner et al., 1975, Erdösi and Hasegawa, 2011] would cause too much depolarization.

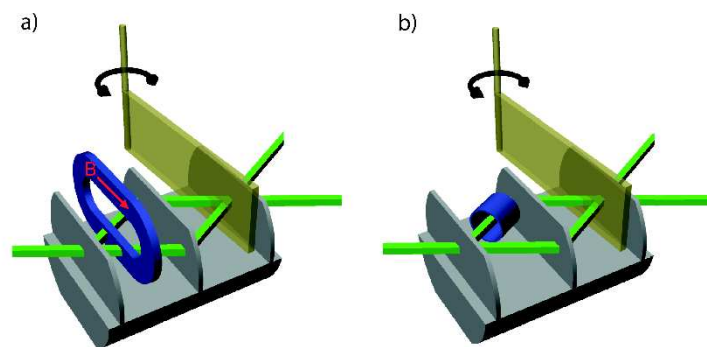


Figure 3.6: a) Setup with mu-metal inserted in the beam as spin-rotator. b) Setup using a mu-metal ring to shield the guide field causing depolarization due to field inhomogeneity.

For Bell-measurement using single-neutron interferometry two different

setups were realized [Hasegawa et al., 2003, Erdösi and Hasegawa, 2011] earlier, in which the spin manipulation was problematic causing loss in contrast and degree of polarization. These two setups are depicted in figure Fig.3.6. The interferometer with inserted soft magnetic Mu-metal foil as a spin-rotator is depicted on the left side [Hasegawa et al., 2003]. The rotation is achieved by a magnetic field induced into the Mu-metal by a coil around the sheet outside of the IFM. The Mu-metal sheet considerably reduced the contrast of the IFM by dephasing. To overcome this problem another setup was designed, which does not need any material in the neutron beam in the interferometer [Erdösi and Hasegawa, 2011], shown in figure Fig.3.6 on the right side. In one path of the interferometer the beam passes a tube of Mu-metal which reduces the magnetic guide field strength and thereby induces a relative spin-rotation by different amount of Larmor precession in the two IFM paths. Since the guide field leaks into the cylinder at its open ends, the field homogeneity is compromised which causes depolarization of the neutron beam. This setup also requires a spin turner in front of the interferometer which in addition reduces the degree of polarization as described below.

A new setup is designed to improve performance and tuneability. This setup is not only used to measure Bell's inequality, but also for the measurement of the quantum Cheshire Cat, spin and path weak values, path state reconstruction, the quantum pigeonhole effect [Denkmayr et al., 2014, Sponar et al., 2015, Denkmayr et al., 2017, Waegell et al., 2017], and is still in use for other experiments.

3.4.1 Measurement concept

Essential for every Bell measurement is the generation of a fully entangled state, or Bell-like state. In the Bell argument one particle moves towards the detector A while the other moves in opposite direction to detector B, with anti-parallel spin polarizations. In this experiment a single loop interferom-

eter providing two paths the neutrons can go through is used, with spin s_{x+} in path I and spin s_{x-} in path II , as given in

$$\Psi_{Bell} = \frac{1}{\sqrt{2}} \left(|I\rangle |s_{x+}\rangle + |II\rangle |s_{x-}\rangle \right). \quad (3.78)$$

This is a fully entangled or Bell-like state. Instead of using two detectors and two polarization filters as proposed by Bell, one detector measures a correlation of the spin and the path observable. The algebraic sum S given in equation Eq.3.70 becomes a function of a parameter for spin measurement direction α , which is an angle in the yz -plane of the Bloch sphere, and the phase shift χ between the paths,

$$S(\alpha, \alpha', \chi, \chi') = E(\alpha, \chi) + E(\alpha, \chi') - E(\alpha', \chi) + E(\alpha', \chi'), \quad (3.79)$$

with the correlation function

$$E(\alpha, \chi) = \frac{N_{++}(\alpha_+, \chi_+) - N_{+-}(\alpha_+, \chi_-) - N_{-+}(\alpha_-, \chi_+) + N_{--}(\alpha_-, \chi_-)}{N_{++}(\alpha_+, \chi_+) + N_{+-}(\alpha_+, \chi_-) + N_{-+}(\alpha_-, \chi_+) + N_{--}(\alpha_-, \chi_-)}. \quad (3.80)$$

The coincident rates are given by $N_{\pm,\pm}(\alpha_{\pm}, \chi_{\pm}) = [1 + \cos(\alpha_{\pm} - \chi_{\pm})]/2$. The largest violation of Bell's inequality is given for spin analysis directions $\alpha_+ = 0$, $\alpha'_+ = \pi/2$, $\alpha_- = \pi$ and $\alpha'_- = 3\pi/2$, and path selections $\chi_+ = \pi/4$, $\chi'_+ = 3\pi/4$, $\chi_- = 5\pi/4$ and $\chi'_- = 7\pi/4$. This settings result in a theoretical violation of $S = 2\sqrt{2} \not\leq 2$. Figure Fig.3.7 shows the spin and path settings depicted on Bloch-spheres.

In Fig.3.8 the experimental setup is shown. A magnetic guide field $\vec{B}_{GF} = (0, 0, B_{GF})$ is applied over the whole setup to prevent depolarization. The Bell state (Eq. 3.78) is prepared by polarizing the neutrons in the $+z$ direction using birefringent prisms as described in section 2.3.1, which is then rotated into $+y$ direction, by DC spin-rotator as described in section 2.3.5. The beam polarized in $+y$ direction enters the interferometer and is rotated around the z -axes by $-\pi/2$ in path I and by $\pi/2$ in path II by two Larmor accelerators, one in each path, as described in section 2.3.4. At this stage the Bell state

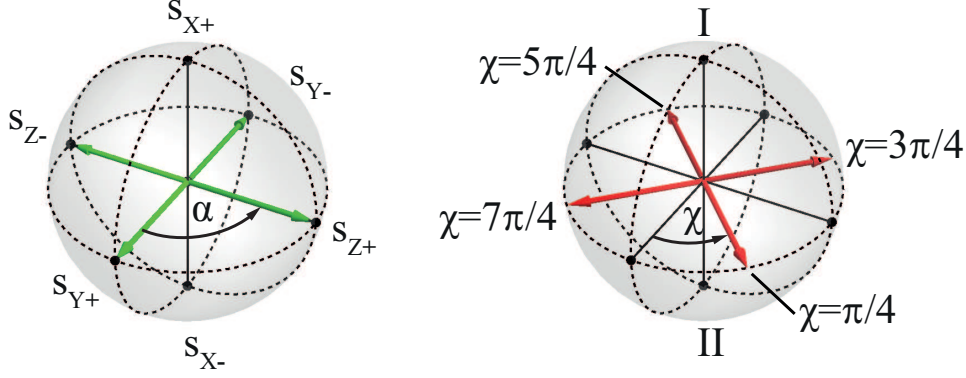


Figure 3.7: *Left: Spin measurement direction for the largest violation of Bell's inequality. Right: Path selection for largest possible violation. The superposition of path I and path II results in a path state in the equatorial plane which can be rotated by phase shifter by an angle of χ .*

is prepared.

In order to set the path states χ_{\pm} and $\chi'_p m$, a phase shifter in the interferometer is tuned accordingly. The path part of the wave function is given by

$$\psi(\chi) = \frac{1}{\sqrt{2}}(|I\rangle + e^{i\chi}|II\rangle). \quad (3.81)$$

Only the neutron beam measured by the O-detector is used for the measurement, since it is the only beam able to show full contrast, as described in 2.2. That is why spin analysis is only applied on the O-beam. The spin selection is accomplished by a second DC spin-rotator and a supermirror. By tuning the field strength of the DC spin-rotator the polar angle θ measured from the z-axis is adjusted. While the azimuth angle ϕ is tuned by moving the DC spin-rotator along the flight path of the neutrons. Due to Larmor precision caused by the guide field, the change in length l of the flight path up to the

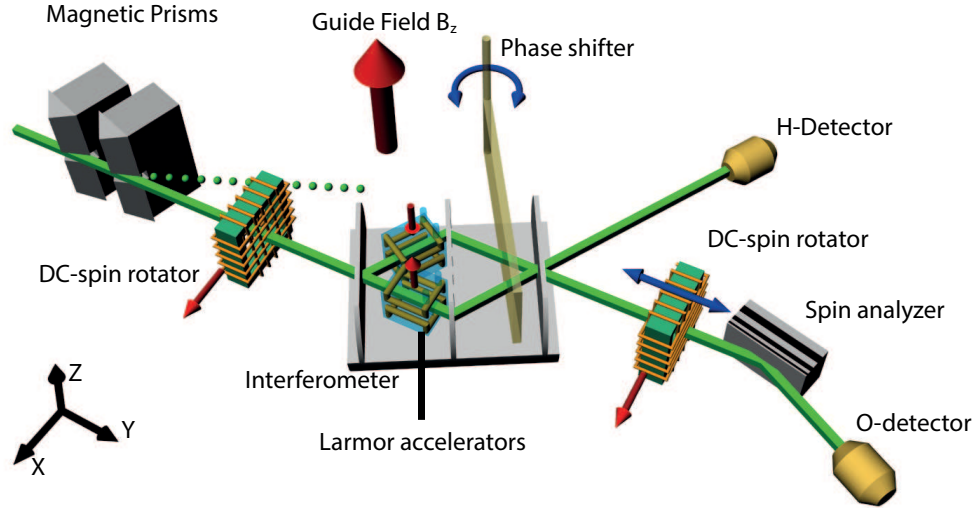


Figure 3.8: *Setup for measuring Bell's inequality. Magnetic prisms polarize the neutrons and a DC spin-rotator rotates the spin in $+y$ direction. In the interferometer a Bell state is generated by two Larmor accelerators. The path state is selected by a phase shifter and the third plate of the interferometer. Behind the interferometer the spin state is selected by an other DC-spinrotator and the supermirror spin analyzer. The O-detector counts the selected neutrons. A guide field is applied over the whole setup to prevent depolarization.*

DC spin-rotator results in different azimuth angles ϕ , as given in

$$\phi(l) = \frac{2\mu B_{GF}}{\hbar v_n} l. \quad (3.82)$$

Since the supermirror lets the $|s_{z+}\rangle$ spin component pass and the other components are filtered out, the second DC spin-rotator must be tuned in a way that the spin component required for the measurement is rotated into $z+$ direction. The O-detector only measures the neutrons passing through the supermirror, which have a the spin component parallel to the $+z$ direction.

3.4.2 Setup design

In this experiment symmetrical triple-Laue interferometer is used, which has an overall length of 123 mm, a plate thickness of 3 mm, and a plate separation of 53 mm. This interferometer named 'Kaiser interferometer', is chosen because of the high contrast of > 0.9 [Geppert et al., 2014] and the large space between the plates to accept sufficiently large spin manipulation devices. In order to achieve a large violation all components of the setup must be optimized to reduce perturbations on the system. The two most important factors are high temperature-stability and avoiding depolarization.

The neutron interferometer is very sensitive to temperature fluctuations, which reduces contrast and induces phase fluctuation.

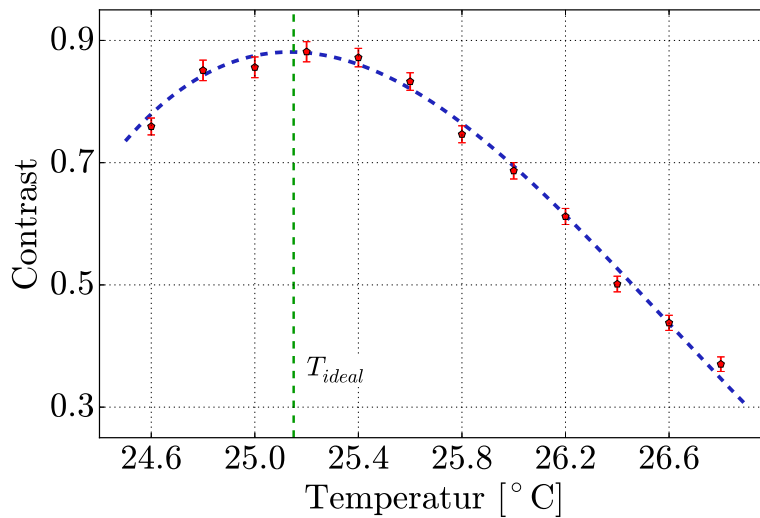


Figure 3.9: *Influence of the surrounding temperature on the contrast of the interferometer. At 25.15°C a contrast $C > 0.88$ is achieved, which is marked with a dashed green line. At a temperature 1°C higher than the ideal temperature a contrast of only $C < 0.60$ can be achieved.*

The spin manipulators inside the interferometer i.e. the Larmor accelerators, need to be water cooled since the coils produce heat that would disturb

the interferometer. To evaluate the influence of temperature fluctuations on the interferometer the water temperature inside the Larmor accelerators is changed and the contrast is measured at different temperatures. In figure Fig.3.9 the contrast as function of the cooling water temperature of spin manipulation device is given. When the temperature is set to the temperature of the setup environment the contrast becomes largest, because no temperature gradients are present and the interferometer is kept at a stable temperature. This is fulfilled at 25.15°C and the contrast at this cooling water temperature is $C > 0.88$. When the temperature of the spin manipulation device is changed by just 1°C the contrast drops to $C < 0.6$. A temperature of 0.7°C over the ideal temperature leads to a drop in contrast to below $C < 0.71$ and therefore no violation of Bell's inequality would be notable.

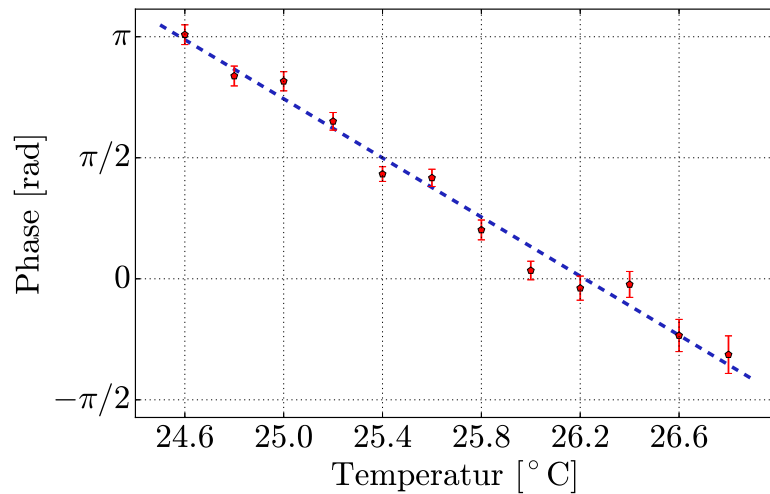


Figure 3.10: *The phase shift induced by temperature change of the Larmor accelerators inside the interferometer.*

Even more delicate is the phase shift induced by temperature gradients and fluctuations as shown in figure Fig.3.10. A change in temperature of 1°C results in a phase shift of 1.92 rad. This results in $S < 2$ for a temperature change of just 0.22°C . In practices even a small droplet of water evaporating

on the surface of the Larmor accelerator makes no measurements possible. This results are specific for each interferometer and can vary a bit, but are of similar magnitude for every interferometer.

The second big issue are in-homogeneous magnetic fields. If the field applied by a spin manipulation device is not homogeneous over the whole cross section, different parts of the beam are rotated by different amounts, which results in depolarization. Every time a non-adiabatic field change occurs the beam can lose degree of polarization easily. This effects can be minimized by using adiabatic field transitions whenever possible, or aligning fields producing a non adiabatic field transition as good as possible.

New guide field

The old guide field used in previous experiments had several shortcomings, such as the small size, the in-homogeneous field, and insufficient thermal properties. The old guide field didn't allow for the newly built interferometer presented in chapter 4 since it was too narrow. The small width of the guide field also results in an in-homogeneous field over the width and height of the guide field, since the field gradients increase in close proximity of the coil windings. The old guide field had a water cooling system, but the thermal coupling of the wires to the cooling water was insufficient, therefore too much heat was transferred from the coils to the interferometer.

The guide field is the largest magnetic field component of the the new setup. The new magnetic guide field should be as homogeneous as possible over the whole width and length of the setup, while providing as much space as possible between the coils for other components, such as the interferometer itself, the spin manipulation devices and also an aperture for beam shaping. The coils must be insulated and water cooled to avoid thermal perturbation on the interferometer. The coils should be able to provide guide fields up to 30 G, which is needed for some experiments using resonance frequency

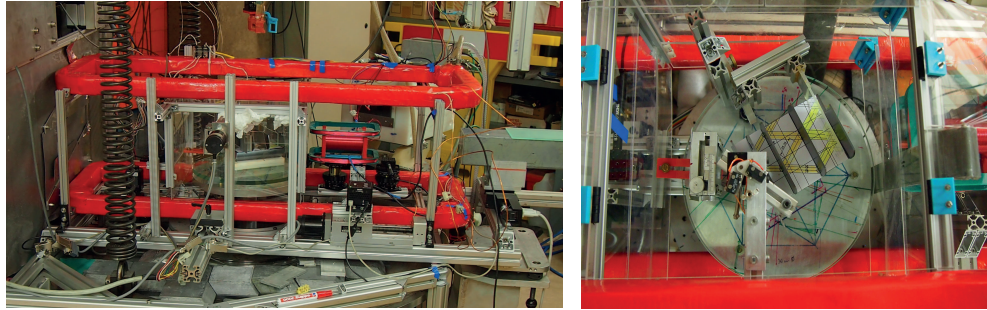


Figure 3.11: *Pictures of the new guide field. Left: Side view of the Guide field (red) in the setup. The length is limited by the radiation shielding to the left and the supermirror to the right. Right: Detail of the setup from above. The guide field is built wide enough to fit the table on which the interferometer stands and a box of acrylic glass around the interferometer.*

spin-rotators. A Helmholtz-like design is made with a pair of coils which are separated in z-direction by half their width, which provides a homogeneous field along the longitudinal center line except for the very ends. A CAD-drawing of the of one coil frame is shown in figure Fig.3.12.

The windings (orange) are embedded in an aluminium frame (black), which provides structural support and tubing for the cooling water. The tubing for cooling water is rectangular with a width of 36 mm and 16 mm height. The frame provides a rectangular gap of 38 mm width and 18 mm height, which is enough space for 120 windings of the wire with a diameter of 2 mm. This results in a resistance of 1.8Ω for each coil. The gaps between the wires are filled with heat conducting resin to provide good heat transport from the wires to the cooling water. The coils are wrapped in insulating foam, which reduces the heat transport towards the interferometer. The finished coils weigh about 25 kg each.

The length of the guide filed is limited to 1.1 m by the space between the shielding around the neutron guide in front, and in the back by the position

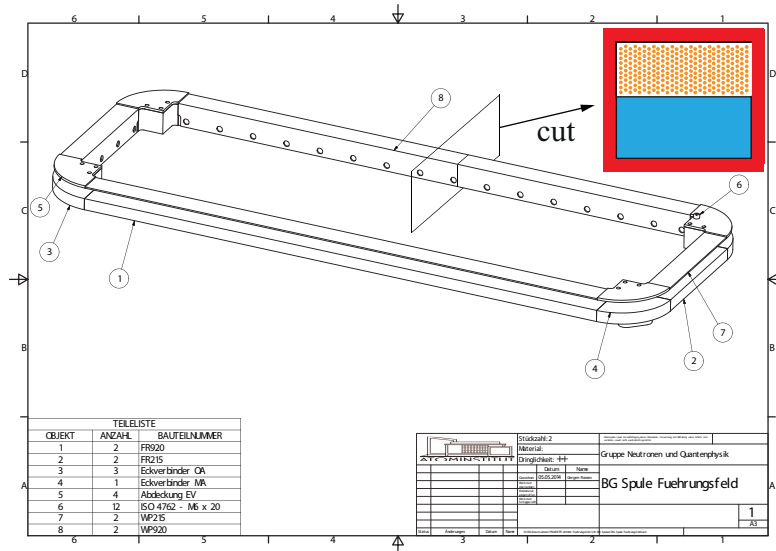


Figure 3.12: CAD-drawing of one of the two coil frames for the guide field. A cut is shown in the upper right corner, representing the finished coil with winding and insulation. Aluminium profiles (black) provide tubing for cooling water (blue) and space for copper wire (orange). The gaps between the wires is filled with heat-conducting resin. The coil is wrapped with insulating foam (red).

of the supermirror in front of the O-detector, as can be seen in the photo Fig.3.11. The interferometer is placed on a rotating table as can be seen on the left picture in Fig.3.11. The table is enclosed in a acrylic box, which avoids convectional ventilation at the interferometer. This box needs to fit inside the guide field coils. Since the box is 0.3m wide, the coils have to be at least 0.31m wide on the inside. The vertical distance between the lower and the upper coil is 0.175m, this distance accounts for the volume of the windings.

The coils are connected in a parallel circuit. The new guide field provides a field strength of 3.6 G/A, which results in a current of 8.3 A for the desired maximal guide field of $B_{GF} = 30$ G. Since the coils are in a parallel circuit

the resulting thermal output is 62 W.

Monochromator

The monochromator selects neutrons with the wave length λ used in the experiment and also defines the wave length distribution, therefore the neutron velocity distribution. Depending on the design of the monochromator the full width at half maximum (FWHM) σ of the wave length distribution can vary. It is basically a trade of between higher count rate for larger σ or longer coherence length for smaller σ . The FWHM can be quantify by measuring a rocking curve, where the intensity is measured while the interferometer is rotated around the vertical axes. The monochromatization also influences the efficiency of the spin manipulation devices. The angle of rotation of the neutron spin is directly proportional to the time the neutrons are exposed to the field, as given in $\alpha(\tau) = 2\mu B\tau/\hbar$. Since slower neutrons take more time τ to pass a spin manipulator, they are rotate a little more than faster neutrons, which effectively reduces the degree of polarization.

Also the initial degree of polarization is influenced by the monochromator, because of the small separation between up-spin and down-spin component of the neutron beam, achieved by the magnetic prisms. In figure Fig.3.13 a rocking curve of a beam passing through the two birefringent magnetic prisms is shown. Two separated peaks are visible, one coming from the up-spin component, the other the down spin component. When the peaks get wider the peaks can overlap so much that down-spin neutrons fulfill the Bragg condition at the up-spin peak, therefore they are reflected by the first plate of the interferometer and reduce the degree of polarization.

In previous setups a single-fold reflection from a silicon perfect crystal monochromator was used, which provided a beam with mean wave length of 1.92 \AA and a FWHM of $\sigma = 6.11 \cdot 10^{-6} \text{ rad}$. In the new setup a three-fold reflection from a new silicon perfect crystal monochromator is used which

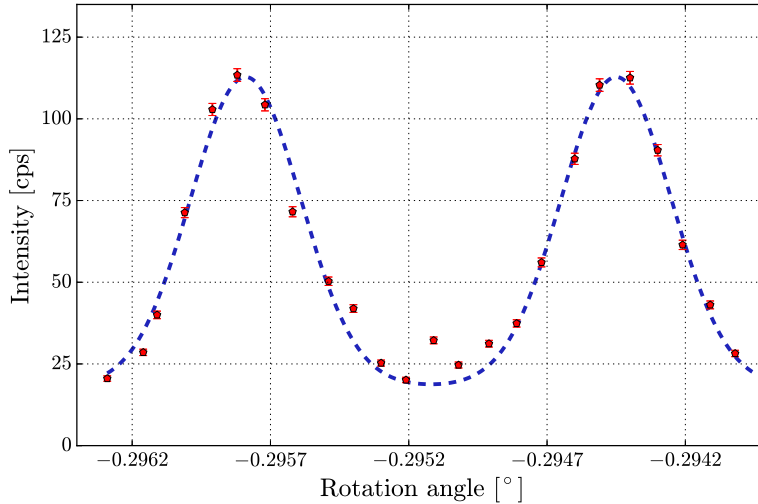


Figure 3.13: *Rocking curve with the two birefringent prisms in place. Two peaks are visible one consisting of up-spin neutrons the other of down-spin neutrons.*

provides the same wave length but a FWHM of $4.26 \cdot 10^{-6}$. The respective rocking curves are shown in Fig.3.14. The smaller FWHM is achieved at the expense of about 10% decreased count rate.

New DC spin-rotators

The DC spin-rotators consist of two coils one providing a field compensating the guide field and a second for the field performing the desired spin-rotation, as described in section 2.3.5. The two field should be perpendicular to each other and the field transition from the guide field to the DC spin-rotator field should be non-adiabatic. If the field transition would be adiabatic, the spin polarization would follow the magnetic field change and would not rotate as desired. A non-adiabatic field transition is best achieved when the neutron beam is passing through the windings. Since the neutrons propagate through material, small angle scattering occurs. This small angle scattering is

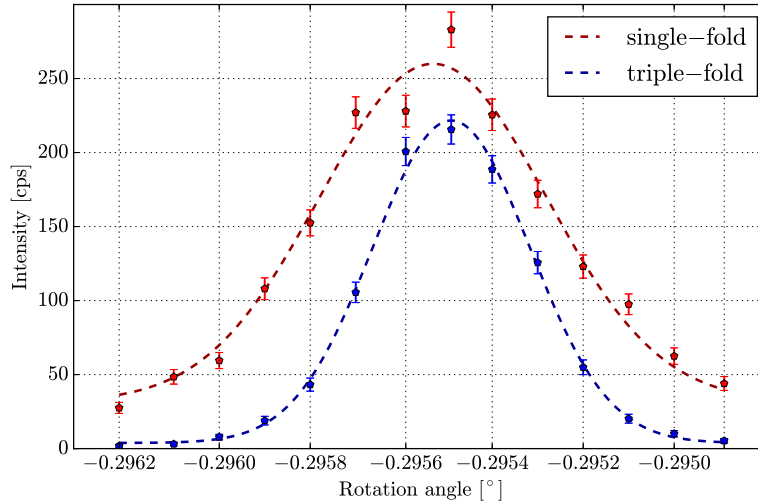


Figure 3.14: *Rocking curve using a single-fold silicon perfect crystal monochromator (red) and using a triple-fold silicon perfect crystal monochromator (blue).*

problematic for the first DC spin-rotator between the prisms and the interferometer: due to small angle scattering the FWHM of the rocking curves can increase, therefore more down-spin neutrons are scattered into the up-spin peak and the degree of polarization is reduced.

In the previous setups copper wires were used for the coils, which produced much scattering. The small angle scattering can be reduced in two ways: by changing the winding material from a round wire to a flat band, and by choosing a material with lower scattering cross section. Several prototypes for the new DC spin-rotators are fabricated and tested. The first is made out of high purity aluminium wire with a diameter of 0.5 mm. Aluminium has a ten times smaller scattering cross section than copper. Three different DC spin-rotators are made, using copper and aluminium ribbons instead of wires, which, due to their rectangular cross section, produce less small angle scattering than wires made of the same materials. The copper

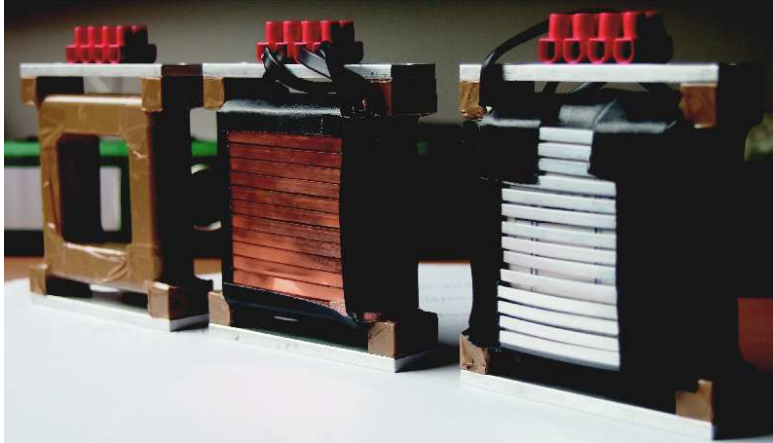


Figure 3.15: *An empty frame for a DC spin-rotator, a DC spin-rotator made of copper ribbon, and one made of aluminium ribbon.*

ribbons used are made of high purity copper, are 0.1 mm thick, and 3 mm and 4 mm wide respectively. The high purity aluminium ribbon is 4 mm wide and 1 mm thick. The aluminium wire is thicker because it is much less ductile than copper and brittle when thin. Figure Fig.3.15 shows a frame of a DC spin-rotator without wires and two completed types of DC spin-rotators, one using copper ribbon the other aluminium ribbon. All DC spin-rotators use the same frame design made of aluminium, which is 70 mm wide, 70 mm high, and 20 mm deep.

All new DC spin-rotators are tested by measuring rocking curves with the spin-rotators put between the monochromator and the interferometer. As comparison a rocking curve is measured with nothing between monochromator and interferometer. The results are shown in the graph Fig.3.16. In table Tab.3.1 the results of the measurements are summarized. These measurements show that there is more influence on the FWHM, whether wires or ribbons are used, than the material properties for copper and aluminium. The aluminium ribbon coils have the same properties as the copper ribbons coils, within the errors. The FWHM of the ribbon coils is 30 % smaller than

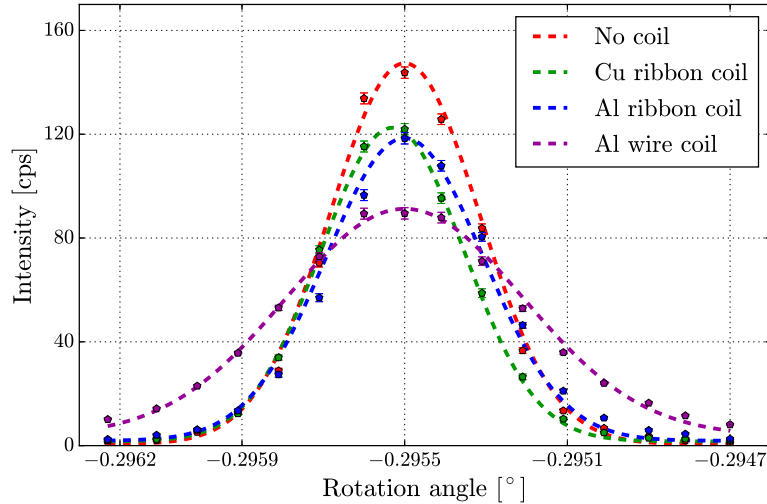


Figure 3.16: *Rocking curves without a DC spin-rotator placed in the beam line and with different DC spin-rotator designs in the beam line.*

the FWHM of the wire coil. It is important to notice that not only the degree of polarization is reduced by small angular scattering but also the count rate. The wire coil has 30% less peak height and therefore transmission than the ribbon coils. For the experiment the 3 mm wide copper wire is chosen, because it is easier to handle than aluminium ribbon and more windings can be applied than with the 4 mm copper ribbon.

To test the degree of polarization of the setup and the efficiency of the DC spin-rotators the two flipper method [Fredrikze and van de Kruijs, 2001] is used. The interferometer is tuned so that the up-spin peak fulfills the Bragg condition and one beam of the interferometer is blocked to remove any possible path interference effects. One DC spin-rotator is put in front of the interferometer, and one behind the interferometer. The supermirror is placed in front of the O-detector so that only up-spin neutrons arrive at the detector. Now four intensity measurements are performed: first with both DC spin-rotators turned off $I(off, off)$, the second with the first set

	Peak	FWHM
No Coil	1.000	1.000
Al Wire	0.56(1)	1.68(4)
Al Ribbon	0.80(1)	1.16(2)
Cu Ribbon 3mm width	0.84(1)	1.11(2)
Cu Ribbon 4mm width	0.85(1)	1.16(2)

Table 3.1: Rocking curve comparison with DC spin-rotator coils made of different materials, normalised to the empty setup.

to induce a rotation of π $I(on, off)$, third the second DC spin-rotator set to π spin rotation and the first turned off $I(off, on)$, and fourth both DC spin-rotators set to π spin rotation $I(on, on)$. Using the equations below the efficiencies (ξ_{front} , ξ_{back}) of both DC spin-rotators and the overall degree of polarization P are calculated,

$$\xi_{front} = \frac{I(on, on) - I(on, off)}{I(off, off) - I(off, on)}, \quad \xi_{back} = \frac{I(on, on) - I(off, on)}{I(off, off) - I(on, off)},$$

$$P = \sqrt{\frac{\left(I(off, off) - I(on, off)\right)\left(I(off, off) - I(off, on)\right)}{I(off, off)I(on, on) - I(on, off)I(off, on)}}$$
(3.83)

The measurement results for the four normalized intensities needed for the evaluation of the degree of polarization and the efficiencies of the DC spin-rotators are given in table Tab.3.2.

The degree of polarization is measured to be $P = 0.999(6)$ or for simplicity $P > 0.993$, the efficiency of the first DC-coil is $\xi_{front} = 0.98(1)$ and efficiency of the second coil is $\xi_{back} = 0.98(1)$. The degree of polarization using a DC spin-rotator with a aluminium wire is $P < 0.95$.

	cps	err
$I(off, off)$	110.3	± 0.96
$I(on, off)$	1.39	± 0.11
$I(off, on)$	1.26	± 0.10
$I(on, on)$	107.7	± 0.95

Table 3.2: Intensities measured for the evaluation of the degree of polarization and the efficiencies of the DC spin-rotators.

3.5 Adjusting the setup

The S18 instrument at the ILL in Grenoble is a user facility which is used for interferometric experiments as well as ultra small angular scattering (US-ANS) experiments. Both types of experiments can be performed at different neutron wave length and therefore different Bragg angles. Both types of experiments can either use polarized or unpolarized neutron beams. As a consequence the setup has to be realigned, partly rebuilt, and adjusted from scratch for every measurement cycle. The process of adjusting the setup from scratch to the first measurement take two scientists between 10 and 14 days. The actual setup is placed on a vibration damping optical bench in a concrete housing, to reduces thermal fluctuations.

Monochromator

First the monochromator, with a triple-fold reflection, that reflects the neutrons from the neutron guide onto the interferometer, needs to be adjusted. The reflection plane used in the monochromator is the (2,2,0) crystal plane. It is important that the beam coming from the monochromator has the desired Bragg angle of $\theta = \pi/6$. The neutron beam also needs to be horizontal, otherwise it could not pass the small gap in the yoke of the magnetic prisms

used for polarization. A laser level is utilized, which projects a height adjustable horizontal line, to set the detector to the correct height, as seen in Fig.3.17. The monochromator is adjusted so that as many neutrons as possible arrive at the detector while satisfying the requirement mentioned above.

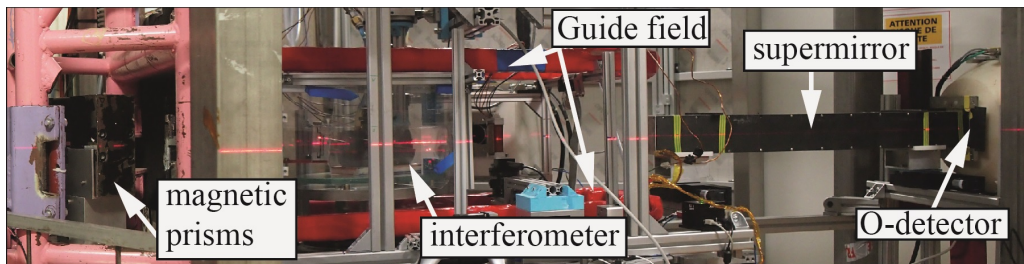


Figure 3.17: Pictures of the setup with red laser line of the laser level tool.

Adjusting the tilt angle of the interferometer

Next the interferometer is placed in the beam path and adjusted. First the Bragg condition must be fulfilled. This is achieved by measuring a rocking curve by rotating the interferometer along the vertical axes while only one path the neutrons can take through the interferometer is open, the other is blocked by cadmium beam stoppers. Usually path I is blocked, to reduce background at the O-detector, caused by the direct beam coming from the monochromator. Second the so-called ρ -axes, i.e. the tilt angle of the interferometer, needs to be adjusted, which is the rotation of the interferometer along the beam direction. The goal is to get the (2,2,0) crystal plane of the interferometer parallel to the reflection plane of the monochromator. The measurement is executed by a measuring rocking for each position of the ρ -axes. This increases the peak intensity and makes the FWHM of the rocking curve narrower. The narrower the rocking curve the higher the achievable degree of polarization as described above.

Phase shifter and contrast of the interferogram

Now the phase shifter is inserted and both beam path are opened to allow accessing interference fringes. In this experiment a 3 mm thick slab of sapphire (Al_2O_3) is used as the phase shifter. The interference pattern is measured by rotating the phase shifter, which induces a phase shift χ between the two paths of the interferometer. A typical interference pattern is shown in figure Fig.3.18. The function $g(\chi) = y_0 + A \cos(f\chi + \phi)$, with the offset y_0 , the

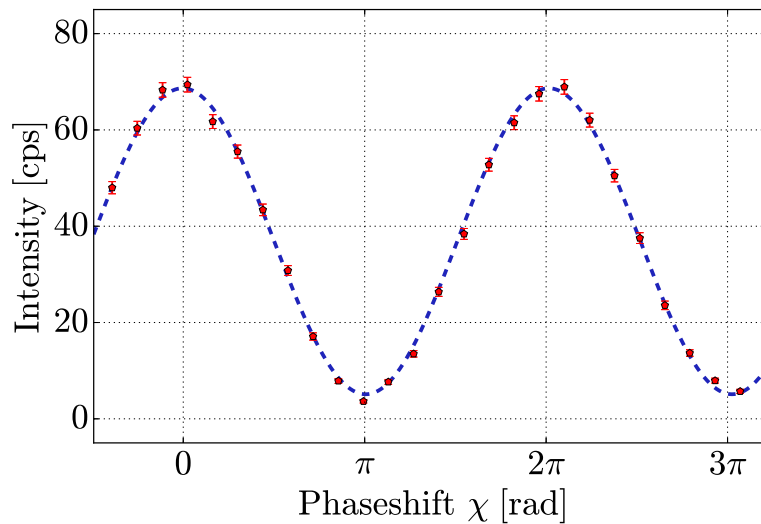


Figure 3.18: *Interference pattern showing a contrast of $C = 0.86$.*

amplitude A , the frequency f , and a phase ϕ , is least square fitted to the measurement data. The contrast is calculated by $C = A/y_0$.

Depending on the position where the neutron beam passes through the interferometer, different contrasts emerges. By opening of the aperture, the contrast of the interference patterns is decreased, due to phase and contrast fluctuations across the area covered by the neutron beam. In order to reduce this effect, a small aperture is chosen of $3 \cdot 3 \text{ mm}^2$ for the actual measurement of Bell's inequality. To find the spot on the interferometer that provides the highest contrast a raster scan is performed. The aperture is moved in

1 mm steps over a range of 8 mm wide and 3 mm height, at every position a interference pattern is measured. In figure Fig.3.19 the obtained contrasts of the interferograms are plotted. In height 0 mm at position 13 mm and 14 mm the highest contrast is found and the aperature is set to position 13.5 mm and 0.0 mm. The height 0 mm actually corresponds to 12 mm above the basis of the interferometer. A lower position of the aperture would provide enough space for the Larmor accelerator.

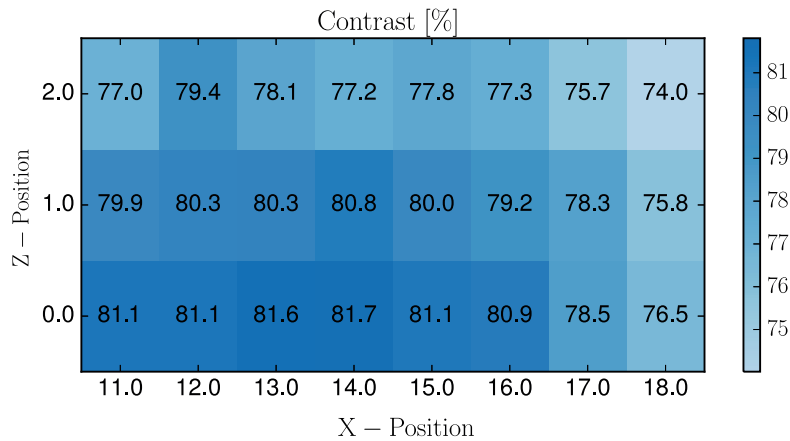


Figure 3.19: Results of a raster scan, where the contrast is plotted against the position of the aperture.

During the adjustment and installment of each of the elements of the setup, the housing of the interferometry setup is opened often, this results in thermal perturbations and reduces the contrast of the interferometer. After the setup is adjusted completely no perturbations occur and the whole setup transits into stable thermal conditions over a time period of one to three days. When the setup is in a thermal stable condition, contrast of $C > 0.91$ are measured.

In figure Fig.3.20 the mean intensity y_0 is plotted against the position of the aperture. The maximum intensity is at the position $x = 13$ mm and $z = 0$ mm which is close to the position of the highest contrast. If they would

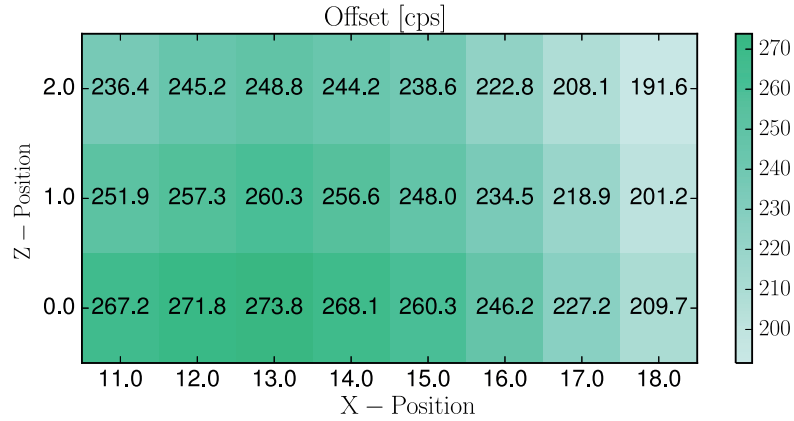


Figure 3.20: Results of a raster scan, where the contrast is plotted against the position of the aperture.

differ considerably, the interferometer would be moved, so that the region of highest contrast of the interferometer matches the region of highest intensity of the neutron beam.

Guide field

Now the polarimetric part of the setup is adjusted. To avoid depolarization of the neutron spin the guide field must be switched on, during the measurements for the adjustment of the spin manipulation devices. First the magnetic field is set to the desired field strength of 12 G using a Gauss-meter. To cool the coils of the guide field a temperature regulating water pump runs tempered water through the guide field coil frames. Depending on the temperature of the cooling water the contrast of the interferometer changes, but since the guide field coils are well insulated the change in contrast is small. A temperature scan is performed, where the contrast is measured at different temperatures of the cooling water for the guide field. the result is shown in figure Fig.3.21 The temperature is set to 21.25 °C.

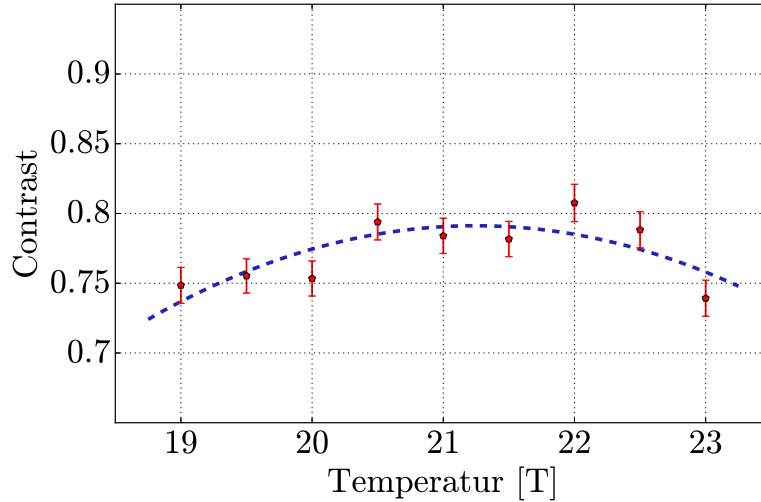


Figure 3.21: Contrasts measured at different temperatures of the cooling water of the guide field. A temperature of 21.25°C provides the best performance, which is marked with a dashed green line. The insulation of the guide field coils results in a small dependency of the contrast on the change in temperature.

Birefringent prisms

After the position of highest contrast is found the birefringent magnetic prisms, working as a polarizer, are put in place. The function principles of the prisms are described in section 2.3.1. The two prisms can be translated horizontally perpendicular to the beam direction, depending on their position the angular separation between up-spin and down-spin component changes. The best position for the prisms can be evaluated by blocking one beam in the interferometer to avoid interference effects and measuring rocking curves at different positions of the prisms. First the best position for the prisms closer to the monochromator is adjusted, followed by adjusting the best position of the second prism with the first in place. With the prisms in the beam two peaks are visible in the rocking curve, as can be seen in figure

Fig.3.13. The measurement data is fitted with the function

$$g(\theta) = y_0 + \frac{A}{\sqrt{2\pi}\Delta} \left(e^{-\frac{(x-x_0)^2}{2\Delta^2}} + e^{-\frac{(x-x_0-\delta x_0)^2}{2\Delta^2}} \right), \quad (3.84)$$

with the offset y_0 , the peak height A , the peak width Δ , the position of the first peak x_0 and the separation of the peaks δx_0 . The best position for the prisms is found when the peak separation δx_0 becomes largest. An angular separation of the up-spin and the down-spin component of $2.3 \cdot 10^{-5}$ rad is found in our setup. Due to the small acceptance angle of the Bragg-reflection of the interferometer these two peaks can be clearly separated, and the chosen peak has a degree of polarization of $P > 0.993$.

Supermirror

Next the supermirror spin analyzer is put in the beam line and adjusted. The correct height of the supermirror is adjusted using the laser level. The supermirror has a 20 mm entry window and exit window and is 0.86 m long, which results in an acceptance angle of 0.05 rad. To adjust the supermirror two translation stages, one at the front and the other at the back of the supermirror, translate the supermirror perpendicular to the beam line. This allows for adjusting angle and lateral position of the supermirror. When the maximal intensity is found the supermirror is adjusted and the spin manipulation devices can be installed and adjusted.

DC spin-rotator

The DC spin-rotator in front of the interferometer needs to be adjusted first, since it is needed to adjust the other components. For adjusting a DC spin-rotator three steps are required: first a rough adjustment of the field in $\pm x$ -direction without compensation field; second scanning the compensation field in $-z$ direction with the field in x -direction set to the estimated current

needed for a rotation of $\theta = \pi$; and third a precise scan of the field in $\pm x$ -direction with the compensation field active. For all these measurements one path is blocked in order to avoid path interference during the measurement.

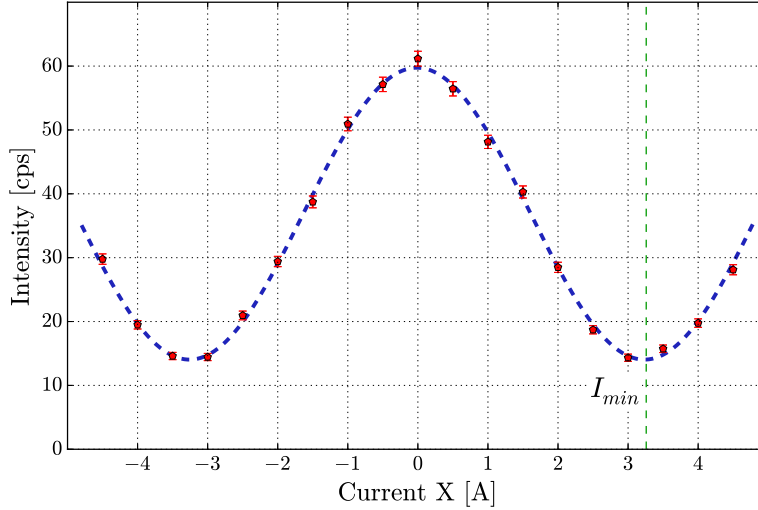


Figure 3.22: Plot of the intensity versus the current in the coil of the DC spin-rotator producing a field in $\pm x$ -direction, with out a B_z compensation field. The flip ratio is 4.25 and the efficiency 0.76

The first scan of the field in $\pm x$ -direction is depicted in figure Fig.3.22. A cosine function is fitted to the obtained data. Without a compensation field the DC spin-rotator shows poor flip ratio of $I_{max}/I_{min} = 4.25$, which translates to a efficiency of $\xi = 0.62$. It is important that the field in $\pm x$ -direction is square to the magnetic guide field. If this is not the case the minimum on one side is lower than on the other and the cosine curve is shifted in one direction. In this case the coil needs to be tilted until both minimums are on the same height and the cosine function has phase $\phi = 0$ i.e. the maximum of the fit function is at $I = 0$ A. The required current for the measurement of the compensation field is extracted out of the fit results to be $I_{min} = 3.259$ A.

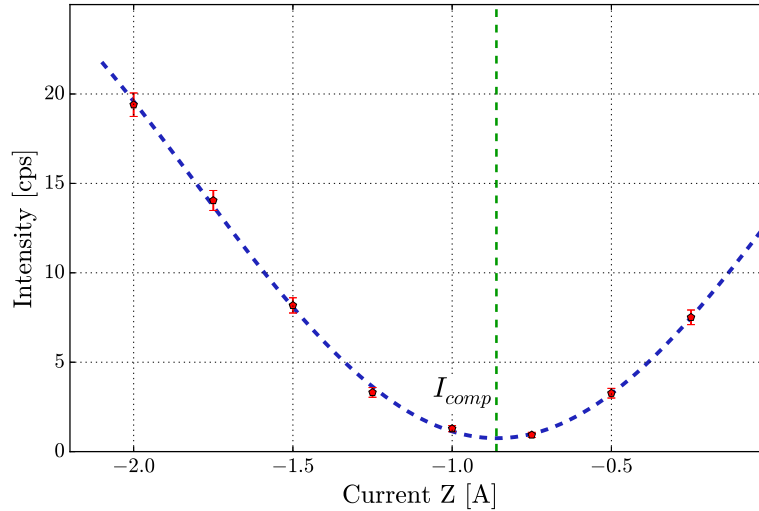


Figure 3.23: Scan of the compensation field of the DC spin-rotator, with roughly estimated field in y -direction applied.

With the current in the coil in x -direction set, a scan of the compensation field is executed. Since the field needs to be applied in $-z$ -direction, negative currents must be applied. The scan is shown in plot Fig.3.23, with a sine curve fitted to the data. The minimum given by the fit result gives the strength needed for the compensation field $I_{comp} = -0.861$ A.

With the compensation field established a precise scan of the field in $\pm x$ -direction can be performed. The result of this scan is depicted in figure Fig.3.24, with a cosine curve fitted to the data. The flip ratio of this scan is $FR = 99.8$ and the corresponding efficiency is $\xi = 0.98$. The currents for specific spin-rotation angles θ are derived from the fit. The current needed for a rotation of π , i.e. a spin flip, is $I(\pi) = 3.463$ A, which results in a polarization of the beam in the $-z$ -direction or a spin state of $|s_{z-}\rangle$. For a spin state in $+y$ -direction or a $|s_{y+}\rangle$, as desired for the experiment a current of $I(\pi/2) = 1.732$ A is needed.

The DC spin-rotator behind the interferometer is adjusted in the same

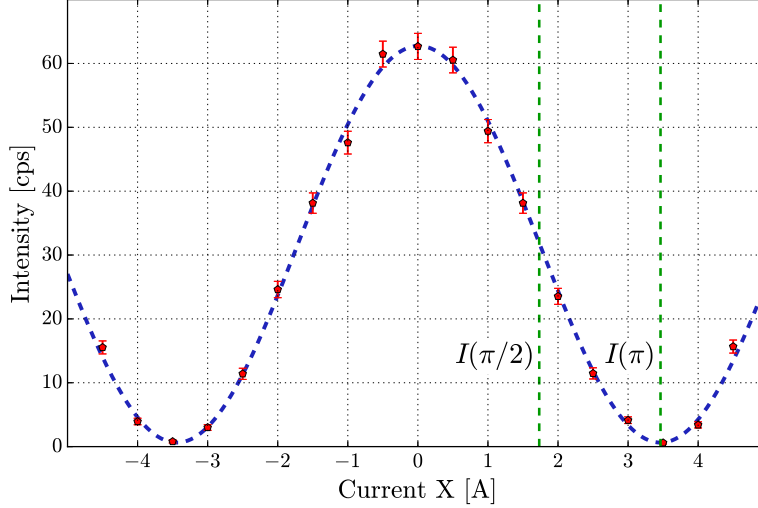


Figure 3.24: Plot of the precise scan of the field in $\pm x$ -direction of the DC spin-rotator, with the compensating field in $-z$ -direction applied.

manner as the DC spin-rotator in front of the interferometer, and has about the same flip ratio of $I_{max}/I_{min} = 99.8$. To select any possible spin direction for measuring at the detector an other parameter additional to the current in the coil in $\pm x$ -direction needs to be applied; the current only gives a rotation around the x-axes i.e. the polar angle θ . By moving the coil back and forth along the beam path the azimuth angle ϕ can be adjusted additionally, due to Larmor precision by the guide field. Therefore the DC spin-rotator behind the interferometer is put on a translation stage to be able to adjust the azimuth angle ϕ . A scan is performed where the DC coil in front of the interferometer is set to $I_{front}(\pi/2)$, the DC coil behind the interferometer is set to $I_{back}(-\pi/2)$, and one path in the interferometer is blocked. While moving the coil back and forth the intensity at the O-detector oscillates. At the position of maximal intensity the $|s_{y+}\rangle$ spin component is selected for detection, at the position of minimum intensity the $|s_{y-}\rangle$ spin component is selected, and on the positions in between the two spin components $|s_{x+}\rangle$

and $|s_{x-}\rangle$ are selected respectively. This is shown in plot Fig.3.25. The positions for the respective spin component selections are marked by dashed green lines. To select the $|s_{z+}\rangle$ spin component the DC coil can be turned off $I_{back}(0) = 0$, for the $|s_{z-}\rangle$ component the DC coil is set to $I_{back}(\pi)$ at any position of the translation stage.

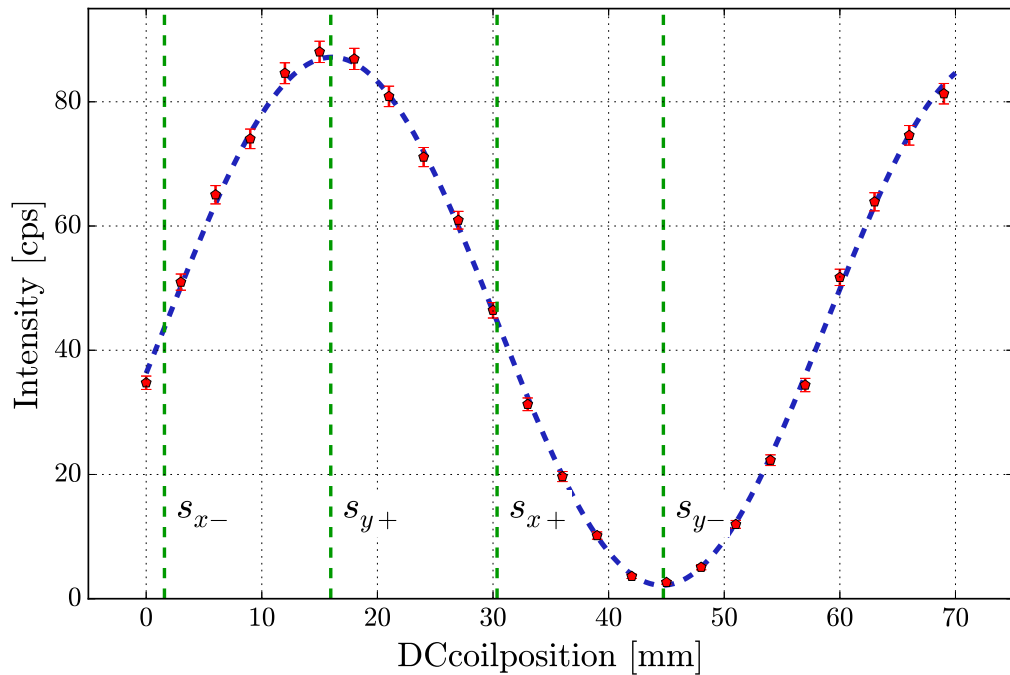


Figure 3.25: Plot of the intensity modulation as a function of the position of the DC spin-rotator coil behind the interferometer. The dashed green lines show the positions i.e. the azimuth angle $\phi = 0, \pi/2, \pi, 3\pi/2$ for selecting the $|s_{x\pm}\rangle$ and $|s_{y\pm}\rangle$ respectively.

Larmor accelerators

After the DC spin-rotators are adjusted the Larmor accelerators are placed in the interferometer. The Larmor accelerators need to be cooled when in use, since the 3D printed plastic can melt and the coils deform when they

get to hot ($> 80^\circ\text{C}$). Despite the fact that only little power is applied to the Larmor accelerators, about 1 W, this power output takes place in a small insulated volume of about 4 cm^3 . To avoid negative influences of the water temperature on the interferometer a temperature scan of the cooling water of this device is performed. The results of this scan is shown in figure Fig.3.9. The temperature, which allows for the highest contrast, is chosen at 25.15°C .

Now beam in path I of the interferometer is blocked and a current versus intensity scan can be performed. To do so the DC spin-rotator in front of the interferometer is set to $I_{front}(\pi/2)$ and the DC spin-rotator in the back is set to select the $|s_{y+}\rangle$ component for measurement. By applying field additional to the guide field in $\pm z$ -direction the azimuth angle ϕ of the spin polarization can be adjusted, which results in a change in intensity at the detector as seen in Fig.3.26.

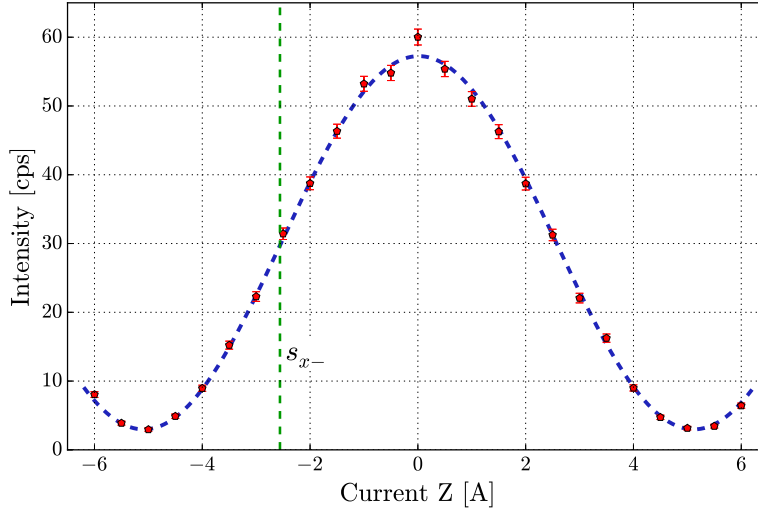


Figure 3.26: Plot of the intensity modulation as a function of the current in the Larmor accelerator in path II. The current needed for a rotation of $\phi = \pi/2$ is marked with a dashed green line.

The current of $I_{LA}(\pi/2) = -2.559\text{ A}$ for a rotation of $\phi = \pi/2$ is calcu-

lated from the least square fit parameters of the cosine function. By rotating the $|s_{y+}\rangle$ spin state by $\phi = \pi/2$ the $|s_{x-}\rangle$ state in path II is generated. Note that the maximum is exactly at zero current, since this path was used to adjust the DC spin-rotators. The flip ratio measured is $I_{max}/I_{min} = 22$ or an efficiency of $\xi = 0.91$ is obtained respectively. Considering that this efficiency is reduced considerably by the efficiencies of the two DC spin-rotators and the degree of polarization, the efficiency of the Larmor accelerator itself is extracted to be $\xi \approx 0.96$.

The Larmor accelerator in path I is adjusted in the same way, but with the beam stopper put in path II . The results of the scan is shown in figure Fig.3.27, with a cosine curve fitted to the data. To establish the $|s_{x+}\rangle$ state in path I a rotation of $\phi = -\pi/2$ is needed. The corresponding current of $I_{LF}(-\pi/2) = 2.766$ is marked with a dashed green line in the graph. Note

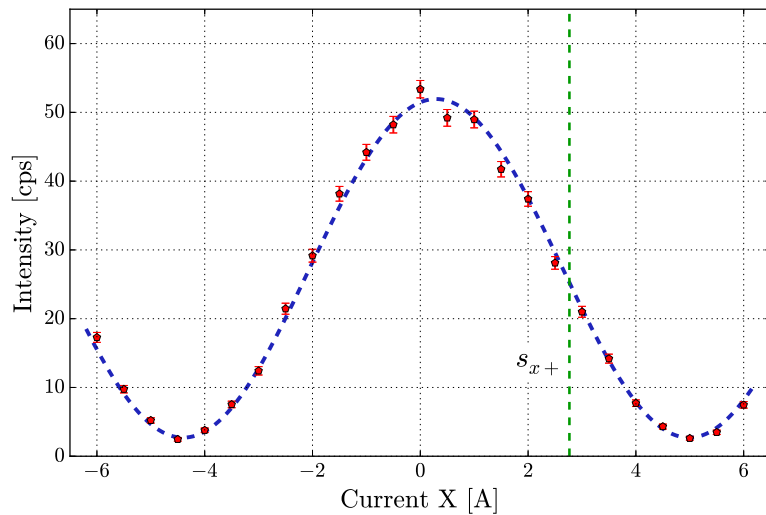


Figure 3.27: Plot of the intensity modulation as a function of the position of the DC spin-rotator coil behind the interferometer. The dashed blue lines show the positions i.e. the azimuth angle ϕ for selecting the $|s_{x\pm}\rangle$ and $|s_{y\pm}\rangle$ respectively.

the small shift of the maximum of the cosine curve to the right by $\phi \approx \pi/16$, which is caused by a small in-homogeneity of the guide field. Given the path length of roughly 100 mm in which the two beam path are separated, the mean guide field difference between path I and path II is about 0.2 G or 1.5% of the guide field strength.

By using the evaluated efficiencies of each element of the setup, an overall efficiency is calculated to be $\xi_{setup} = 0.84$. This gives an estimate for the maximal achievable violation of Bell's inequality of $S(\xi_{setup}) = 2\sqrt{2} \cdot \xi_{setup} = 2.376$. This rough estimation can also be applied in a similar manner to other measurements performed utilizing this setup. In earlier measurements the overall efficiency of the old setup was about $\xi_{old} = 0.72$, as calculated from the magnitude of the violation of Bell's inequality.

Now all devices needed for the measurement of Bell's inequality are adjusted. However, it is possible to adjust the setup differently in a large variety of settings. The incoming state can be set to any point on the Bloch sphere, since the DC spin-rotator in front of the interferometer can also put on a translation state, which allows for setting the azimuth angle ϕ . The DC spin-rotator is able to select any spin component for measurement. Using the Larmor accelerators the degree of entanglement can be adjusted from not entangled at all, to a fully entangled state. The Larmor accelerators are also used to mark the paths in weak measurements as done in other measurements [Denkmayr et al., 2014, Sponar et al., 2015, Denkmayr et al., 2017, Waegell et al., 2017] using this setup.

3.6 Results

The Bell state $|\psi_{Bell}\rangle = (|s_{x+}\rangle|I\rangle + |s_{x-}\rangle|II\rangle)/\sqrt{2}$ is generated as described above. Four phase shifter scans are performed for one data set, each at different settings for the spin selection angles $\alpha_+ = 0, \alpha_- = \pi, \alpha'_+ = \pi/2$, and

$\alpha'_- = 3\pi/2$. Since the measurement is very sensitive to temperature fluctuations the four phase shifter scans are convoluted into one measurement: the phase shifter is set to the first measurement position and a count rate is measured for each spin direction α . Then the phase shifter is moved to the next position and again count rates for all four spin directions are measured. By doing so eventual phase drifts are spread evenly onto all four phase shifter scans and no relative phase drift between the phase shifter scans occurs. However, temperature drifts may result in a change of the period of the interference patterns, but this does not compromise the measurement results. The results of such a measurement of a set of interference patterns for each spin direction α is shown in figure Fig.3.28. The dashed green lines show the phase settings needed to evaluate result of the Bell measurement. The different mean intensities obtained for the measurements in $\alpha_- = \pi$ direction and $\alpha'_- = 3\pi/2$ direction, is a result of a miss alignment. Either the generated state is not a perfect Bell state, or the measurement directions for α_i are not correctly adjusted.

Two sets of data are collected, so that the measurement time for each measurement is shorter and less susceptible to temperature fluctuations. One set is measured 60 s per phase and spin selection setting, the other 90 s. This two sets are evaluated separately and an average over the two results is calculated to reduce statistical error.

The data is normalized to the time counted and least square fitted with a sine curve $g(x) = y_0 + A \sin(f\chi + \phi)$, the standard deviation $\sigma = \sqrt{n}$ of the count rate n is used as a weighting for the fit. The values given by the fit functions for the phase settings $\chi_+ = \pi/4$, $\chi_- = 5\pi/4$, $\chi'_+ = 3\pi/4$, and $\chi'_- = 7\pi/4$ give the values for the coincidence rates $N(\alpha_{\pm}, \chi_{\pm})$. The error of the coincident rates can be calculated using the variance of the fit parameters. The S value is calculated as given in the equations Eq.3.74 and

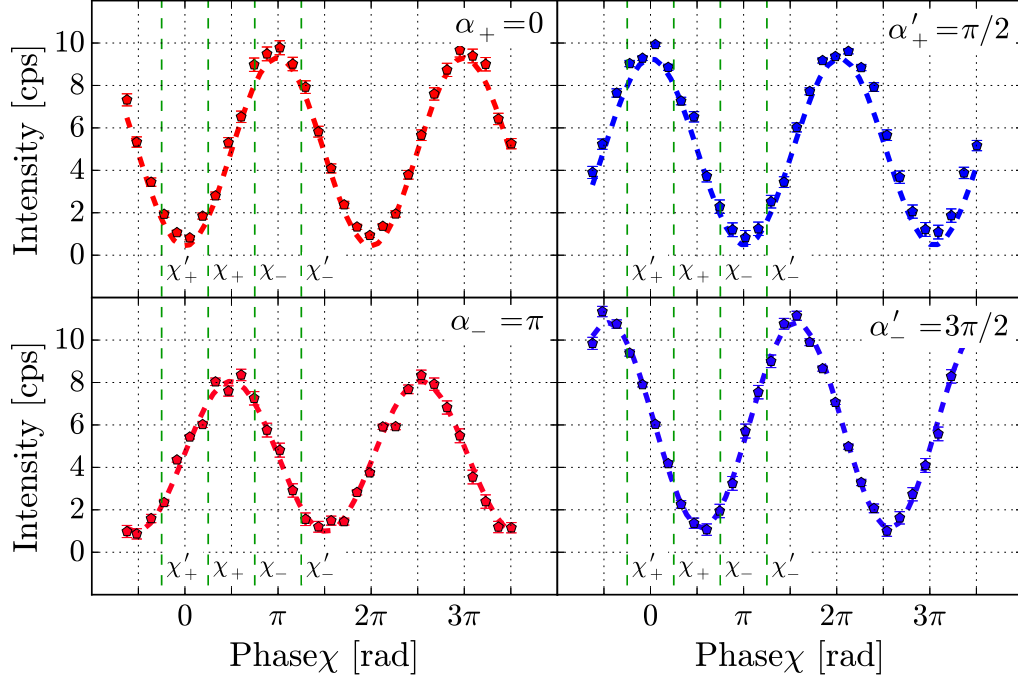


Figure 3.28: *Interference patterns of the Bell measurement. The four plots show interference patterns at different measurement directions α . The dashed green lines mark the phase settings χ used for the evaluation of the expectation $E(\alpha, \chi)$ values.*

Eq.3.70. Using error propagation

$$\sigma_{Bell} = \sqrt{\sum \left(\frac{\partial S(x_i)}{\partial x_i} \sigma_i \right)^2}, \quad (3.85)$$

the standard deviation of the measurement result is calculated. We obtain the final result,

$$S = 2.365 \pm 0.013, \quad (3.86)$$

which gives a violation of 28σ , well above the classical limit of $S < 2$.

3.7 Discussion

The new devices used in the setup considerably improve the abilities of the polarized neutron interferometer setup. Using a new coil design for the DC spin-rotators and a triple-fold monochromator, a degree of polarization of the incoming beam of $P > 0.993$ is achieved. The newly designed spin manipulation devices allow for very accurate adjustment, as well as high flexibility of the setup. New Larmor accelerators allow the reduction of thermal disturbances on the interferometer. Dephasing is not an issue since no material is put in the beam path inside the interferometer. This results in high contrasts of $C > 0.91$.

The value of $S = 2.365 \pm 0.013$ for the Bell-like inequality measurement, is 28σ above the limit of 2 for noncontextual hidden variable theories. It therefore proves, that no contextual hidden variable theory can reproduce the predictions of quantum mechanics. This clear violation of the Bell-like inequality is much higher than previous measurements using neutron interferometry [Hasegawa et al., 2003, Erdösi and Hasegawa, 2011], and was achieved in a fraction ($\sim 1/10$) of the measurement time used in the other experiments.

Chapter 4

Which-way measurement

4.1 Introduction

The first double slit experiments by Young 1802, was performed to show the wave theory of light, and to contradicted Newton's corpuscular theory. In the double slit experiment a coherent light source illuminates a plate with two narrow parallel slits. A screen is placed behind the the plate, on which interference patterns become visible. Experiments using massive particles such as electrons [Davisson and Germer, 1927, Jönsson, 1961, Tonomura, 1987] or neutrons [Rauch et al., 1974] also showed interference fringes. Later on experiments using even larger particles like atoms [Cronin et al., 2009], or even large molecules [Arndt et al., 1999, Nairz et al., 2003] showed interference fringes in double-slit experiments.

However, there is an important distinction between the classical version of the double-slit experiment, e.g. using a beam of light, and the quantum mechanical version, using massive particles: In a classical experiment, using electromagnetic waves, interference fringes are instantaneously visible on the screen. In a quantum mechanical experiment using massive particles only statistically distributed detection-spots appear at the first stage, and inter-

ference fringes become visible only after an accumulation of enough particles. The question arises which way a particle took in a double slit experiment.

When which-way information is obtained by putting a detector in one path the interference patterns vanish, since the detected particles can no longer interfere with the particles traveling through the other path. This led to the complementarity principle formulated by Bohr [Bohr, 1928], which states that a quantum system either shows particle or wave properties. A simple experiment proposed by Ghose [Ghose et al., 1991] with a simple twist as suggested by Bose [Bose, 1927] illuminates issues with the complementarity principle by Bohr. Let's consider a 50:50 beam splitter and two detectors in the beam in transmitted direction D_t and one in the beam in reflected direction D_r . Single photons passing through the beam splitter can either be detected at D_t or D_r , the detectors never click at the same time, which is perfect anti-coincidence and particle behavior. When a biprism with a small tunneling gap is placed in one path, only photons that tunneled, i.e. a wave property, can be detected at the respective detector. Englert introduced the duality relation $D^2 + V^2 \leq 1$ [Englert, 1996], which represents a trade off between path information, or distinguishability D , and visibility V of the interference fringes, which allows for both particle and wave properties in a system: the more information is extracted about the path, the less interference fringes are visible. Quantum eraser experiments show that, if which-way information is extracted the visibility is reduced up to the point of no visibility, when the which-way information is 'erased' afterwards the visibility is regained [Herzog et al., 1995, Walborn et al., 2002].

Many theoretical discourses and experiments [Greenberger and Yasin, 1998, Englert, 1996, Dürr et al., 1998] tried to push limits to obtain as much path information as possible while still allowing for interference effects. New approach to which-way measurements is the two-state vector formalism [Watanabe, 1955, Aharonov et al., 1964, Aharonov and Vaidman,

1990, Vaidman, 2013]. In the two-state vector formalism each particle is described by a backward-evolving quantum state created at the detector, in addition to the standard, forward-evolving wave function created at the source. The two-state vector formalism implies that a particles can have a local observable effect only if both the forward- and backward-evolving quantum waves are nonvanishing at this location. The chain of causality in the two-state vector formalism is the combination of the *forward causality* of the particle coming from the source, and the *backward causality* of the particle from the future, i.e. a particle traveling back in time.

In 2013 a experiment was presented by Danan et al., using this two-state vector formalism to explain the results of a which-way measurement in a laser Mach-Zehnder interferometer [Danan et al., 2013]. They make the claim, that *'The photons do not always follow continuous trajectories. Only the description with both forward and backward evolving quantum states provides a simple and intuitive picture of pre- and postselected quantum particles.'*

We present a which-way experiment using a double-loop interferomete, and apply small time-dependent which-way marking by resonance-frequency spin-rotators. The which-way information is extracted via Fourier-analysis of the time-dependent detector signal behind the interferometer. We give a simple picture, explaining the observed results: In our picture cross terms between the main (time-independent) component and the which-way marked components of the wave function in the interferometer are responsible for the observed effects. This picture provides a deeper understanding of the physics involved and gives quantitative results, which is missed the two-state vector formalism, in the form presented by Danan et al.

4.2 Theory

In this experiment a four plate double-loop interferometer is used that provides three spatially separated paths which are recombined at the fourth plate and interfere with each other. A scheme of the interferometer is depicted in Fig.4.1.

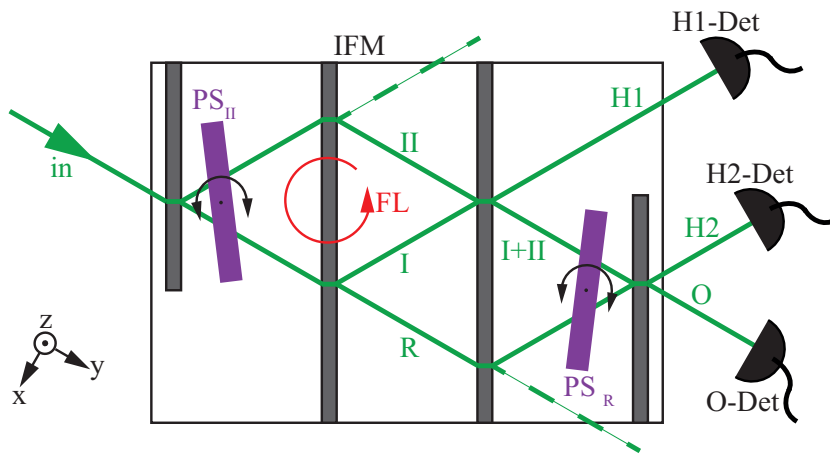


Figure 4.1: *Double-loop interferometer with three beam paths. The neutron beam is depicted in green. The front-loop (FL) is composed of two beams in path I, and path II. A phase shifter (PS_{II}) tunes the phase of the front loop. One outgoing beam in path $I+II$ is combined with the reference beam in path R . The phase of the reference beam in path R is tuned using phase shifter PS_R . Three detectors O , $H1$, and $H2$ measure the intensity of the outgoing beams in paths O , $H1$, $H2$ respectively.*

The three path can be described as a normal single-loop Mach-Zehnder interferometer with an additional beam (reference beam) that interferes with one of the outgoing beams of a single-loop interferometer (front-loop). Two phase shifters are used the first one (PS_{II}) tunes the phase of the front loop, the second phase shifter (PS_R) tunes the phase of the reference beam relative to the outgoing beam it interferes with. The incoming wave function

in path in is normalized $I_{in} = |\psi_{in}|^2 = 1$. Each plate acts as a beam splitter, as described in section 2.2. Between second and third plate three separate beams are present with corresponding wave functions and phases $\frac{1}{2}e^{i\chi_I}\psi_I$, $\frac{1}{2}e^{i\chi_{II}}\psi_{II}$, and $\frac{1}{2}e^{i\chi_R}\psi_R$. At the third plate beams in path I and path II are recombined to

$$\frac{1}{2}e^{i\chi_{I+II}}\psi_{I+II} = \frac{1}{2\sqrt{2}}e^{i\chi_I}\psi_I + \frac{1}{2\sqrt{2}}e^{i\chi_{II}}\psi_{II}, \quad (4.1)$$

with $\chi_{I+II} = \text{Arg}(e^{i\chi_I} + e^{i\chi_{II}})$. The intensity $I_{I+II} = |\psi_{I+II}|^2 = \frac{1}{4}[1 + \cos(\chi_I - \chi_{II})]$ is analogous to the intensity of a single-loop interferometer. By tuning the phases of beams in path I and path II the intensity of the beam in path $I + II$ can be tuned between $0 \leq I_{I+II} \leq 1/2$ in relation to the initial intensity I_{in} . At the fourth plate the beam in path $I + II$ is combined with the reference beam in path R and compose the beam in path O . The wave function in path O can be written as

$$\psi_O = \frac{1}{2\sqrt{2}}e^{i\chi_{I+II}}\psi_{I+II} + \frac{1}{4}e^{i\chi_R}\psi_R. \quad (4.2)$$

The intensity at the O -detector is given by

$$I_O = |\psi_O|^2 = \frac{1}{16}[3 + 2\cos(\chi_I - \chi_{II}) + 2\cos(\chi_I - \chi_R) + 2\cos(\chi_{II} - \chi_R)]. \quad (4.3)$$

In practice only two phase shifters are needed, because an overall phase can not be resolved, only the relative phases between the beams in each path are of importance. Therefore the phase of the beam in path I can be assigned to be zero, while the phases of the beams in paths II and path R can be tuned with the phase shifters PS_{II} and PS_R respectively.

To obtain which-way information which-way markers are facilitated. This markers should make a small imprint on the wave function without much disturbance on the system, so that coherence is conserved, and must allow for a accurate readout behind the interferometer. In this experiment which-way markers are inserted at four positions in the interferometer. To mark four

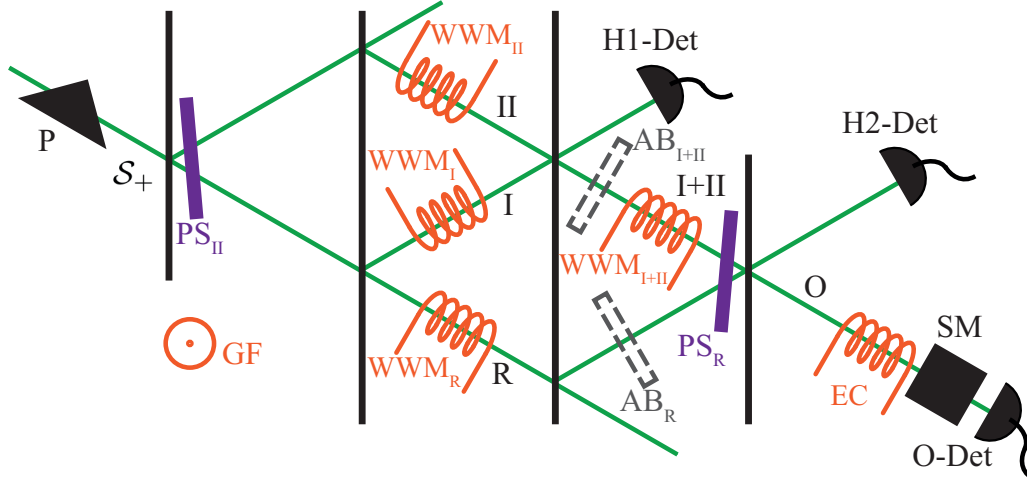


Figure 4.2: A schematic depiction of the setup. The neutrons are polarized in positive z -direction $+z$ by passing two magnetic prisms (P) before entering the four plate interferometer. The first three plates provide a regular Mach-Zehnder interferometer consisting of paths I and II . The fourth plate enables a reference beam R to interfere with the outgoing beam of the interference loop in front in path $I + II$. Phase shifter PS_{II} tunes the phase of the front-loop and phase shifter PS_R tunes the phase of the reference beam. Four which-way markers (WWM_i), and two slots for absorbers (AB_i) are placed in the interferometer. An energy compensator (EC) and a supermirror (SM) are placed in front of the O -detector.

different paths (I , II , R , and $I + II$) in the interferometer simultaneously the usual marking, like absorbers or static spin rotations, used in previous experiments [Denkmayr et al., 2014, Sponar et al., 2015] are not suitable: they do not allow extraction of which-way information of four paths simultaneously.

In the presented experiment resonance-frequency spin-rotators are chosen, since they can provide distinguishable which-way marking for each path. By applying a small energy shift of different magnitude in each path, which leads intensity modulation in time, with different frequencies, attributed to each

path. Since every path is marked with a different energy shift $\Delta E_i = \hbar\omega_i$, which-way information can be derived by a Fourier-analysis of the intensity modulation in time at the O-detector. A peak at the frequency ω_i , found in the power spectrum, is clear evidence that neutrons have taken path i . The physical principles of a resonance-frequency spin-rotator are described in section 2.3.6.

A scheme of the setup is depicted in Fig.4.2. The incoming beam is spin-polarized in positive z-direction represented by s_{z+} , being the positive eigen-state of the spin operator $\widehat{\mathcal{S}}_z = \frac{\hbar}{2}\widehat{\sigma}_z$. (For easier readability the notation is changed in comparison to chapter 4.) The spin polarization is achieved by two birefringent prisms (P) as described in section 2.3.1. The down-spin component is represented by s_{z-} , which is the negative eigen-state of the spin operator $\widehat{\mathcal{S}}_z = \frac{\hbar}{2}\widehat{\sigma}_z$. Two phase shifters (PS_{II} , PS_R) are inserted in the interferometer, and there are two slots for absorbers (AB_{I+II} , AB_R) are between the third and fourth plate of the interferometer. Four which-way markers (WWM_I , WWM_{II} , WWM_R , WWM_{I+II}) are placed inside the interferometer for which-way marking, and one resonance-frequency spin-rotator (EC) behind the interferometer for energy compensation, as described below. A supermirror spin-analyzer (SM) is put in front of the O-detector. Two more detectors H1-Det, and H2-Det monitor the phases of the front loop and the reference beam.

The design of the resonance-frequency spin-rotators is described in section 2.3.6. The magnitude of the energy shift $\Delta E_i = \hbar\omega_i$ is tuned by the local guide field and the frequency ω_i of the oscillating field of the corresponding which-way marker. The amount of which-way marking is controlled by a rotation angle α of the neutron-spin. This angle α is chosen to be small enough to reduce perturbation on the wave function due to marking. The unitary transformation $\widehat{U}_{WWM}(\omega, \alpha)$ represents the rotation of the neutron

spin by a resonance-frequency spin-rotators

$$\hat{U}_{WWM}(\omega, \alpha) = \begin{pmatrix} \cos(\alpha/2) & -ie^{i\omega t} \sin(\alpha/2) \\ -ie^{-i\omega t} \sin(\alpha/2) & \cos(\alpha/2) \end{pmatrix}. \quad (4.4)$$

When $\hat{U}_{WWM}(\omega_i, \alpha_i)$ is applied on a wave function $\Psi_i = s_{z+} \otimes \psi_i$ between second and third plate the result is given by

$$\begin{aligned} \Psi'_i &= \hat{U}_{WWM}(\omega_i, \alpha_i) \Psi_i \\ &= \frac{e^{i\chi_i}}{2} [\cos(\alpha_i/2) s_{z+} - ie^{-i\omega_i t} \sin(\alpha_i/2) s_{z-}] \otimes \psi_i \\ &= \frac{e^{i\chi_i}}{2} [s_{z+} - ie^{-i\omega_i t} \sin(\alpha_i/2) s_{z-}] \otimes \psi_i + \mathcal{O}(\alpha_i^2), \end{aligned} \quad (4.5)$$

with $i = I, II, R$. The energy shift results in a time dependent phase of $e^{-i\omega_i t}$. In Fig.4.3 a diagram of the energy levels is depicted. The up-spin component s_{z+} is represented by the solid blue line and the down-spin component s_{z-} by the dashed red line.

The path $I + II$ coming from the front loop is also marked by an energy shift of $\Delta E_{I+II} = \hbar\omega_{I+II}$ by which-way marker WWM_{I+II} between the third and the fourth plate of the interferometer. The wave function Ψ'_{I+II} behind which-way marker WWM_{I+II} is given by

$$\begin{aligned} \Psi'_{I+II} &= \hat{U}_{WWM}(\omega_{I+II}, \alpha) \frac{1}{\sqrt{2}} (\Psi'_I + \Psi'_{II}) \\ &= s_+ \otimes \psi_{I+II} - \frac{i}{\sqrt{2}} \sum_i \sin(\alpha_i/2) e^{-i\omega_i t} e^{i\chi_i} s_- \otimes \psi_i + \mathcal{O}(\alpha_i^2), \end{aligned} \quad (4.6)$$

with $i = I, II, I + II$, and the definition of ψ_{I+II} as in Eq.4.1. The beam in the (marked) path $I + II$ is recombined with the reference beam in the (marked) path R at the fourth plate. The wave function in path O behind the interferometer is given by $\Psi_O = \frac{1}{\sqrt{2}} \Psi'_{I+II} + \frac{1}{2} \Psi'_R$.

Behind the interferometer an energy compensation of $\Delta E_{EC} = \hbar\omega_{EC}$ is performed in path O by resonance-frequency spin-rotator WWM_{EC} to reduce the overall energy shift of the which-way marking, as seen in Fig.4.3. This

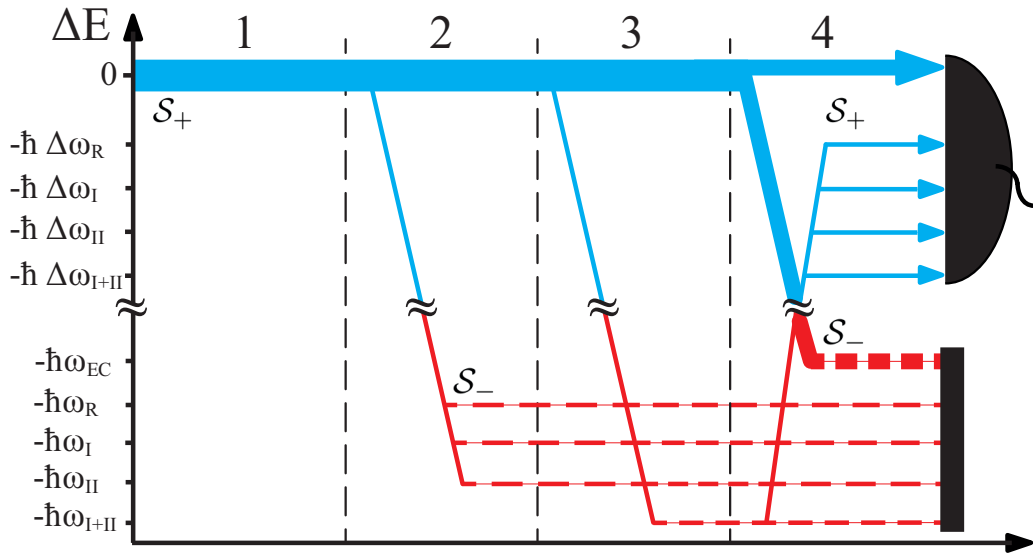


Figure 4.3: Schematic of the energy levels of the neutrons, terms of second order and higher order are neglected. Up-spin components s_+ are represented by the solid green line, down-spin components s_- by the dashed red line. Only the up-spin components reach the O-detector the down-spin components are filtered out by the supermirror. Region 1 represents the beam before entering the interferometer in the energy level of the incoming beam. In regions 2 and 3 represent the which-way marking, that takes place between the second and third plate, and the third and fourth plate of the interferometer respectively. In region 4 the energy compensation behind the interferometer is set.

is achieved by a spin-rotation of $\alpha_{EC}^\pm = \pm\pi/2$ at a frequency of ω_{EC} . The wave function behind WWM_{EC} is given by $\Psi_{EC}^\pm = \widehat{U}_{WWM}(\omega_{EC}, \alpha_{EC}^\pm)\Psi_O$. It is important to point out that only the frequency differences $\Delta E_i = \hbar(\omega_i - \omega_{EC}) = \hbar\Delta\omega_i$ between the initial energy, and the compensated energies, need to be resolved by the O-detector as seen in Fig4.3. Before the beam reaches the O-detector a super-mirror filters out the down-spin component. The super-mirror is represented by the projector $\widehat{\Pi}_{s_{z+}}$ onto the s_{z+} state. The wave function behind the super-mirror $\Psi_{SM}^\pm = \widehat{\Pi}_{s_{z+}}\Psi_{EC}^\pm$ can be written as

$$\begin{aligned}\Psi_{SM}^\pm &= \left[\frac{e^{i\chi_I}}{4\sqrt{2}} \left[1 \mp \sin(\alpha_I/2) (e^{-i\Delta\omega_I t} + e^{-i\Delta\omega_{I+II} t}) \right] \psi_I \right. \\ &\quad + \frac{e^{i\chi_{II}}}{4\sqrt{2}} \left[1 \mp \sin(\alpha_{II}/2) (e^{-i\Delta\omega_{II} t} + e^{-i\Delta\omega_{I+II} t}) \right] \psi_{II} \\ &\quad \left. + \frac{e^{i\chi_R}}{4\sqrt{2}} \left[1 \mp \sin(\alpha_R/2) e^{-i\Delta\omega_R t} \right] \psi_R \right] \otimes s_+ + \mathcal{O}(\alpha_i^2) \\ &= \Psi_{E_0} + \sum_i \Psi_i^\pm + \mathcal{O}(\alpha_i^2),\end{aligned}\tag{4.7}$$

where $\Psi_{E_0} = \frac{1}{4\sqrt{2}}(\Psi_I + \Psi_{II} + \Psi_R)$ is the sum of the main components of the wave functions at energy level $\Delta E = 0$, and Ψ_i^\pm are the energy shifted components, given by

$$\Psi_i^\pm = \mp \frac{e^{i\chi_i}}{4\sqrt{2}} \sin(\alpha_i/2) e^{-i\Delta\omega_i t} s_+ \otimes \psi_i,\tag{4.8}$$

with $i = I, II, R, I + II$. The energy shifted component, i.e. which-way marked component, of the which-way markers WWM_I and WWM_{II} , leaks out of the front-loop interferometer, regardless of settings of PS_{II} . The intensity, up to first order of α , can be calculated by summing up the unchanged energy component Ψ_{E_0} and the individual cross terms between the initial energy components and the marking components Ψ_i^\pm , as given in

$$\begin{aligned}I^\pm &= |\Psi_{SM}^\pm|^2 = |\Psi_{E_0}|^2 \\ &\quad + 2 \sum_i \Re(\Psi_{E_0}^* \Psi_i^\pm) + \mathcal{O}(\alpha_i^2),\end{aligned}\tag{4.9}$$

for $i = I, II, R, I+II$. The intensity of the O -beam behind the interferometer is given by

$$\begin{aligned}
I_{O-Det}^{\pm} = & \frac{1}{32} \left[3 + 2 \cos(\chi_I - \chi_{II}) + 2 \cos(\chi_I - \chi_R) + 2 \cos(\chi_{II} - \chi_R) \right. \\
& \mp 2 \sin(\alpha/2) \left[\cos(\Delta\omega_{It}) [1 + \cos(\chi_I - \chi_{II}) + \cos(\chi_I - \chi_R)] \right. \\
& + \sin(\Delta\omega_{It}) [\sin(\chi_I - \chi_{II}) + \sin(\chi_I - \chi_R)] \\
& + \cos(\Delta\omega_{II}t) [1 + \cos(\chi_{II} - \chi_I) + \cos(\chi_{II} - \chi_R)] \\
& + \sin(\Delta\omega_{II}t) [\sin(\chi_{II} - \chi_I) + \sin(\chi_{II} - \chi_R)] \\
& + \cos(\Delta\omega_{R}t) [1 + \cos(\chi_R - \chi_I) + \cos(\chi_R - \chi_{II})] \\
& + \sin(\Delta\omega_{R}t) [\sin(\chi_R - \chi_I) + \sin(\chi_R - \chi_{II})] \\
& + \cos(\Delta\omega_{I+II}t) [2 + 2 \cos(\chi_I - \chi_{II}) + \cos(\chi_I - \chi_R) + \cos(\chi_{II} - \chi_R)] \\
& \left. \left. + \sin(\Delta\omega_{I+II}t) [2 \sin(\chi_I - \chi_{II}) + \sin(\chi_I - \chi_R) + \sin(\chi_{II} - \chi_R)] \right] \right. \\
& \left. + \mathcal{O}(\alpha_i^2) \right].
\end{aligned} \tag{4.10}$$

It should be noticed, that the first line of Eq.4.10 is equal to the intensity of the unmarked double-loop interferometer in Eq.4.3, besides a scaling factor, that accounts for the intensity lost by the energy compensation. This results in an intensity, for the phases set to $\chi_I = \chi_{II} = \chi_R = 0$ and $\alpha_i = \alpha$,

$$\begin{aligned}
I^{\pm}(\chi_I = \chi_{II} = \chi_R = 0) = & \\
\frac{1}{32} \left[9 \mp 6 \sin\left(\frac{\alpha}{2}\right) \left[\cos(\Delta\omega_{It}) + \cos(\Delta\omega_{II}t) + \cos(\Delta\omega_{R}t) + 2 \cos(\Delta\omega_{I+II}t) \right] \right]. & \\
\end{aligned} \tag{4.11}$$

This setting provides highest possible intensity of the beam in path $I + II$, and therefore highest possible intensity at the O -detector. The intensity at

the O-detector for the phases $\chi_{II} = \pi$ and $\chi_I = \chi_R = 0$ is given by

$$I^\pm(\chi_I = \chi_R = 0, \chi_{II} = \pi) = \frac{1}{32} \left[1 \mp 2 \sin\left(\frac{\alpha}{2}\right) [\cos(\Delta\omega_{It}) - \cos(\Delta\omega_{II}t) + \cos(\Delta\omega_{Rt})] \right]. \quad (4.12)$$

This setting gives lowest possible intensity in the beam in path $I + II$. In an ideal case no intensity would be measured, if a detector is put in the beam in path $I + II$. By tuning the phase of the front-loop to $\chi_I = 0$, and $\chi_{II} = \pi$ the intensity at the O-detector drops to $1/9$ of the intensity when the phase of the front-loop is set to $\chi_I = \chi_{II} = 0$. At the same time the intensity of the signal of WWM_I , WWM_{II} , and WWM_R drops to $1/3$, while the signal from WWM_{I+II} vanishes. This is easily understood by considering the fact that $1/9$ of the amplitude corresponds to $1/\sqrt{9} = 1/3$ intensity. The amplitudes of the wave functions in path I and path II cancel out, due to the phase shift of $\chi_{II} = \pi$.

In the experiment absorbers can be put in positions AB_R , and AB_{I+II} , as depicted in Fig.4.2. By putting absorbers in the beam paths the interference effect of the reference beam R on the outgoing beam $I + II$ of the front loop can be tuned and vice versa. The transmission of the absorbers (T_{AB_R} , $t_{AB_{I+II}}$) is dealt with by multiplying each wave function by the square root of the transmissivity T_i of the respective absorber

$$\Psi'_{I+II} \approx \sqrt{T_{AB_{I+II}}} e^{i\chi_{I+II}} [s_{z+} - \sum_{i=I,II,I+II} ie^{-i\omega_i t} \sin(\alpha_i/2) s_{z-}] \otimes \psi_{I+II} \quad (4.13)$$

$$\Psi'_R \approx \sqrt{T_{AB_R}} e^{i\chi_R} [s_{z+} - ie^{-i\omega_R t} \sin(\alpha_R/2) s_{z-}] \otimes \psi_R. \quad (4.14)$$

The intensity I_{AB}^\pm incorporating the absorbers calculates accordingly to the

intensity without the absorbers Eq.4.10. The intensity is given by

$$\begin{aligned}
I_{AB}^{\pm}(\chi_I = \chi_R = 0, \chi_{II} = \pi) = & \\
= \frac{1}{32} [& T_{AB_R} - 2\sqrt{t_{AB_R} T_{AB_{I+II}}} \sin\left(\frac{\alpha}{2}\right) \cos(\Delta\omega_{I}t) \\
+ 2\sqrt{ & T_{AB_R} T_{AB_{I+II}}} \sin\left(\frac{\alpha}{2}\right) \cos(\Delta\omega_{II}t) - 2T_{AB_R} \sin\left(\frac{\alpha}{2}\right) \cos(\Delta\omega_{R}t)], & \quad (4.15)
\end{aligned}$$

for the phases set to $\chi_I = \chi_R = 0$, and $\chi_{II} = \pi$, which is the only phase setting used in the experiment when absorbers are inserted. When no absorber is put in position AB_R and beam stopper with zero transitivity $T = 0$ is put in position AB_{I+II} , only the signal of WWM_R and the offset from the beam in path R remains.

$$I_{AB}^{\pm}(t_{AB_R} = 1, t_{AB_{I+II}} = 0) = \frac{1}{32} - \frac{1}{16} \sin\left(\frac{\alpha}{2}\right) \cos(\Delta\omega_{II}t) \quad (4.16)$$

This is the intensity at the O-detector coming from the beam in path R and interference between Ψ_R and Ψ'_R . When a beam stopper is put in AB_R and no absorber is put in AB_{I+II} , no signal arrives at the O-detector. The signal of the beams in path I and II vanishes, as well as the blocked beam in path R . This is understood by the fact, that no intensity arrives at the O-detector.

When the marking strength is increased by increasing the angle α_i terms of the order α^2 can no longer be neglected, which makes the calculation much more complicated, since the terms such as

$$\sum_i \sum_j \Re(\Psi_i^{\pm*} \Psi_j^{\pm}) \quad (4.17)$$

should be taken into account. In the extreme case of complete entanglement of path and energy shift, given at $\alpha_i = \pi$, the phase shifters no longer shift intensity from one detector to the other, but only add a phase to the time depending intensity modulations. Without a time resolved measurement the intensity at the O-detector would be constant, which is not the case for

which way marking of $\alpha < \pi$. This is analogous to Englerts duality relation $D^2 + V^2 \leq 1$ [Englert, 1996], but in this case the visibility is proportional to $\cos(\alpha/2)$, and distinguishability is proportional to $\sin(\alpha/2)$, which results in

$$\cos(\alpha/2)^2 + \sin(\alpha/2)^2 \leq 1. \quad (4.18)$$

This relation limits the amount of which-way information can be extracted, while preserving a certain amount of visibility of the interference fringes.

4.3 Simulation

Due to imperfections in the setup and the interferometer, the interference visibility is reduced. To be able to compare theoretical predictions with the experimental results, the effect of the reduction in contrast needs to be accounted for in a simulation. Deviations from the ideal theoretical predictions are caused for example by external perturbations, reduced degree of spin polarization, efficiency of the spin manipulators and analyzer, misalignment of the setup, and the contrast of the interferometer itself.

In case of the present experiment using a four plate double-loop interferometer, the contrast of the interferometer has the largest influence. Since the simulation is an approximation and the other influences listed above are considered to be small, in comparison with the effect of the contrast of the interferograms, they are not taken into account.

First we consider a single loop interferometer with two path wave functions ψ_I and ψ_{II} and try to give a simple description of reduced degree of interference ability, by a contrast parameter $0 \leq C_{i,j} \leq 1$. The wave functions are given by

$$\psi_I = \frac{1}{2\sqrt{2}}e^{ix_I}, \quad \text{and} \quad \psi_{II} = \frac{1}{2\sqrt{2}}e^{ix_{II}}. \quad (4.19)$$

The intensity of the outgoing beam towards the O-detector can now be writ-

ten as

$$I_O(C_{i,j}) = \sum_{i=I,II} \sum_{j=I,II} C_{i,j} (\psi_i^* \psi_j) = \frac{1}{4} (1 + C_{I,II} \cos(\chi_I - \chi_{II})). \quad (4.20)$$

By tuning $C_{i,j}$ between 0 and 1 any contrast occurring in an experiment can be simulated. For the double loop interferometer a set of three wave functions are present,

$$\psi_I = \frac{1}{4} e^{i\chi_I}, \quad \psi_{II} = \frac{1}{4} e^{i\chi_{II}}, \quad \text{and} \quad \psi_R = \frac{1}{4} e^{i\chi_R}. \quad (4.21)$$

The contrast of each pair of wave functions need to be taken into account

$$\begin{aligned} C_{i,j} \Big|_{i \neq j} &= \{C_{I,II} = C_{II,I}, C_{I,R} = C_{R,I}, C_{II,R} = C_{R,II}\} \\ C_{I,I} &= C_{II,II} = C_{R,R} = 1. \end{aligned} \quad (4.22)$$

The intensity at the O-detector is given by

$$\begin{aligned} I_O(C_{i,j}) &= \sum_{i=I,II,R} \sum_{j=I,II,R} C_{i,j} (\psi_i^* \psi_j) \\ &= \frac{1}{3} \left[1 + \frac{2}{3} (C_{I,II} \cos(\chi_I - \chi_{II}) + C_{I,R} \cos(\chi_I - \chi_R) \right. \\ &\quad \left. + C_{II,R} \cos(\chi_{II} - \chi_R)) \right]. \end{aligned} \quad (4.23)$$

At the first glance this relation allows for negative intensities for example when the parameters $\chi_I = \chi_R = 0$, $\chi_{II} = \pi$, $C_{I,II} = C_{I,R} = 1$, and $C_{II,R} = 0$ are chosen, which results in

$$I_O(C_{i,j}) = -\frac{1}{9}. \quad (4.24)$$

But this is not a possible set of parameter achievable in reality, since the contrast parameters $C_{i,j}$ are composed in practice as products of the coherent amplitudes of each wave function A_i^{coh} corresponding to the contrast

parameter, as given in

$$A_I^{coh} A_{II}^{coh} = C_{I,II} \quad (4.25)$$

$$A_I^{coh} A_R^{coh} = C_{I,R} \quad (4.26)$$

$$A_{II}^{coh} A_R^{coh} = C_{II,R}. \quad (4.27)$$

This natural restriction is sufficient to avoid negative intensities at the O-detector. Therefore the equation Eq.4.23 is valid for a double loop interferometer with reduced contrast. Furthermore since contrast of each pair of wave functions is experimentally accessible, the values of $C_{i,j}$ can be measured separately.

When the experiment is simulated including the spin dependent part of the wave functions, the intensity at the O-detector can be calculated in a similar manner as in equation Eq.4.9.

$$I_{c.c.}^{\pm} = \sum_i \sum_j C_{i,j} (\Psi_i^* \Psi_j) + \sum_i \sum_j \Re(C_{i,j} \Psi_i^* \Psi_j^{\pm}) + \mathcal{O}(\alpha_i^2). \quad (4.28)$$

This result in an contrast corrected intensity of

$$\begin{aligned}
I_{c.c.}^{\pm} = & \\
& \frac{1}{32} \left[3 + 2C_{I,II} \cos(\chi_I - \chi_{II}) + 2C_{I,R} \cos(\chi_I - \chi_R) + 2C_{II,R} \cos(\chi_{II} - \chi_R) \right. \\
& \mp 2 \sin(\alpha/2) \\
& \left[\cos(\Delta\omega_{It}) [1 + C_{I,II} \cos(\chi_I - \chi_{II}) + C_{I,R} \cos(\chi_I - \chi_R)] \right. \\
& + \sin(\Delta\omega_{It}) [C_{I,II} \sin(\chi_I - \chi_{II}) + C_{I,R} \sin(\chi_I - \chi_R)] \\
& + \cos(\Delta\omega_{II}t) [1 + C_{I,II} \cos(\chi_{II} - \chi_I) + C_{II,R} \cos(\chi_{II} - \chi_R)] \\
& + \sin(\Delta\omega_{II}t) [C_{I,II} \sin(\chi_{II} - \chi_I) + C_{II,R} \sin(\chi_{II} - \chi_R)] \\
& + \cos(\Delta\omega_{Rt}) [1 + C_{R,I} \cos(\chi_R - \chi_I) + C_{R,II} \cos(\chi_R - \chi_{II})] \\
& + \sin(\Delta\omega_{Rt}) [C_{R,I} \sin(\chi_R - \chi_I) + C_{R,II} \sin(\chi_R - \chi_{II})] \\
& + \cos(\Delta\omega_{I+II}t) \\
& \left. \left[2 + 2C_{I,II} \cos(\chi_I - \chi_{II}) + C_{I,R} \cos(\chi_I - \chi_R) + C_{II,R} \cos(\chi_{II} - \chi_R) \right] \right. \\
& + \sin(\Delta\omega_{I+II}t) \\
& \left. \left[2C_{I,II} \sin(\chi_I - \chi_{II}) + C_{I,R} \sin(\chi_I - \chi_R) + \sin(C_{II,R}\chi_{II} - \chi_R) \right] \right] \\
& + \mathcal{O}(\alpha_i^2) \left. \right].
\end{aligned} \tag{4.29}$$

4.4 Preparations for the experiment

The present which-way measurement requires an interferometer that provides three spatially separated interfering beams, and time resolved measurement at the three detectors. Since there was no suitable interferometer, a new double-loop interferometer is designed and fabricated. For the time resolved-measurement a new FPGA-card (field programmable gate array) is installed in the computer system at the S18 facility, new software is written and im-

plemented in the existing control system of the S18 facility.

4.4.1 The new double-loop interferometer

To satisfy all requirements of the experiment a new interferometer must be built to very specific needs. A interferometer is needed in which three different beam paths interfere with each other. The distance between the plates must be as big as possible to have as much space as possible in the interferometer for spin manipulation devices. However, the design is limited by the size of the silicon crystal rod and by technical restraints.

Design of the new double-loop neutron interferometer

When four plates are placed one after another, eight outgoing beams are present behind the fourth plate as seen in Fig.4.4. Four of this outgoing beams i.e. A , B , G , and H , can only be reached by one path the neutrons can take, therefore they show no interference between three paths. The other four outgoing beams can be reached by three paths each, the neutron can take. However, only path C can show a contrast of $C = 1$ in each of the three possible loops. This is due to Pendellösung effects, which are described in section 2.2.1. Only beams which are reflected and transmitted the same amount of times show full overlap and therefore full interference. There are three paths for the neutrons ending up in beam $C = ttrr + trrt + rrtt$. The new double loop interferometer is designed in a way that beam C is used for measurements. The plates need to be equally distanced and equally thick, in order to enable full contrast in the experiment.

The interferometer is cut out of a silicon perfect crystal rod with 4 inch diameter. The 220-plane is chosen as reflection plane, which allows to use neutrons with a wavelength of 1.92 Å at a Bragg-angle of 30° and a symmetric beam design. The thermal neutron guide H25 used at the S18 instrument at the ILL provides highest neutron intensity at 1.92 Å, and therefore the

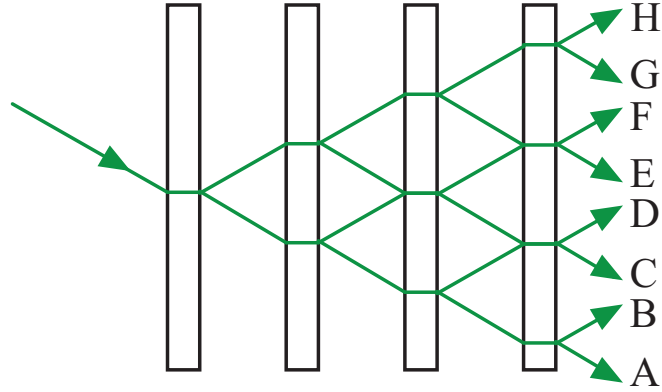


Figure 4.4: A four plate interferometer with all possible outgoing beams (A-H) depicted.

highest possible count rate. Since the coherence length of the neutrons is about $10\ \mu\text{m}$ for the transversal direction of the beam trajectory, between the plates should be within one order of magnitude below the coherence length i.e. $1\ \mu\text{m}$. This very high precision is feasible for the manufacturing process.

Each plate should be as thin as possible to allow for more space for spin manipulation devices, as well as to avoid too much widening of the beam, since the beam gets widened by the plate thickness while passing it. If the plates are too thin they will bend during the cutting process and therefore reduce the achievable precision. After consulting with the company Holm-Silicon [Holm, 2013], which actually did the cutting, a plate thickness of 2.5 mm was chosen. The design of the interferometer is depicted in Fig.4.5,4.6, with length specification in millimeters.

The distance between the plates is limited by the width of the crystal. The incoming beam gets wider at every plate of the interferometer by the thickness of the plate, as described in section 2.2.1. Since the interferometer has four plates with a thickness of 2.5 mm the beam widens by 10 mm by

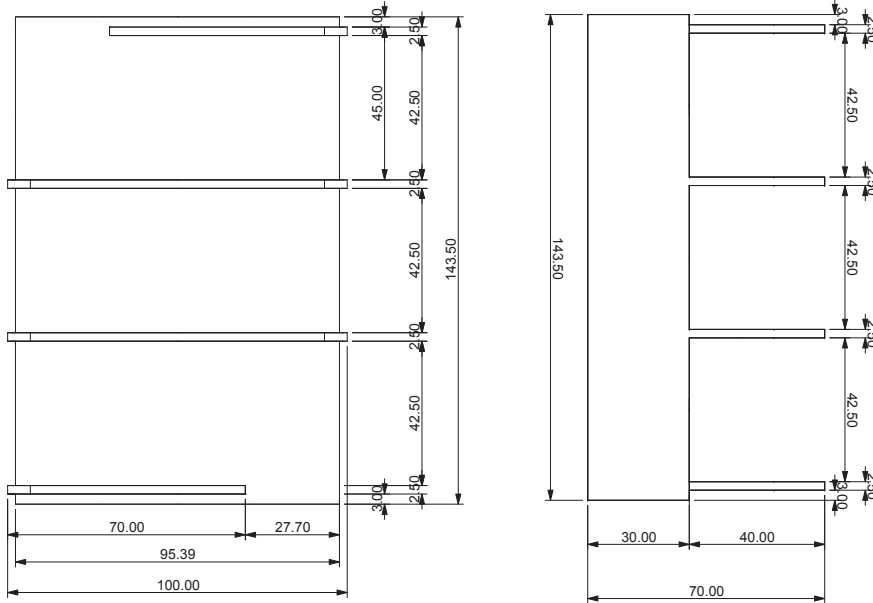


Figure 4.5: CAD planes of the new double loop interferometer, with length specification in mm. Left: Top-view of the interferometer. Right: Side-view of the interferometer.

passing through the interferometer. Due to the Bragg-angle of $\theta_B = 30^\circ$, resulting in an angle between transmitted and reflected beam of 60° , the beam separation is as wide as the plate distance. The distance between the interferometer plates is chosen to be 42.5 mm, as depicted in figure Fig.4.5. This results in a separation between furthest left and furthest right position of the beam of 64 mm. By adding the initial beam width of about 5 mm and the beam widening of 10 mm, a rough estimate of the width needed by the neutron beam is given at 79 mm. At the broadest point of the interferometer of 100 mm, this allows for lateral adjustment of the beam within a range of 21 mm.

The beam path in the interferometer is depicted in 3D in Fig.4.7. Two phase shifter plates (PS_{II} , PS_R) are sufficient to tune any relative phases for the three beams. There are three outgoing beams, which are used in

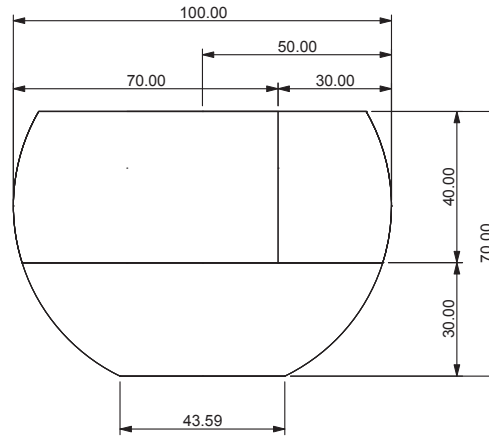


Figure 4.6: *Side-view of the CAD plan for new double-loop interferometer, with length specification in mm.*

experiments, labeled H1, H2, and O. By monitoring two of the three beams the phase relations of all three paths can be monitored, i.e. H1 and H2. The third beam can be used for additional analysis like spin state and time resolution.

Principles of silicon etching

The cutting process produces micro cracks on the surface of the interferometer, that need to be removed before the interferometer can be put to use. This is achieved by chemical etching of $30\ \mu\text{m}$ in depth from the surface of the whole interferometer. The etch bath consist of nitric acid HNO_3 60% and hydrofluoric acid HF 40%. The reaction takes place in several steps: First the nitric acid is converted to nitrogen dioxide and water. Then silicon dioxide builds up on the surface of the crystal. The silicon oxide is then

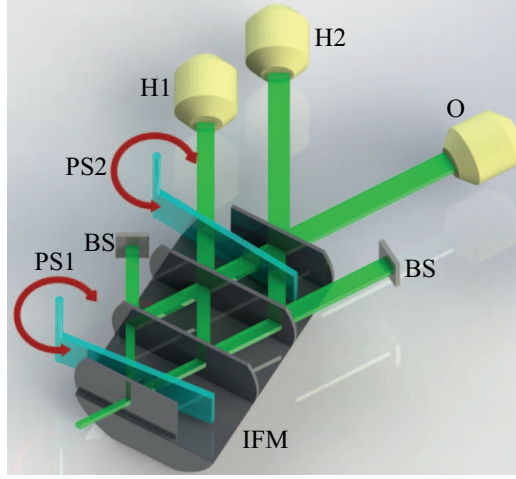
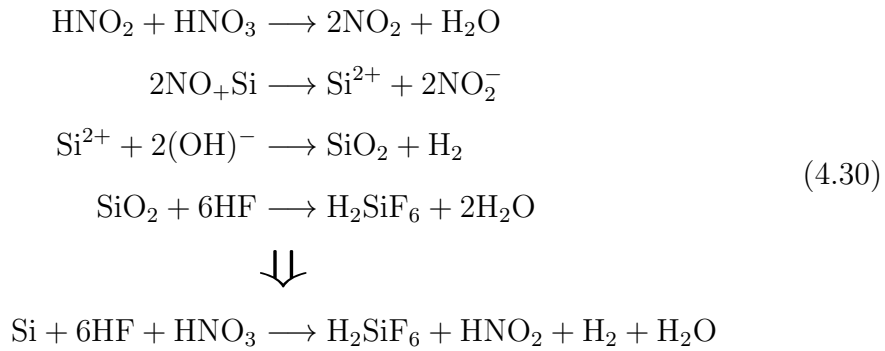


Figure 4.7: Interferometer (IFM) with two phase shifters (PS_{II} , PS_R) inserted. Two beam stoppers (BS) block non-interfering beams, not used for measurement. Three detectors (O, H1, H2) detect beams which can show interference.

removed by the hydrofluoric acid. This whole process can be written as



The etching bath is a mixture of 60 parts nitric acid and 1 part hydrofluoric acid. The mixing ratio determines the etching rate, the more hydrofluoric acid is added the faster the etching rate. The expected etching rate using a 60 : 1 mixture is $0.3 \mu\text{m}/\text{min}$ [Zawisky et al., 2009], which can vary depending on temperature and roughness of the surface of the interferometer. It is important to etch slowly to get homogeneous etching on the whole surface of

the interferometer. When etching fast the interferometer heats up, especially the plates and the edges, the higher the temperature the faster the etching process. Also when etching fast the exchange of exhausted acid and fresh acid is in-homogeneous over the surfaces of the interferometer. Both effects result in a higher etching rate at edges, which results in a cushion like shape of the plates, referred to as '*cushion effect*'. Which results in defocusing of the neutron beam and therefore a reduction in contrast. Both effects are inevitable, but can be reduced by slow etching and constant temperature of the etching bath. When an etching depth of about $100\ \mu\text{m}$ is reached the cushion effect has built up to an amount that is already reducing the contrast of the interferometer, etching any further should be avoided.

When the etching rate is too high, gas bubbles appear on the surface of the crystal. These bubbles cause an in-homogeneous etching result. By moving the interferometer in the etching bath, the bubbles can be removed.

During the etching process the hydrofluoric acid is degraded and needs to be replaced at a rate of 20 ml per gram of silicon removed from the interferometer. How much mass of silicon is removed during the etching process can be calculated using $\Delta m_{Si} = A\rho_{Si}\Delta d$, where A is the surface of the interferometer, $\rho_{Si} = 2.363\ \text{kg/m}^3$ is the density of silicon, and Δd is the expected etching depth. By weighing the interferometer before and after the etching, it is possible to calculate the actual etching depth using the formula above.

Interferometer etching process

Prior to the etching process the interferometer has to be cleaned to remove any residue of the cutting process, which would have an adverse effect on the etching. First the interferometer is put in a lean solution of the detergent *Dextran neutral*[®] in deionized water for several hours, to dissolve residue. The interferometer is then wiped with dust free laboratory wipes to remove residue. This is done until no more residue is visible on the laboratory wipes.

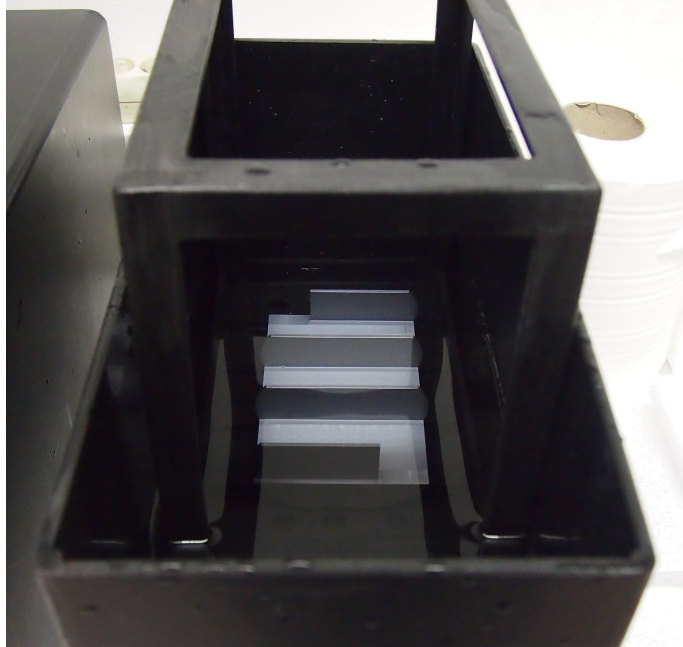


Figure 4.8: *Interferometer in an acetone bath before the etching process.*

The interferometer is rinsed with deionized water before it is put in a bath of p.a. (pro analysis) acetone for several hours, to dissolve any remaining fouling. In Fig.4.8 the interferometer is shown in the acetone bath. The interferometer is wiped again with laboratory wipes and acetone. To avoid dust to set on the interferometer it is placed in the acetone bath until the etching process.

The etching depth is estimated by weighing the interferometer before and after the etching process. Since the interferometer weighs about 860 g and the expected weight loss is expected to be about 5 g the weighing has to be highly accurate. The scale used is a Sartorio PT-300 with a precision of 0.001 g at a weight of 1000 g. The interferometer is taken out of the acetone bath dried using compressed nitrogen gas to get rid of any excess acetone as seen in Fig.4.9 and put on the scale Fig.4.9. Since the evaporation of the acetone cools the interferometer moisture in the air condensates on the

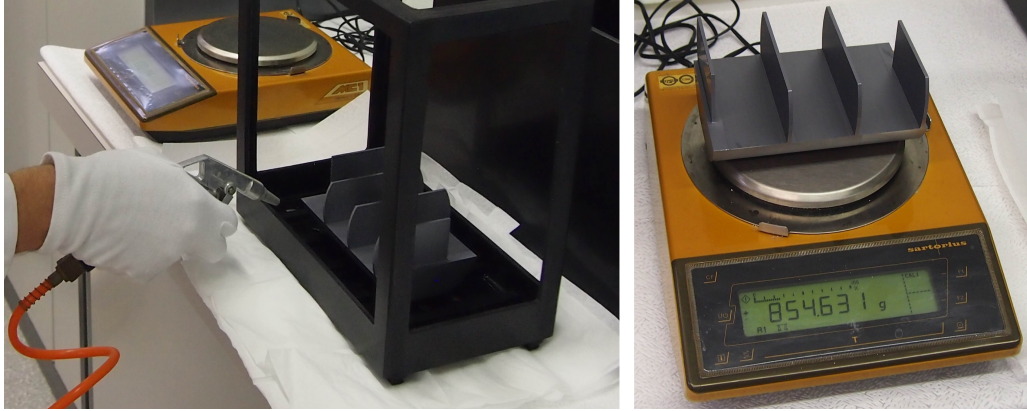


Figure 4.9: *Weighing of the interferometer. Left: Air-drying of the interferometer. Right: Interferometer on a high precision scale.*

interferometer and therefore alter the weighing result. To get better weighing results an average over three weighings is calculated. For the etching process the etching bath is put in a water bath, which acts as a temperature reservoir to keep the etching bath at a stable temperature as seen in Fig.4.10 . When the interferometer is put into the etching bath bubbles can form on the surface of the silicon crystal, which can degrade the quality of the etching process. By moving the interferometer in the bath this bubbles can be removed. During the etching hydrofluoric acid is dissipated and needs to be replaced. After the estimated etching time, the interferometer is put into a bath of deionized water to wash out the acids of the etching bath.

For the first etching an etching rate of $0.3 \mu\text{m}/\text{min}$ was expected, therefore a etching time of 60 min was calculated for an etching depth of $18 \mu\text{m}$, which is set lower than the $30 \mu\text{m}$ expected for the interferometer to work, to avoid too deep etching. Given the calculated surface of the interferometer of 633.5 cm^2 , a mass loss of 2.7 g of silicon was expected, which results in a consumption of 54 ml of hydrofluoric acid during the etching process. This consumption needs to be compensated by adding hydrofluoric acid during the etching. The hydrofluoric acid is added in 18 ml portions at 15 min, 30 min,

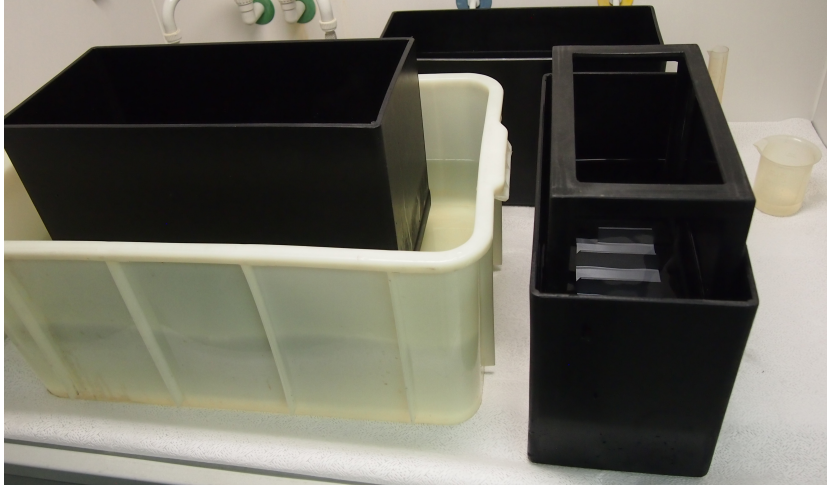


Figure 4.10: *The etching bath in a temperature reservoir ready for etching.*

and 45 min. The interferometer weighed before etching, and has a mass of 854.67 g. During the etching no bubbles appeared on the surface of the interferometer, which is an indication for slow and homogeneous etching. The interferometer is moved in the bath at least every 3 min to mix the etching bath and to get acid exchange on the surface of the interferometer.

After 60 min of etching the interferometer is put in deionized water to get rid of any excess acid and the etching bath is disposed. For weighing the interferometer is put in an acetone bath, taken out, air dried and weighed in the same manner as before the etching. The weight of the interferometer after etching is 852.83 g, which gives a mass loss 1.83 g, therefore an etching depth of $\Delta d = 12.2 \mu\text{m}$, and an etching rate of $0.2 \mu\text{m}/\text{min}$. The etching rate is much lower than expected, which is caused by the very flat surface provided by the company Holm-Silicon.

The goal for the second etching is to reach an overall etching depth of $30 \mu\text{m}$. Since the first etching reached $12.2 \mu\text{m}$, only $17.8 \mu\text{m}$ need to be removed now. By the etching rate of $0.2 \mu\text{m}/\text{min}$ an etching time of 89 min is calculated as well as 2.7 g of mass loss and 53 ml of hydrofluoric acid con-

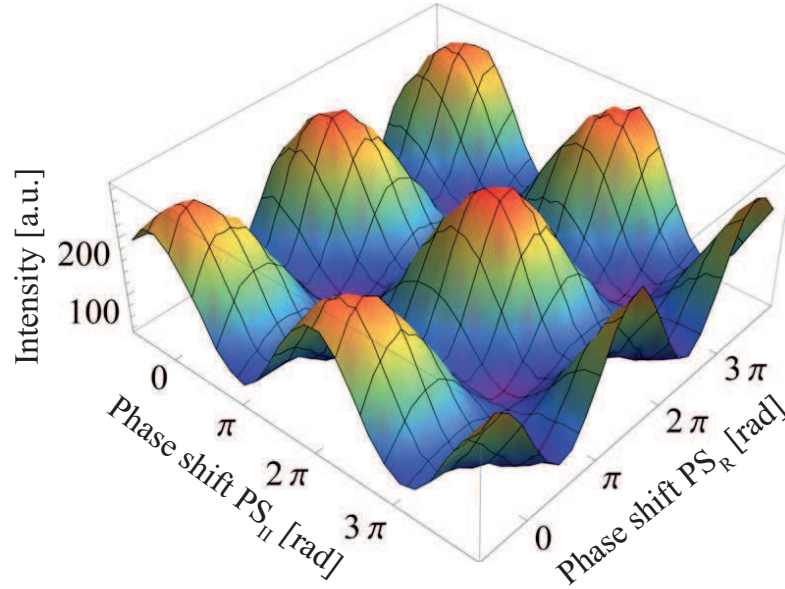


Figure 4.11: *Interference pattern for two phase shifters in the interferometer.*

sumption. The hydrofluoric acid is added in 18 ml portions after 22 min, 44 min, and 66 min.

After the second etching the interferometer weight 849.72g, which gives an etching depth of $20.8 \mu\text{m}$ and an average etching rate of $0.23 \mu\text{m}/\text{min}$. The interferometer is now etched by $33.0 \mu\text{m}$ overall, slightly more than expected. The interferometer is tested at the S18 at the ILL Grenoble, but no interference fringes are found. This makes a third etching necessary.

The goal for the third etching process is to etch $15 \mu\text{m}$ more. For the etching the previously obtained average etching rate of $0.22 \mu\text{m}/\text{min}$ is used for calculations. This results in an etching time of 68 min, a weight loss of 2.25 g and a hydrofluoric acid consumption of 45 ml. The hydrofluoric acid is added in 15 ml portions after 17 min, 34 min, and 51 min.

After the third etching the interferometer weight 847.67g, which gives an etching depth of $13.7 \mu\text{m}$ at an etching rate of $0.2 \mu\text{m}/\text{min}$. The interferom-

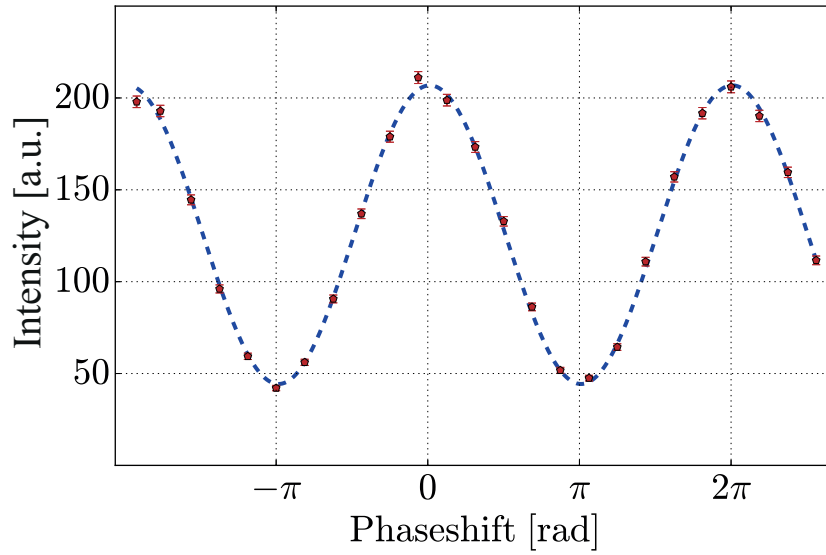


Figure 4.12: *Interference pattern with one phase shifter fixed at a position with maximum contrast for the second phase shifter.*

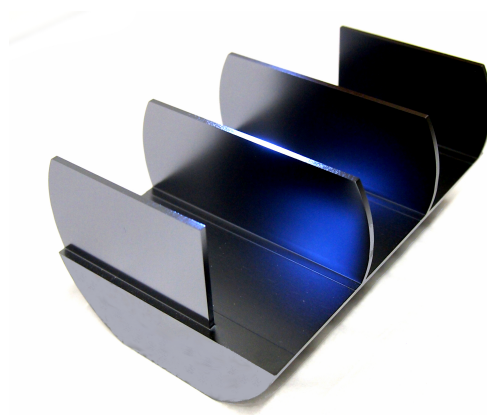


Figure 4.13: *Photography of the double-loop interferometer after the completed etching process.*

eter is tested in Grenoble and showed a contrast of about 65%. Two test are made both with two phaseshifters in the interferometer as depicted in Fig.4.7. In Fig. 4.11 an interference pattern for an array of positions for phase shifter PS_I and phase shifter PS_R is depicted. Depending on the position of one phaseshifter the contrast achieved by tuning the other varies. In figure Fig.4.12 phase shifter PS_I is set to give a phase shift of 0 rad and a phase shifter scan using phase shifter PS_R is performed. The contrast of this scan is 0.647(5). A photography of the finished double-loop interferometer is depicted in Fig.4.13.

4.4.2 Time-resolved measurement

To obtain information of the which-way marking a time-resolved measurement of the detector signal needs to be performed. This is achieved via a FPGA card (field programmable gate array) and new software for the FPGA card, as well as software, integrated in the slow control system (i.e. the user interface) of the S18 instrument. The time resolution program is programmed using LAB-View[®]. Beside the time resolution of the detector signal the FPGA card also creates a trigger signal for the spin manipulators and the data acquisition to ensure a synchronized processes. A schematic of the time resolution system is given in Fig.4.14

The time resolved measurement is performed in a way that the slow control system gives parameters to the FPGA card i.e. loop time, delay time of the trigger signal, duration of the trigger signal, duration of the measurement, start signal, and stop signal. When the measurement is started by sending the start signal to the FPGA card, the FPGA card starts loops with given duration, every time a neutron is detected by one of the detectors the FPGA card creates an entry in a FIFO data buffer (first in first out) containing a detector identifier and the time of measurement of the neutron since the start of the last loop. This buffer is read out by the slow control

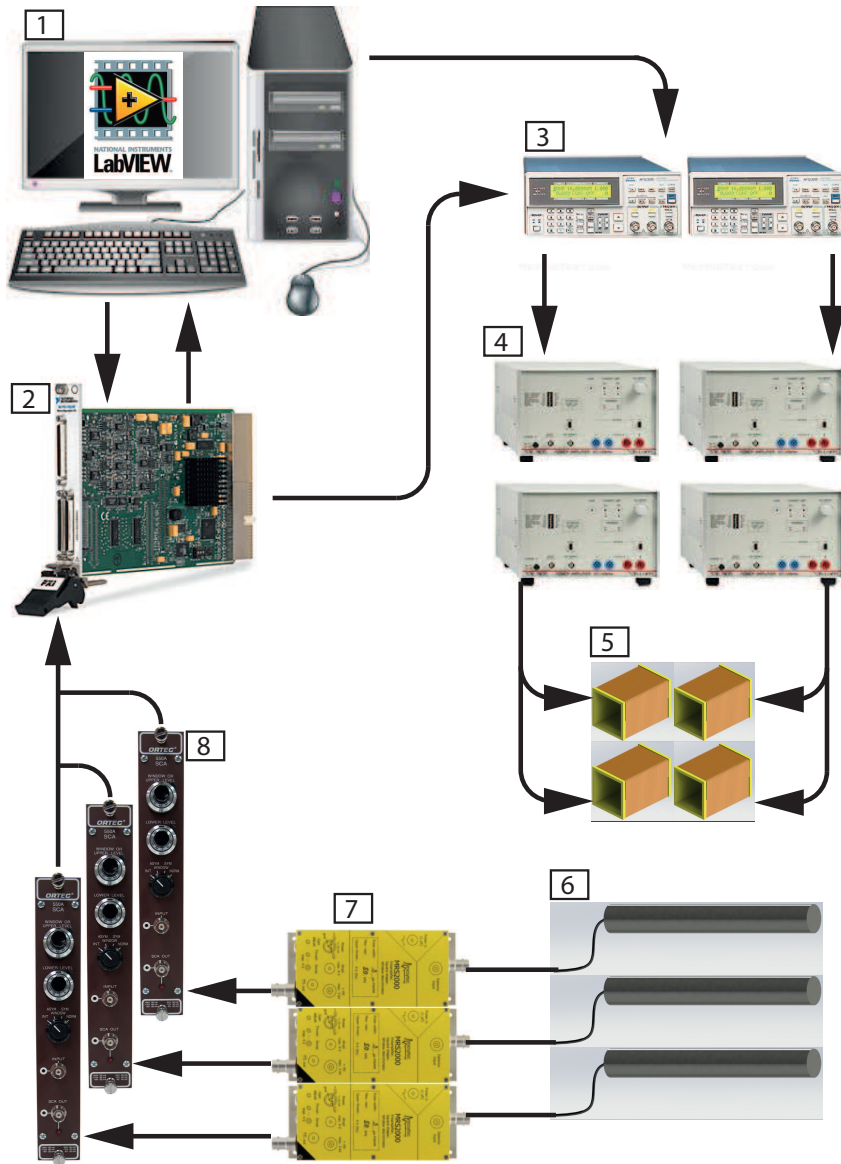


Figure 4.14: The setup for time resolved measurements, consisting of (1) the slow control system, (2) FPGA card, (3) function generators, (4) signal amplifiers, (5) resonance-frequency spin-rotators, (6) detectors, (7) pre-amplifier, and (8) single channel analyzer.

system. In each loop a trigger signal is produced by the FPGA card starting after the delay time is reached, and lasting as long as the given duration of the trigger signal. The delay is to compensate for the time of flight of the neutrons between the spin manipulators and the detector. The delay can be calculated by subtracting the time of flight from the loop time. The trigger signal is sent to the function generators, which produce sinusoidal output signals of given frequency and amplitude. The signal is forwarded to amplifiers, which in turn power the spin manipulators. When the function generators are triggered, they start producing a burst of sine waves for the duration of one loop with certain parameters (i.e. frequency, amplitude, offset), given by the slow control system. The parameters for the signal generators are set before the FPGA card is activated. The FPGA card operates continuously until the duration of the measurement is reached, or a stop signal is sent from the slow control system.

The slow control system dequeues the buffer, and sorts the counts into bins according to the time the neutrons were measured after start of the loop. The slow control system creates two files, one with the accumulated counts in each bin, and one with detection time of every single neutron. The latter can be used for investigating correlations in neutron detection.

The FPGA card used is a National Instrument[©] NI PXI-7813R card, with 40 MHz clock frequency which gives a maximal time resolution of 25 ns. The signal coming from each detector is preamplified by a mesytec-MRS-2000[©] preamplifier, and discriminated by ORTEC[©] 590A single channel analyzers (SCA), which passes a TTL signal on to a digital input of the FPGA card. When the signal from the SCA exceeds a threshold, the FPGA card registers one count. The shaping time of the SCA limits the resolution to 500 ns. The signal generators used are Tektronix[©] AFG320, and the signal amplifiers used are Toellner[©] TOE7610.

4.5 Experiment realisation

For the execution of this experiment some components, such as beam polarization, a spin analysis, vibration damping, and long-term temperature stability, are identical to those used in the setup for the measurement of Bell's inequality. However, since the double-loop interferometer provides one more path which need to be adjusted, two instead of one phase shifters, and five instead of four spin manipulation devices are needed, which are more complicated to adjust, the time for adjusting the setup increases by few days.

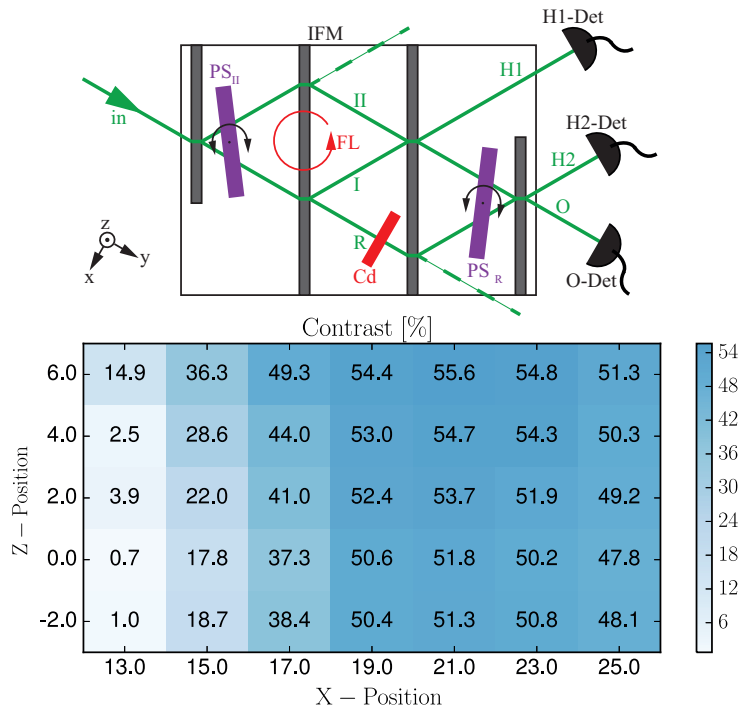


Figure 4.15: Raster scan of the front-loop. Top: The double-loop interferometer with a cadmium absorber (Cd) placed in path R. Only path I and path II are able to show interference fringes, this loop is referred to as the front loop (FL). Bottom: Results of a raster scan of the front loop, where the contrast is plotted against the position of the aperture.

As in the Bell setup, the three-fold monochromator is adjusted first. Then the interferometer is placed in the beam and the rocking angle together with the ρ -axis is adjusted. The double loop interferometer requires two phase shifters. As a phase shifter PS_{II} a 5 mm thick slab of silicon is used. The second phase shifter PS_R is made of 3 mm thick sapphire crystal.

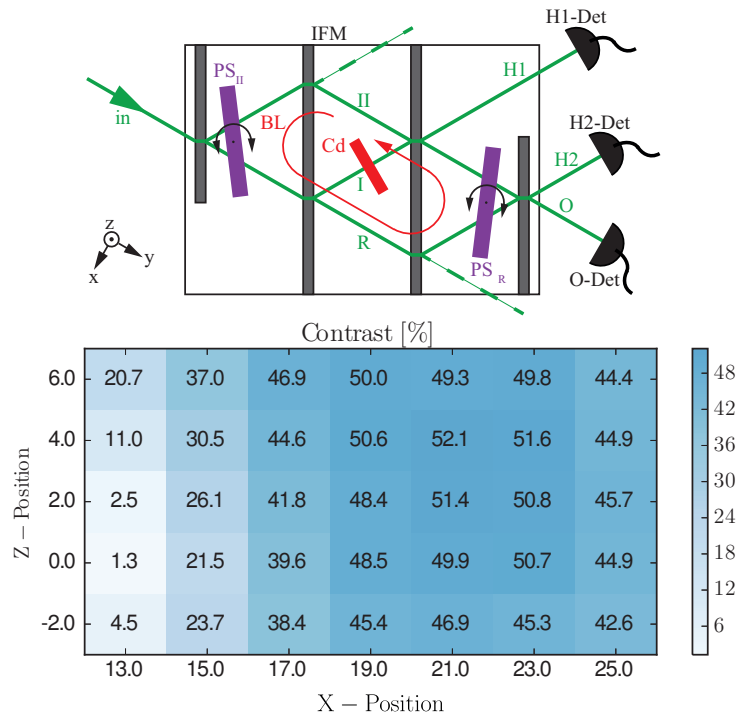


Figure 4.16: Raster scan of the big-loop. Top: The double-loop interferometer with a cadmium absorber (Cd) placed in path I. Only path II and path R are able to show interference fringes, this loop is referred to as the big loop (BL). Results of a raster scan of the big loop, where the contrast is plotted against the position of the aperture.

The double-loop interferometer provides three paths, each pair of paths shows interference fringes, which results in three different loops consisting of two paths interfering with each other. To find the spot where the interferometer provides the highest contrast three raster scans must be performed.

Finally a raster scan of the aft loop is performed, with the Cadmium

beam blocker in path II . This raster scan is performed using phase shifter PS_R . The results of this raster scan are depicted in figure Fig.4.17.

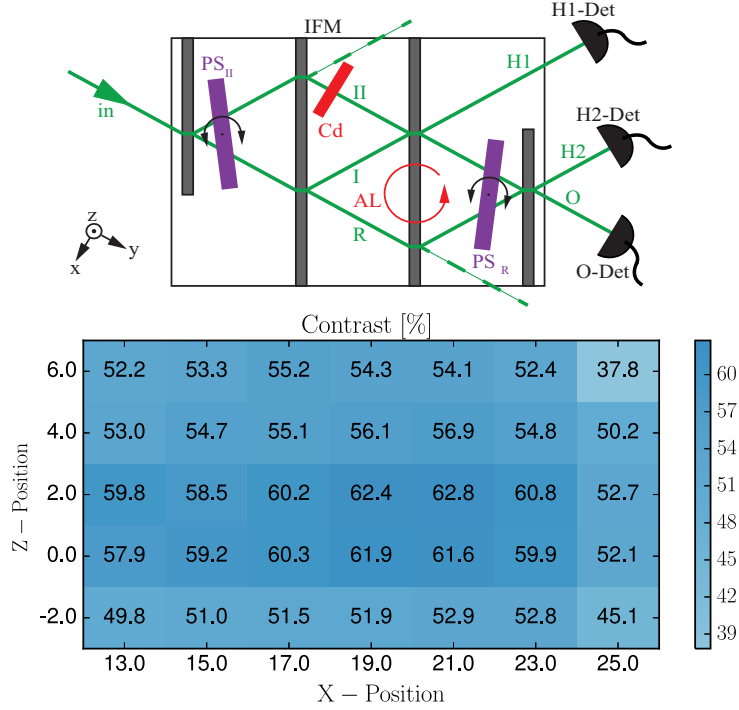


Figure 4.17: Raster scan of the aft-loop. Top: The double-loop interferometer with a cadmium absorber (Cd) placed in path II . Only path I and path R are able to show interference fringes, this loop is referred to as the aft loop (AL). Bottom: Results of a raster scan of the aft loop, where the contrast is plotted against the position of the aperture.

First a scan of the front loop is performed with a Cadmium beam blocker in path R , as plotted in figure Fig.4.15. The aperture in front of the interferometer is moved in 2 mm increments over an area of 12 mm width or Y -direction and 8 mm height in Z -direction, at each position a phase shifter scan using phase shifter PS_{II} is performed. The results of the raster scan are shown in figure Fig.4.15.

In the same manner a raster scan of the big loop is performed with the Cadmium beam blocker placed in beam path I , as depicted in Fig.4.16.

The raster scan is performed in the same area as before using phase shifter PS_{II} again, since this is the phase shifter that is actually altered during the measurement. The results are shown in graph fig.4.16.

For the measurement the position $Y = 21$ mm and $Z = 4$ mm, this position shows good contrast for all three loops. The contrasts at this positions are used for the simulation later on.

Next the guide field is set adjusted. The resonance-frequency spin-rotators will operate at $\omega_I/2\pi = 74$ kHz, $\omega_{II}/2\pi = 77$ kHz, $\omega_{I+II}/2\pi = 80$ kHz, and $\omega_R/2\pi = 71$ kHz respectively. The energy compensating SR_{EC} behind the interferometer is set to the frequency $\omega_{EC}/2\pi = 68$ kHz. The local guide fields adjust the the local guide field to satisfy the resonance condition

$$\omega_{res} = \frac{2|\mu|B_{tot}}{\hbar} \left(1 + \frac{B_{osc}^2}{16B_{tot}^2} \right), \quad (4.31)$$

with $B_{tot} = B_{GF} + B_{loc}$, which is the sum of the guide field and the local guide field. To reduce the fields applied by the local guide fields the guide field is set roughly to the field strength needed for the middle frequency of $\omega_I/2\pi = 74$ kHz. This results to a field strength of about 25 G. In figure Fig.4.18 a CAD drawing is depicted showing the fields applied by the resonance-frequency spin-rotator on the left side, and on the right side a picture of the actual spin-rotator at three different stages of construction is shown.

Interferograms of the front-loop are measured at different cooling-water temperatures of the guide field, as described in section 3.5. The best temperature setting is found at 22.0 °C. Subsequently the spin rotator assembly is put into the interferometer. A picture of the assembly is shown in figure Fig.4.19. Then a temperature versus contrast scan of the cooling water in the spin rotator assembly is performed. The result is depicted in graph Fig.4.20, we found the best temperature at 21.37 °C marked with a dashed green line.

Now the resonance-frequency spin-rotators can be adjusted one at the

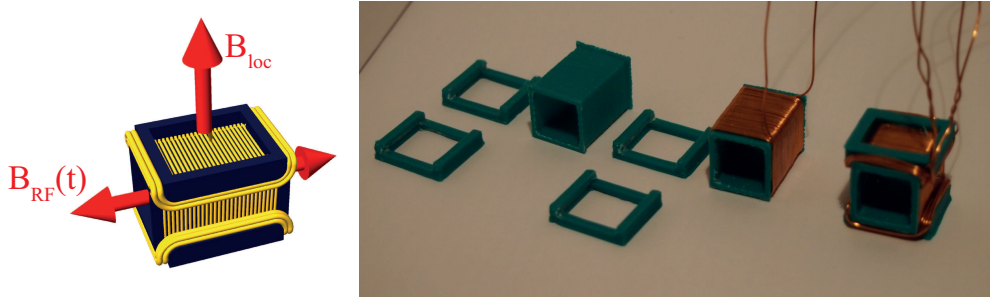


Figure 4.18: *Resonance-frequency spin-rotator. Left: Depiction the two magnetic fields, i.e. the local guide field B_{loc} and the time dependent oscillating field $B_{RF}(t)$ Right: Picture of the resonance-frequency spin-rotator from left to right: 3D printed frames, frame with coil for the oscillating field, finished spin-rotator with local guide field coils.*

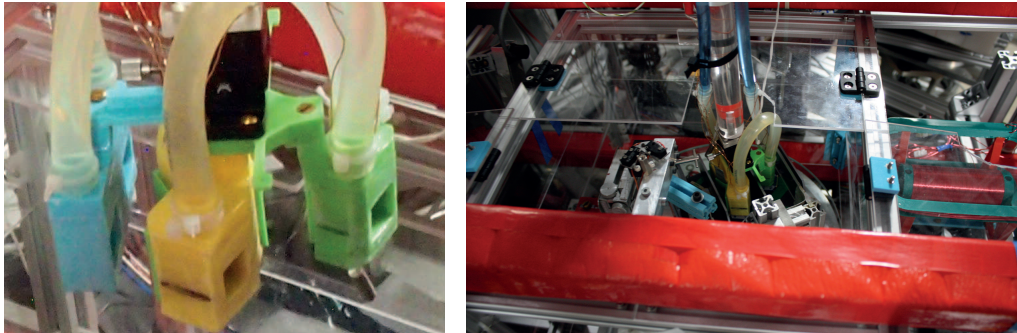


Figure 4.19: *The resonance-frequency spin-rotator assembly. Left: The whole assembly is about 110 mm in length. The black lines on the boxes mark the middle of the passage for the neutron beam, which is aligned using a laser level. Right: The resonance-frequency spin-rotator assembly in the interferometer.*

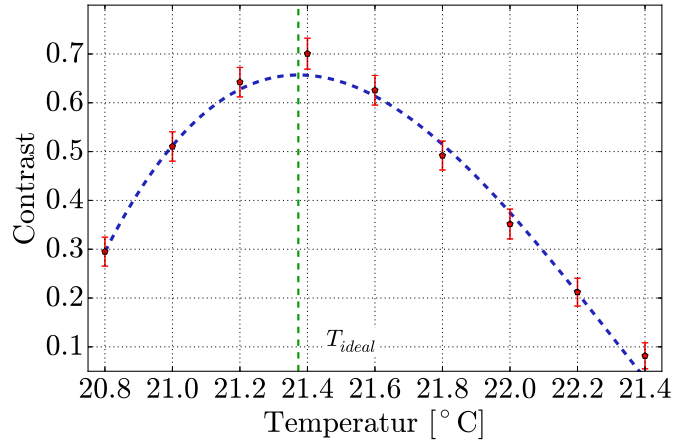


Figure 4.20: *The contrast in dependence on the temperature of the spin rotator assembly. The best temperature is at 21.37°C, which is marked with a green dashed line.*

time and the unused paths are blocked using Cadmium beam blockers. First the spin rotator in path I is adjusted at a frequency of $\omega_I/2\pi = 74$ kHz. A function generator produces a sine curve at the given frequency, the output amplitude i.e. the peak voltage, is adjusted. The signal coming from the function generator is sent to an amplifier, that drives the resonance-frequency spin-rotator. By changing the output amplitude of the function generator the power output of the amplifier to the resonance-frequency spin-rotator is tuned.

First the amplitude of the function generator is set to an estimated 3 V and the count rate versus of current in the coil producing the local guide field is measured. The result of this scan is shown in Fig.4.21. A green dashed line marks the current of $C_{min} = 0.32$ A at which the lowest count rate is achieved, according to a polynomial curve fit. Then a scan of the amplitude of the function generator with the current of the local guide field set to C_{min} . The result is shown in graph Fig.4.21. The wide curve is best fitted using a sine curve. From the fit parameters the amplitude corresponding to a spin-

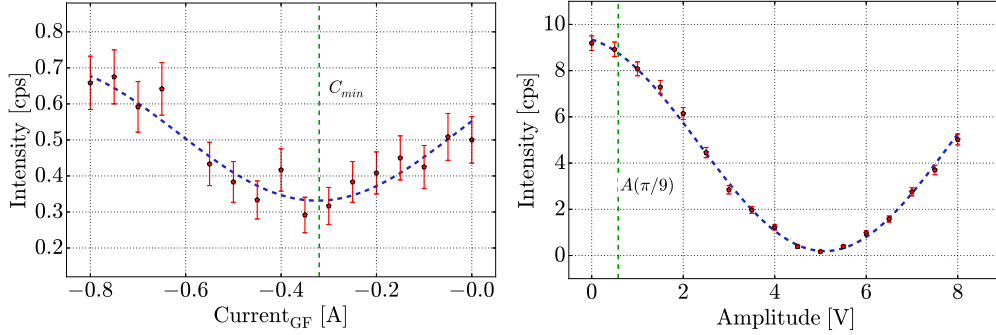


Figure 4.21: *Which-way marker adjustment. Left: Scan of the local guide field of a which-way marker. Right: Scan of the amplitude of the function generator of a which-way marker.*

rotation of $\alpha = \pi/9$ is extracted. The resulting amplitude $A(\pi/9) = 0.58$ V is marked in the graph with a dashed green line. The flip ratio of this device is calculated to be $I_{max}/I_{min} = 44$.

The other three resonance-frequency spin-rotators inside the interferometer are adjusted in the same manner. The spin-rotator in path II , which operates at a frequency of $\omega_{II}/2\pi = 77$ kHz has a flip ratio of $I_{max}/I_{min} = 50$ and the amplitude is set to $A(\pi/9) = 0.57$ V. The spin rotator in path $I+II$ operating at a frequency of $\omega_{I+II}/2\pi = 80$ kHz is set to $A(\pi/9) = 1.83$ V and has a flip ratio of 33. The lower flip ratio and higher amplitude is due to the the spin-rotator being a little shorter than the others, since less space is available for this which-way marker because of the phase shifter PS_R . The spin rotator in path R is set to a frequency of $\omega_R/2\pi = 71$ kHz the amplitude is set to $A(\pi/9) = 0.44$ V with a flip ratio of $I_{max}/I_{min} = 42$.

The resonance-frequency spin-rotator behind the interferometer is adjusted in the same way. Since it is about eight times longer, the expected amplitude is one eighth and the resonance should be much narrower than the resonance of the spin-rotators inside the interferometer. For the guide field scan the amplitude is set to $A = 0.4$ V. The result of the guide field scan is

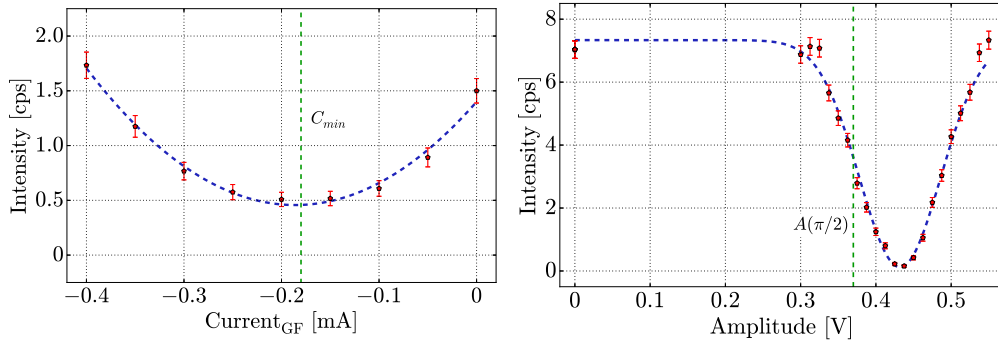


Figure 4.22: Adjustment of the resonance-frequency spin-rotator behind the interferometer. Left: Scan of the local guide field. Right: Amplitude scan of the frequency generator governing the energy compensating resonance-frequency spin-rotator behind the interferometer.

depicted in graph Fig.4.22, with the ideal current $C_{min} = -0.18$ A.

Using the guide field current of $C_{min} = -0.18$ A an amplitude scan is performed. The scan is shown in graph Fig.4.22. Since the resonance is very narrow, so it is best fitted using a Gauss-function. The amplitude for a rotation of $\alpha = \pi/2$ is $A(\pi/2) = 0.37$ V. This spin rotator has a flip ratio of $I_{max}/I_{min} = 61$. The second setting, a spin-rotation of $\alpha = -\pi/2$, is achieved at an amplitude of $A(-\pi/2) = -0.37$ V. This completes the adjustment of the setup for measuring this which-way experiment.

For this experiment several measurements are performed with different phase shifter settings and absorbers in two different positions in the interferometer. A data collection for one set of parameters can take between 24 h and 50 h, depending on the count rates. The final count rates are between 3 cps and 19 cps. Each measurement for one set of parameters is split up in shorter sub-measurements with a duration of 1800 s, in which half of the time an energy compensation set to $\alpha_{EC} = \pi/2$ the other half set to $\alpha_{EC} = -\pi/2$. Between each sub-measurement phase shifter scans are performed fitted and the phase shifter settings are readjusted, to account for possible phase drifts

caused by temperature fluctuations. First a scan of PS_{II} is performed with all resonance-frequency spin-rotators turned off. The intensity at the H1-detector is fitted with a cosine function and the desired phase shifter position is calculated from the fit parameters. The H1-detector is used since the neutron intensity is higher at the H1-detector than the O-detector. In the same manner the position of phase shifter PS_R is adjusted.

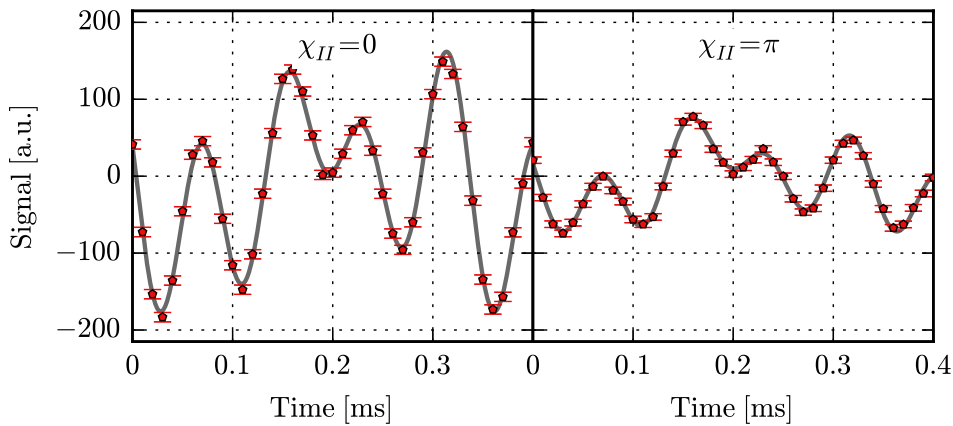


Figure 4.23: *Intensity differences of measurements with the phases set to $\chi_{II} = \chi_R = 0$ on the left hand side, and the phases set to $\chi_{II} = \pi$ and $\chi_R = 0$ on the right hand side. Both fitted with a sum of four sine curves.*

The actual data collection is done by repeating a time-resolved sub-measurement, until the full measurement duration is completed. During a sub-measurement a looped measurement is performed as described in section 4.4.2. This loop is divided into bins. Each count is added to the bin corresponding to the point in time the neutron is detected since the starting time of the loop. The loop duration and the bin width are optimized using the Nyquist-theorem [Nyquist, 1928], with the expected count rates and the frequency resolution of the fast Fourier transform in mind. The loop duration is set to 4 ms and the bin width to $10 \mu\text{s}$. The chosen parameters allow

for a frequency resolution of the Fourier transformation up to 250 Hz, which allows for a clear separation of the frequencies used in the experiment.

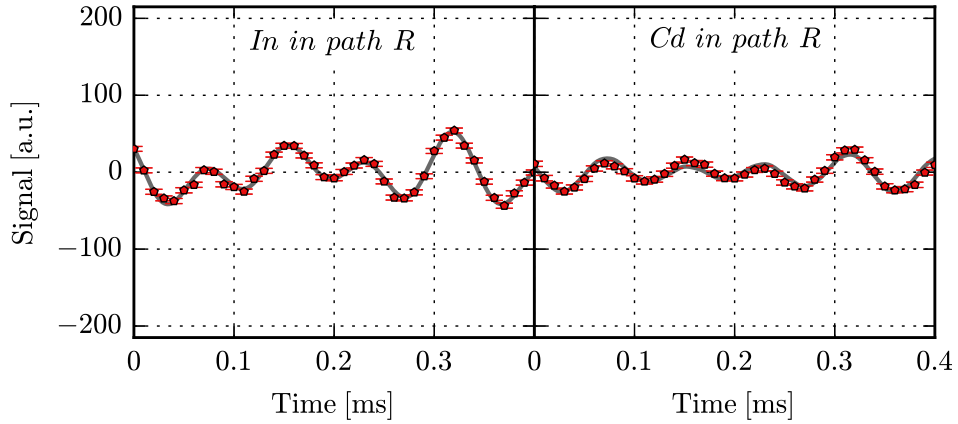


Figure 4.24: *Intensity differences of measurements with the phases set to $\chi_{II} = \pi$ and Indium on path R on the left hand side, and the phases set to $\chi_{II} = \pi$ and Cadmium in path R on the right hand side. Both fitted with a sum of four sine curves.*

The intensity difference $\Delta I = I^+ - I^-$ for the energy compensations $\alpha_{EC}^{\pm} = \pm\pi/2$ is calculated from the data. Typical results for two phase shifter settings are shown in figure Fig.4.23. On the left hand side the phases are set to $\chi_{II} = \chi_R = 0$, while the right hand side shows the intensity difference for the phases set to $\chi_{II} = \pi$ and $\chi_R = 0$. Both are fitted with a sum of four sine curves as given in

$$g(t) = y_0 + \sum_{i=1}^4 A_i \sin(\omega_i t + \phi_i), \quad (4.32)$$

to guide the eye.

The intensity differences for the phase shifters set to $\chi_{II} = \pi$ and $\chi_R = 0$, and absorbers in path R or path $I + II$, are shown in Fig.4.24 and Fig.4.25 respectively.

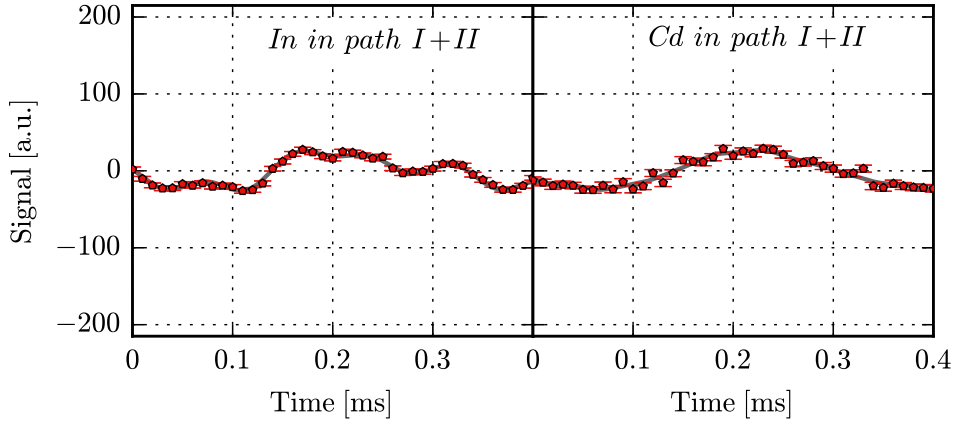


Figure 4.25: *Intensity differences of measurements with the phases set to $\chi_{II} = \pi$ and Indium on path I + II on the left hand side, and the phases set to $\chi_{II} = \pi$ and Cadmium in path I + II on the right hand side. Both fitted with a sum of four sine curves.*

The least square fit converges very slowly and has large standard deviations of the fit parameters. To obtain reasonable good fits to give quantitative fit results, the measurement time would need to be extended beyond manageable durations.

4.6 Data analysis and results

After the data acquisition, the intensity differences are calculated, are normalized to compensate for different measurement duration, and Fourier transformed using a discrete Fourier transformation (FFT) in a standard manner with zero-padding and a Hann window-function. Zero-padding allows for more frequency bins in the same interval of the Fourier spectrum, therefore isolated frequencies can be resolved clearly. The Hann window-function reduces spectral leakage, and therefore the resolution is further increased. The

theoretical prediction for the ideal case with $C_{i,j} = 1$ and the contrast corrected simulation with $C_{i,j} < 1$ yield intensities $I^\pm(t)$, which are normalized, and Fourier transformed in the same way.

First a measurement with both phases set to $\chi_{II} = \chi_R = 0$ is performed. The count rate for this setting is 18.6 counts per second (cps) at the O-detector. The Fourier spectrum of this measurement is depicted in the top row in figure Fig.4.26, with a scheme of the setup. This measurement is used as bases for the normalization of the spectra of all Fourier spectra shown below. The data is normalized in a way that the peaks in the Fourier spectrum corresponding to the frequencies of the spin-rotators in paths I , II , and R are at the height of 1 in arbitrary units. The normalization factor, derived in this way, is also applied to all other sets of data to allow for easy comparison of the peak heights of each Fourier spectrum.

In the first row of figure Fig.4.26 the ideal simulation, the contrast corrected simulation and the measurement show the same peak heights for the respective frequencies. The peaks at frequencies $\Delta\omega_R$, $\Delta\omega_I$, and $\Delta\omega_{II}$ are the same height, while $\Delta\omega_{I+II}$ is twice the height. The height of the peak at frequency $\Delta\omega_{I+II}$ can be explained easily. Every plate acts as a beam splitter dividing the wave functions of each path into a forward and a reflected wave function both reduced in amplitude by a factor of $1/\sqrt{2}$. The marking signal from spin-rotator in path ψ_{I+II} has amplitude, which is larger by a factor of $\sqrt{2}$, which results in twice the peak height at $\Delta\omega_{I+II}$ compared to the other peaks in the first row of figure Fig.4.26. This can also be seen in equation Eq.4.11, since the amplitude of spin-rotator SR_{I+II} is twice the amplitude of the other spin-rotators. This plot also shows that the resonance-frequency spin-rotators are well adjusted. If one spin-rotator would be set to an incorrect angle α , i.e. a wrong amplitude of the frequency generator, the respective peak in the Fourier spectrum would be a different height.

The second row of figure Fig.4.26 shows Fourier spectra of a measurement

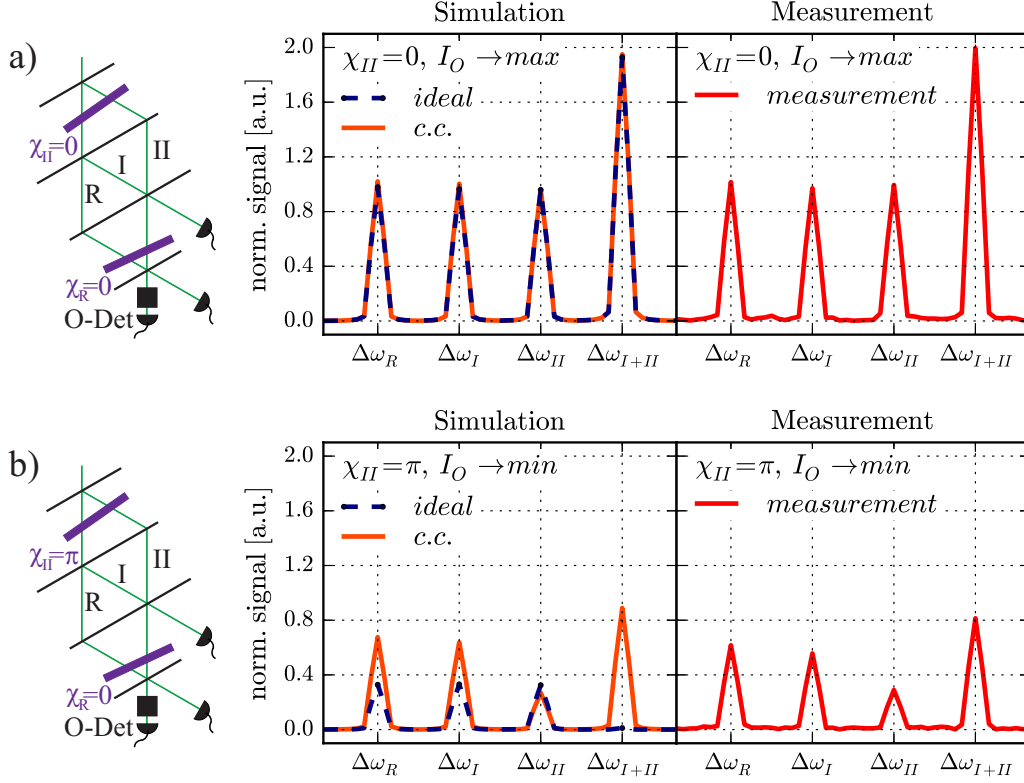


Figure 4.26: *Fourier spectra of the ideal theoretical prediction with $C_{i,j} = 1$ and the contrast corrected simulation with $C_{i,j} < 1$ and measurement, with the experimental setup and parameters. a) The phase shifter PS_{II} is set to $\chi_{II} = 0$. b) The phase shifter PS_{II} is set to $\chi_{II} = \pi$.*

with the phases set to $\chi_{II} = \pi$ and $\chi_R = 0$. Since most of the neutrons of the front loop end up at the H1-detector, the count rate at the O-detector drops as seen from equations Eq.4.11 and Eq.4.12. The intensity at the O-detector drops to 9.1 cps in practice, which is above the level predicted by theory due to the contrast $C_{i,j} < 0$. When the phase of path II is set to $\chi_{II} = \pi$ the amplitudes of all four peaks drop drastically. In the ideal simulation the peaks $\Delta\omega_R$, $\Delta\omega_I$ and $\Delta\omega_{II}$ drop to one third of their initial amplitude but are the same height each. This results from the fact that the interference

terms between the marking signal and the main components from path I and path II interferes destructively due to the phase shift of $\chi_{II} = \pi$

$$I_{I,II}(\chi_I = 0, \chi_{II} = \pi) = |\Psi_I - \Psi_{II}|^2 = 0, \quad (4.33)$$

only the interference of the marking signal of all paths with the main component of path R arrive at the O-detector. This reduces equation Eq.4.9 to,

$$I^\pm = |\Psi_R|^2 + 2 \sum_{i=I,II,R} \Re(\Psi_R^* \Psi_i^\pm) + \mathcal{O}(\alpha_i^2). \quad (4.34)$$

Because of the phase shift $\chi_{II} = \pi$, spin-rotator SR_{I+II} marks the wave function $(\psi_I + e^{i\pi}\psi_{II})/4\sqrt{2} = (\psi_I - \psi_{II})/4\sqrt{2} = 0$, therefore the marking signal is zero and no peak at frequency $\Delta\omega_{I+II}$ is visible. This is also reflected in the calculation in Eq.4.12. In the experiment the wave functions in path $I+II$ do not interfere completely destructively, due to the contrast of $C_{i,j} < 1$. The main components from path I and path R interfere constructively, while the main components from path II and path R interfere destructively, due to the phases of $\chi_{II} = \pi$ and $\chi_R = 0$, which results in different heights of the peaks $\Delta\omega_I$, $\Delta\omega_{II}$, and $\Delta\omega_R$

In Fig. 4.27 and Fig. 4.28 Fourier-spectra of measurements with absorbers in position AB_R and AB_{I+II} respectively are shown. The absorbers used are an Indium foil with a transmission of $T = 0.456$, and a Cadmium foil with a transmission of $T = 0$. When the absorbers are put in AB_R the contribution of the beam in path R is decreased or canceled out respectively.

When the transmission in path R reaches $T_R = 0$, all peaks vanish in the theoretical prediction, since path I and path II interfere destructively and path R is blocked the main component becomes $|\Psi_{E0}|^2 = 0$. Therefore the

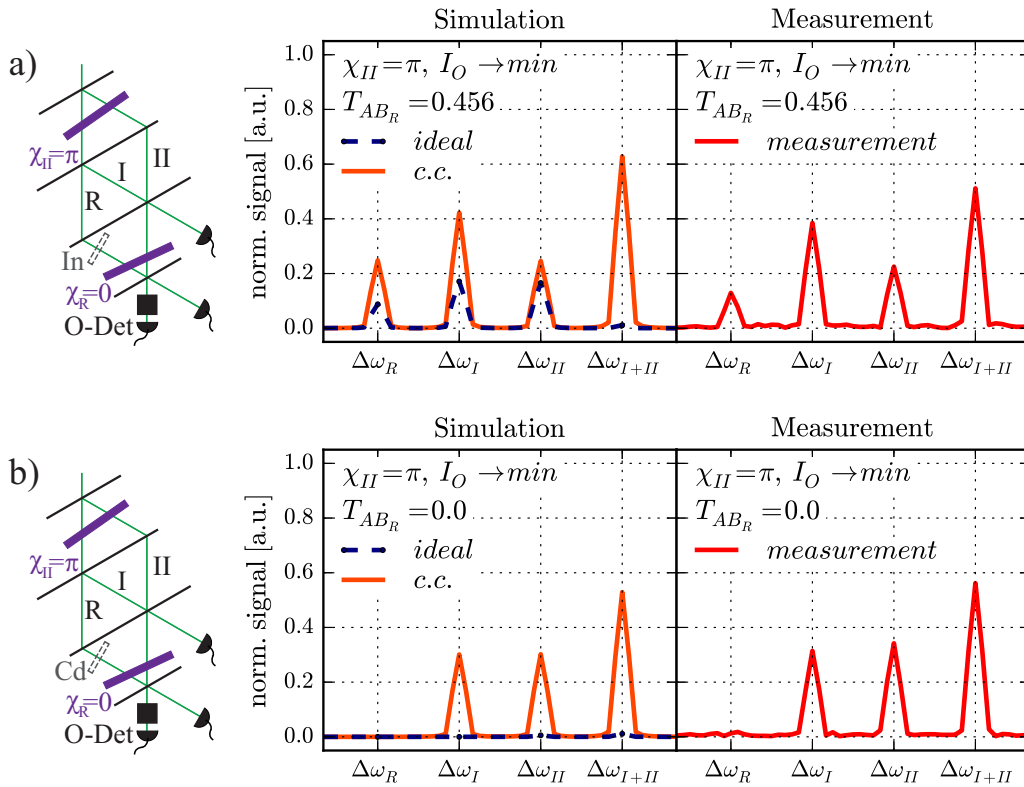


Figure 4.27: Fourier spectra of the ideal theoretical prediction with $C_{i,j} = 1$ and the contrast corrected simulation with $C_{i,j} < 1$ and measurement, with the experimental setup and parameters. a) The phase shifter PS_{II} is set to $\chi_{II} = 0$ and an Indium absorber in path R. b) The phase shifter PS_{II} is set to $\chi_{II} = \pi$ and a Cadmium beam stopper in path R.

intensity in Eq.4.9 becomes $I^\pm = 0$, since

$$I^\pm(T_R = 0) = |\sqrt{T_R} \Psi_R|^2 + 2 \sum_{i=I,II,R} \Re \left(\sqrt{T_R} \Psi_R^* \Psi_i^\pm \right) + \mathcal{O}(\alpha_i^2) \approx 0 \quad (4.35)$$

In the contrast corrected simulation as well as in the measurement peaks at frequencies $\Delta\omega_I$, $\Delta\omega_{II}$, and $\Delta\omega_{I+II}$ remain because of the contrast $C_{i,J} < 1$, that produces leakage from the front loop. The peak at frequency $\Delta\omega_R$ vanishes since both the main component and the marking signal in path R are blocked. For $T = 0.456$ all peaks are reduced in height and the contrast corrected simulation matches the measurement. This demonstrates that the way the simulation is constructed gives a suitable picture of the experiment. This also shows clearly the necessity of the reference beam in path R . In the ideal case no information can be extracted from the Fourier spectra, when the phase shifter PS_{II} is set to $\chi = \pi$, without the beam in path R .

When the absorbers are put in AB_{I+II} , as seen in figure Fig.4.28, the peaks at frequencies $\Delta\omega_I$, $\Delta\omega_{II}$, and $\Delta\omega_{I+II}$ are reduced, or disappear depending on the transmission. The peak at frequency $\Delta\omega_R$ has the same amplitude regardless of the absorber, according to theory, since it arises from the interference of the marking signal and the main component of the beam in path R , which are both unaffected by the absorber.

$$\begin{aligned} I^\pm(T_{I+II} = 0) &= \\ &|\Psi_R| + 2 \sum_{i=I,II} \Re \left(\sqrt{T_{I+II}} \Psi_R^* \Psi_i^\pm \right) + 2\Re \left(\Psi_R^* \Psi_R^\pm \right) + \mathcal{O}(\alpha_i^2) = \quad (4.36) \\ &|\Psi_R| + 2\Re \left(\Psi_R^* \Psi_R^\pm \right) + \mathcal{O}(\alpha_i^2) \end{aligned}$$

Again the contrast corrected simulation matches the measurement. The fluctuation of the height of the peak at frequency $\Delta\omega_R$ results from increased statistical error because of the very low count rates, of about 3 counts per second, since only one path is open.

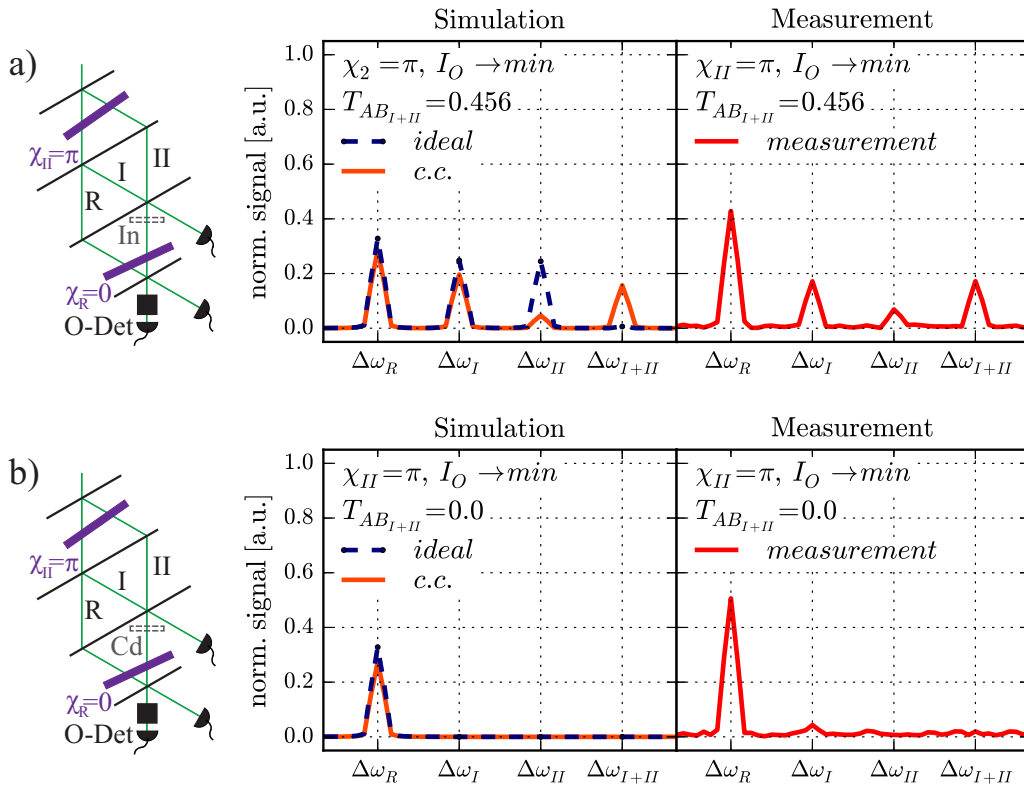


Figure 4.28: Fourier spectra of the ideal theoretical prediction with $C_{i,j} = 1$ and the contrast corrected simulation with $C_{i,j} < 1$ and measurement, with the experimental setup and parameters. a) The phase shifter PS_{II} is set to $\chi_{II} = 0$ and an Indium absorber in path $I + II$. b) The phase shifter PS_{II} is set to $\chi_{II} = \pi$ and a Cadmium beam stopper in path $I + II$.

4.7 Discussion

In this chapter we describe a measurement, utilizing which-way marking of several paths in a double loop interferometer simultaneously. By time-resolving the spin-analyzed signal at the O-detector which-way information has been derived. The second loop provides the reference beam in path R , that allows to probe the outgoing beam from the front loop. This provides information which could not be extracted without it. A theoretical analysis of the experiment is given, that provides a detailed picture of the essential processes involved. This is achieved by calculating the cross terms between marking signal and main components of the beams.

The core concept of our analysis is to attribute the observed intensity modulations to cross-terms, i.e. interference terms between the main components and the which-way marked components of the beams. This formalism provides a simple, yet precise, prediction of the experimental results. The predictions given by our description give quantitative results for a wide variety of experimental settings.

The strength of our approach is best expressed in a comparison to the explanation of a which-way experiment given by Danan [Danan et al., 2013]: In Fig.4.29 two schemes of the laser interferometric experiment are depicted. The nested interferometer (marked by dashed gray line) corresponds to the front loop in our experiment, and the beam reflected by mirror C corresponds to the reference beam in path R in our experiment.

The which-way marking is achieved by small oscillations of the mirrors A , B , C , E , and F at frequencies f_A , f_B , f_C , f_E and f_F respectively. By tuning the phase shift χ in the nested interferometer to π , the peaks at the frequencies f_E and f_F vanish. Note that the height of the other peaks at frequencies f_A , f_B , f_C stay practically the same height.

In their paper the authors make the claims:

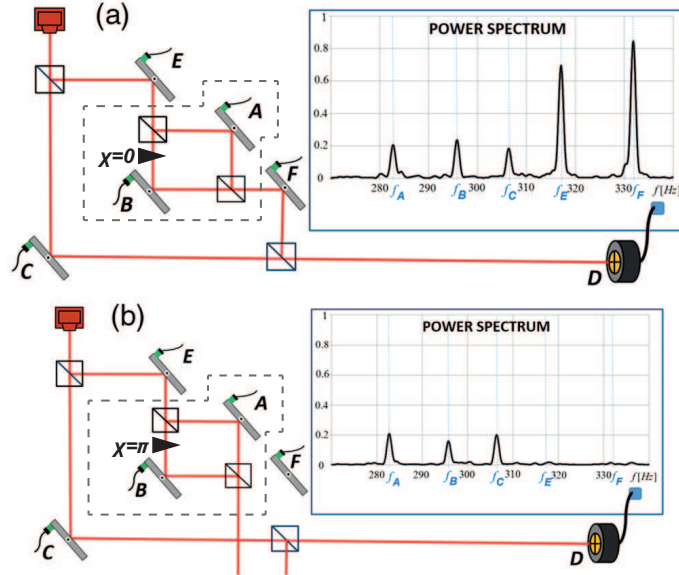


Figure 4.29: *The laser interferometric experiment and power spectra of the intensity modulation at the detector [Danan et al., 2013]. The dashed gray line marks the nested interferometer. a) The phase of the nested interferometer loop is set to $\chi = 0$. b) The phase of the nested interferometer loop is set to $\chi = \pi$.*

- *'The photons do not always follow continuous trajectories. Some of them have been inside the nested interferometer (otherwise they could not have known the frequencies f_A , f_B), but they never entered and never left the nested interferometer, since otherwise they could not avoid the imprints of frequencies f_E and f_F of mirrors E and F leading photons into and out of the interferometer.'*
- *'Only the description with both forward and backward evolving quantum states provides a simple and intuitive picture of pre- and postselected quantum particles.'*

First the absence of the peaks at both frequencies f_E and f_F , is easily explained, with our approach, by the phase shift induced in the nested inter-

ferometer. The which-way signal of mirror E enters the nested interferometer loop and half the signal gets an additional phase of π , which result in the destructive interference of the signal behind the nested interferometer loop. At the mirror F , the main beams coming from mirror A and B interfere destructively, therefore the signal from mirror F becomes zero. The signals from mirrors A and B leak out of the nested interferometer, due to interference with the main component of the beam coming from mirror C , peaks at frequencies f_A and f_B are visible. There is no need for introducing disconnected trajectories, that imply realism at the point of which-way marking, between pre- and post-selection.

Second the change in magnitude of the peaks at frequencies f_A , f_B and f_C is not explained by Danan et al. This can also be easily explained in our description, by the destructive interference occurring in the nested interferometer, only the interference of the which-way signals, which leak out of the nested interferometer, with the main component of the beam reflected at the mirror C remains. The approach chosen by Danan et.al. does not provide as much information as our standard approach using step by step evolution of the wave function, but obscures the workings of this experiment and makes it hard to anticipate the results of this experiment.

The two-state vector formalism does not provide additional information to standard quantum mechanics. Another interesting question is whether or not the two-state vector formalism can give accurate descriptions of delayed choice experiments.

Chapter 5

Conclusion and outlook

In this thesis two fundamental experiments, using polarized perfect-crystal neutron interferometry, have been presented.

In chapter 2 the physical principles of neutron interferometry are described, as well as the methods and devices used for spin preparation, manipulation, and analysis. All elements of the setup, that are essential to understand the experiments presented in thesis, are presented.

In chapter 3 the background to Bell's theorem is given, which includes the historical development. The path that leads from Bell's theorem to an experimentally accessible inequality, as given by CHSH, is outlined, as well as the measurement concept for the neutron interferometric experiment. The crucial and extensive improvements of the setup are presented. The experimental implementation, and the actual measurement are described. The results show clear evidence of the incompatibility of non-contextual hidden variable theories with quantum mechanics: not only a considerably larger violations than previous experiments using perfect-crystal neutron interferometry is achieved, but also in a fraction of the time needed in earlier measurements.

In chapter 4 a measurement scheme for a which-way measurement is presented, using path marking in a double-loop neutron interferometer, where

a reference beam is used to probe another neutron beam. The theoretical treatment is presented, that leads to a simple, yet substantial picture. The method for the simulation for the experiment is explained, that allows to access the measurement results very accurately. The process of designing and fabricating the new double loop interferometer is presented. A new time-resolved measurement system is implemented and successfully used in the measurement. The adjustment procedure of the components needed in the experiment is described, as well as the data handling and analysis. The experimental results agree with the theoretical predictions and simulations, and justify our treatment following the time-development of the wave function.

The presented experiments both study fundamental phenomena of quantum mechanics, but also the capabilities of perfect-crystal neutron interferometry are improved. The setup and new devices, fabricated by the use of a 3D printer, are used in a series of experiments, such as the observation of the quantum Cheshire cat, weak measurements of the Pauli spin operator, "direct" paths reconstruction, or the quantum pigeon hole effect. The 3D-printed spin manipulation devices reduce perturbation on the measurements, can easily be designed for various purposes, and produced with very high accuracy. By using energy as path marking in the new double-loop interferometer and developing a new formalism for calculating quantitative weak values, many future experiments can be feasible. For example, delayed choice experiments, three box paradoxes, and the complete quantum Cheshire cat with delayed choice option. This kind of experiments are very much in reach of the experimental capabilities, but still much effort has to be committed to develop further the capability.

Bibliography

- [Abele, 2008] Abele, H. (2008). The neutron. its properties and basic interactions. *Progress in Particle and Nuclear Physics*, 60(1):1–81.
- [Abutaleb et al., 2012] Abutaleb, M. O., Pushin, D. A., Huber, M. G., Majkrzak, C. F., Arif, M., and Cory, D. G. (2012). Design of remnant magnetization fecov films as compact, heatless neutron spin rotators. *Appl. Phys. Lett.*, 101(182404).
- [Aharonov et al., 1988] Aharonov, Y., Albert, D. Z., and Vaidman, L. (1988). How the result of a measurement of a component of the spin of a spin-1/2 particle can turn out to be 100. *Phys. Rev. Lett.*, 60(14):1351.
- [Aharonov et al., 1964] Aharonov, Y., Bergmann, P. G., and Lebowitz, J. L. (1964). Time symmetry in the quantum process of measurement. *Phys. Rev.*, 134(B1410).
- [Aharonov and Bohm, 1959] Aharonov, Y. and Bohm, D. (1959). Significance of electromagnetic potentials in quantum theory. *Phys. Rev.*, 115:485–491.
- [Aharonov and Casher, 1984] Aharonov, Y. and Casher, A. (1984). Topological quantum effects for neutral particles. *Phys. Rev. Lett.*, 53(4):319–321.

-
- [Aharonov and Vaidman, 1990] Aharonov, Y. and Vaidman, L. (1990). Properties of a quantum system during the time interval between two measurements. *Phys. Rev. A*, 41:11–20.
- [Allen and Eberly, 1975] Allen, L. and Eberly, J. H. (1975). *Optical Resonance and Two-Level-Atoms*. Wiley-Interscience, New York.
- [Allman et al., 1997] Allman, B. E., Kaiser, H., Werner, S. A., Wagh, A. G., Rakhecha, V. C., and J., S. (1997). Observation of geometric and dynamical phases by neutron interferometry. *Phys. Rev. A*, 56(4420).
- [Arndt et al., 1999] Arndt, M. and Nairz, O., Vos-Andreae, J., Keller, C., van der Zouw, G., and Zeilinger, A. (1999). Waveparticle duality of c60 molecules. *Letters to Nature*, 401:680–682.
- [Aspect et al., 1982] Aspect, A., Grangier, P., and Roger, G. (1982). Experimental realization of einstein-podolsky-rosen-bohm gedankenexperiment: A new violation of bell’s inequalities. *Phys. Rev. Lett.*, (49):91.
- [Badurek et al., 1983] Badurek, G., Rauch, H., and Summhammer, J. (1983). Time-dependent superposition of spinors. *Phys. Rev. Lett.*, 51(12):1015–1018.
- [Basu et al., 2001] Basu, S., Bandyopadhyay, S., Kar, G., and Home, D. (2001). Bell’s inequality for a single spin-1/2 particle and quantum contextuality. *Phys. Lett. A*, 279:281.
- [Beer, 1852] Beer, A. (1852). Bestimmung der absorption des rothen lichts in farbigen flssigkeiten. *Annalen der Physik und Chemie*. 86, (86):78–88.
- [Bell, 1964] Bell, J. S. (1964). On the einstein-podolsky-rosen paradox. *Physics (Long Island City, N.Y.)*, (1):195–200.
-

-
- [Berry, 1984] Berry, M. V. (1984). Quantal phase factors accompanying adiabatic changes. *Proc. R. Soc. Lond. A*, 392:45–57.
- [Bertlmann and Zeilinger, 2002] Bertlmann, R. A. and Zeilinger, A. (2002). Quantum [un]speakables, from bell to quantum information. *Springer Verlag, Heidelberg*, (49).
- [Bloch and Sieger, 1940] Bloch, F. and Sieger, A. (1940). Magnetic resonance for nonrotating fields. *Phys. Rev.*, 57:522.
- [Bohm, 1951] Bohm, D. (1951). *Quantum theory*. Prentice-Hall, Englewood Cliffs N.J.
- [Bohm, 1952] Bohm, D. (1952). A suggested interpretation of the quantum theory in terms of "hidden" variables. *Phys. Rev.*, 85:166.
- [Bohm and Aharonov, 1957] Bohm, D. and Aharonov, Y. (1957). Discussion of experimental proof for the paradox of einstein, rosen, and podolsky. *Phys. Rev.*, 108:1070–1076.
- [Bohr, 1928] Bohr, N. (1928). Das quantenpostulat und die neuere entwicklung der atomistik. *Naturwissenschaften*, 16:245.
- [Bohr, 1935] Bohr, N. (1935). Can quantum-mechanical description of physical reality be considered complete? *Phys. Rev.*, E(48):696–702.
- [Bohr, 1949] Bohr, N. (1949). *Discussions with Einstein on Epistemological Problems in Atomic Physics*. Cambridge University Press, United Kingdom.
- [Born, 1971] Born, I. (1971). *The Born-Einstein Letters*. Walker and Company, New York.
- [Bose, 1927] Bose, J. (1927). *Collected physical papers*. Longmans and Green, London.
-

-
- [Clauser et al., 1969] Clauser, J. F., Horne, M. A., Shimony, A., and Holt, R. A. (1969). Proposed experiment to test local hidden-variable theories. *Phys. Rev. Lett.*, 23(15):880–884.
- [Colella et al., 1975] Colella, R., Overhauser, A. W., and Werner, S. A. (1975). Observation of gravitationally induced quantum interference. *Phys. Rev. Lett.*, 34:1472–1474.
- [Cronin et al., 2009] Cronin, a. D., Schmiedmayer, J., and E., P. D. (2009). Optics and interferometry with atoms and molecules. *Rev. Mod. Phys.*, 81:1051.
- [Danan et al., 2013] Danan, A., Farfurnik, D., Bar-Ad, S., and Vaidman, L. (2013). Asking photons where they have been. *Phys. Rev. Lett.*, 111(240402).
- [Davisson and Germer, 1927] Davisson, C. and Germer, L. (1927). Diffraction of electrons by a crystal of nickel. *Phys. Rev.*, 30(6):705.
- [Denkmayr et al., 2017] Denkmayr, T., Geppert, H., Lemmel, H., Mordecai, W., Dressel, J. Hasegawa, Y., and Sponar, S. (2017). Experimental demonstration of direct path state characterization by strongly measuring weak values in a matter-wave interferometer. *Phys. Rev. Lett.*, (118):010402.
- [Denkmayr et al., 2014] Denkmayr, T., Geppert, H., Sponar, S., Lemmel, H., Matzkin, A., Tollaksen, J., and Hasegawa, Y. (2014). Observation of a quantum cheshire cat in a matter-wave interferometer experiment. *Nat Commun*, 5.
- [Dürr et al., 1998] Dürr, S., Nonn, T., and Rempe, G. (1998). Origin of quantum-mechanical complementarity probed by a 'which-way' experiment in an atom interferometer. *Nature*, 395:33–37.
-

-
- [Einstein et al., 1935] Einstein, A., Podolsky, B., and Rosen, N. (1935). Can quantum-mechanical description of physical reality be considered complete? *Phys. Rev.*, 47:777–780.
- [Englert, 1996] Englert, B. G. (1996). Fringe visibility and which-way information: An inequality. *Phys. Rev. Lett.*, 77:2154.
- [Erdösi and Hasegawa, 2011] Erdösi, D. and Hasegawa, Y. (2011). Spin-path entanglement in single-neutron interferometry experiments. In *AIP Conference Proceeding*, number 1384.
- [Erdösi et al., 2013] Erdösi, D., Huber, M., Hiesmayr, B. C., and Hasegawa, Y. (2013). Proving the generation of genuine multipartite entanglement in a single-neutron interferometer experiment. *New Journal of Physics*, 15(2):023033.
- [Filipp et al., 2005] Filipp, S., Hasegawa, Y., Loidl, R., and Rauch, H. (2005). Noncyclic geometric phase due to spatial evolution in a neutron interferometer. *Phys. Rev. A*, 72(2):021602.
- [Filipp et al., 2009] Filipp, S., Klepp, J., Hasegawa, Y., Plonka-Spehr, C., Schmidt, U., Geltenbort, P., and H., R. (2009). Experimental demonstration of the stability of berrys phase for a spin-1/2 particle. *Phys. Rev. Lett.*, 102(030404).
- [Fredrikze and van de Kruijs, 2001] Fredrikze, H. and van de Kruijs, R. W. E. (2001). Calibration of a polarized neutron reflectometer. *Physica B*, 297:143–147.
- [Freedman and Clauser, 1972] Freedman, S. J. and Clauser, J. F. (1972). Experimental test of local hidden-variable theories. *Phys. Rev. Lett.*, (28):938.
- [Geppert et al., 2014] Geppert, H., Denkmayr, T., Sponar, S., Lemmel, H., and y., H. (2014). Improvement of the polarized neutron interferometer
-

- setup demonstrating violation of a bell-like inequality. *Nuclear Instruments and Measurements in Physics Research*, A(00):1–13.
- [Ghose et al., 1991] Ghose, P., Home, D., and Agarwal, G. (1991). *Phys. Lett. A*, 153:403.
- [Greenberger and Yasin, 1998] Greenberger, D. M. and Yasin, A. (1998). Simultaneous wave and particle knowledge in a neutron interferometer. *Phys. Lett. A*, 128(8):391–394.
- [Grigoriev et al., 2004] Grigoriev, S., Kraan, W., and Rekveldt, M. T. (2004). Observation of 4- π periodicity of the spinor using neutron resonance interferometry. *Europhys. Lett.*, 66:164–170.
- [Haroche and Raimond, 2006] Haroche, S. and Raimond, J. M. (2006). *Exploring the Quantum: Atoms, Cavities, and Photons*. Oxford University Press, United Kingdom.
- [Hasegawa et al., 2003] Hasegawa, Y., Loidl, R., Badurek, G., Baron, M., and Rauch, H. (2003). Violation of a bell-like inequality in single-neutron interferometry. *Nature (London)*, 425:45–48.
- [Hasegawa et al., 2010] Hasegawa, Y., Loidl, R., Badurek, G., Durstberger-Rennhofer, K., Sponar, S., and Rauch, H. (2010). Engineering of triply entangled states in a single-neutron system. *Phys. Rev. A*, 81(3):032121.
- [Hasegawa et al., 2001] Hasegawa, Y., Loidl, R., Baron, M., Badurek, G., and Rauch, H. (2001). Off-diagonal geometric phase in a neutron interferometer experiment. *Phys. Rev. Lett.*, 87(7):070401.
- [Hasegawa and Rauch, 2011] Hasegawa, Y. and Rauch, H. (2011). Quantum phenomena explored with neutrons. *New Journal of Physics*, 13(11):115010.
-

- [Heisenberg, 1927] Heisenberg, W. (1927). Über den anschaulichen inhalt der quantentheoretischen kinematik und mechanik. *Zeitschrift fr Physik*, 43(3-4):172–198.
- [Herzog et al., 1995] Herzog, T. J., Kwiat, P. G., Weinfurter, H., and Zeilinger, A. (1995). Complementarity and the quantum eraser. *Phys. Rev. Lett.*, 75(23):3034–3037.
- [Holm, 2013] Holm (2013). *Siliciumbearbeitung Andrea Holm GmbH*. Gigerenz 1,84367 Tann, Germany.
- [Jönsson, 1961] Jönsson, C. (1961). Elektroneninterferenzen an mehreren knstlich hergestellten feinspalten. *Zeitschrift fur Physik*, 161(4):454474.
- [Kennard, 1927] Kennard, E. H. (1927). Zur quantenmechanik einfacher bewegungstypen. *Zeitschrift fr Physik*, 44(4).
- [Klein and Opat, 1976] Klein, A. G. and Opat, G. I. (1976). Observation of 2p rotations by fresnel diffraction of neutrons. *Phys. Rev. Lett.*, 37:238–240.
- [Klepp et al., 2014] Klepp, J., Sponar, S., and Hasegawa, Y. (2014). Fundamental phenomena of quantum mechanics explored with neutron interferometers. *Progress of Theoretical and Experimental Physics*, 8:082A01.
- [Kwiat et al., 1995] Kwiat, P. G., Mattle, K., Weinfurter, H., Zeilinger, A., Sergienko, A. V., and Shih, Y. (1995). New high-intensity source of polarization-entangled photon pairs. *Phys. Rev. Lett.*, (75):4337.
- [Laplace, 1814] Laplace, P.-S. (1814). *Essai philosophique sur les probabilitis*. Paris.
- [Lee et al., 1998] Lee, W.-T., Motrunich, O., Allman, B. E., and Werner, S. A. (1998). Observation of scalar aharonov-bohm effect with longitudinally polarized neutrons. *Phys. Rev. Lett.*, 80:3165.
-

-
- [Lemmel, 2006] Lemmel, H. (2006). Confinement induced neutron phase.
- [Mermin, 1990] Mermin, N. D. (1990). Simple unified form for the major no-hidden-variables theorems. *Phys. Rev. Lett.*, 65(27):3373–3376.
- [Mermin, 1993] Mermin, N. D. (1993). Hidden variables and the two theorems of John Bell. *Rev. Mod. Phys.*, 65(3):803–815.
- [Mezei, 1972] Mezei, F. (1972). Neutron spin echo: A new concept in polarized thermal neutron techniques. *Zeitschrift für Physik*, 255(2):146–160.
- [Nairz et al., 2003] Nairz, O., Arndt, M., and Zeilinger, A. (2003). Quantum interference experiments with large molecules. *Am. J. Phys.*, 71:319.
- [Nyquist, 1928] Nyquist, H. (1928). Certain topics in telegraph transmission theory. *Trans. AIEE*, 47:617–644.
- [Rabi, 1937] Rabi, I. (1937). Space quantization in a gyrating magnetic field. *Phys. Rev.*, 51:652.
- [Ramsey, 1940] Ramsey, N. (1940). A new molecular beam resonance method. *Phys. Rev.*, 76:996.
- [Rauch et al., 2002] Rauch, H., Lemmel, H., Baron, M., and Loidl, R. (2002). Measurement of a confinement induced neutron phase. *Nature*, 417(6889):630–632.
- [Rauch and Suda, 1974] Rauch, H. and Suda, M. (1974). Intensitätsberechnung für ein Neutronen-Interferometer. *Phys. Stat. Sol.*, a(25):495.
- [Rauch et al., 1974] Rauch, H., Treimer, W., and Bonse, U. (1974). Test of a single crystal neutron interferometer. *Phys. Lett. A*, 47(5):369 – 371.
- [Rauch and Werner, 2000] Rauch, H. and Werner, S. (2000). *Neutron Interferometry*. Clarendon Press, Clarendon Press, Oxford.
-

-
- [Rauch et al., 1975] Rauch, H., Zeilinger, A., Badurek, G., Wilfing, A., Bauspiess, W., and Bonse, U. (1975). Verification of coherent spinor rotation of fermions. *Phys. Lett.*, 54(A):425.
- [Sakurai, 1993] Sakurai, J. J. (1993). *Modern Quantum Mechanics*. Prentice Hall, United States.
- [Scully and Suhail Zubairy, 1997] Scully, M. O. and Suhail Zubairy, M. (1997). *Quantum optics*. University Press, Oxford, United Kingdom.
- [Sponar et al., 2015] Sponar, S., Denkmayr, T., Geppert, H., Lemmel, H., Matzkin, A., Tollaksen, J., and Hasegawa, Y. (2015). Weak values obtained in matter-wave interferometry. *Physical Review*, A(92):062121.
- [Sponar et al., 2010] Sponar, S., Klepp, J., Loidl, R., Filipp, S., Durstberger-Rennhofer, K., Bertlmann, R. A., Badurek, G., Rauch, H., and Hasegawa, Y. (2010). Geometric phase in entangled systems: A single-neutron interferometer experiment. *Phys. Rev. A*, 81(4):042113.
- [Suda, 2005] Suda, M. (2005). *Quantum interferometry in phase space*. Springer Science, Berlin.
- [Summhammer et al., 1983] Summhammer, J., Badurek, G., Rauch, H., Kischko, U., and Zeilinger, A. (1983). Direct observation of fermion spin superposition by neutron interferometry. *Phys. Rev. A*, 27(5):2523–2532.
- [Summhammer et al., 1987] Summhammer, J., Rauch, H., and Tuppinger, D. (1987). Stochastic and deterministic absorption in neutron-interference experiments. *Phys. Rev. A*, 36(9):44447.
- [Tittel et al., 1998] Tittel, W., Brendel, J., Zbinden, H., and Gisin, N. (1998). Violation of bell inequalities by photons more than 10 km apart. *Phys. Rev. Lett.*, (81):3563.
-

-
- [Tonomura, 1987] Tonomura, A. (1987). Applications of electron holography. *Rev. Mod. Phys.*, 59:639.
- [Vaidman, 2013] Vaidman, L. (2013). Past of a quantum particle. *Phys. Rev. A*, 87(052104).
- [Waegell et al., 2017] Waegell, M., Denkmayr, T., Geppert, H., Ebner, D., Jenke, T., Hasegawa, Y., Sponar, S., Dressel, J., and Tollaksen, J. (2017). Confined contextuality in neutron interferometry: Observing the quantum pigeonhole effect. *arXiv*, (1609.06046).
- [Walborn et al., 2002] Walborn, S. P., Terra Cunha, M. O., Pdua, S., and Monken, C. H. (2002). Double-slit quantum eraser. *Phys. Rev. A.*, 65(3):033818.
- [Watanabe, 1955] Watanabe, S. (1955). Symmetry of physical laws. part iii. prediction and retrodiction. *Reviews of Modern Physics*, 27(2):179–186.
- [Weihs et al., 1998] Weihs, G., Jennewein, T., Simon, C., Weinfurter, H., and Zeilinger, A. (1998). Violation of bells inequality under strict einstein locality conditions. *Phys. Rev. Lett.*, (81):5039.
- [Werner et al., 1975] Werner, S. A., Colella, R., Overhauser, A. W., and Eagen, C. F. (1975). Observation of the phase shift of a neutron due to precession in a magnetic field. *Phys. Rev. Lett.*, 35(16):1053–1055.
- [Werner and Klein, 2010] Werner, S. A. and Klein, A. G. (2010). Observation of aharonovbohm effects by neutron interferometry. *Journal of Physics A: Mathematical and Theoretical*, 43(35):354006.
- [Wheeler and Zurek, 1983] Wheeler, J. A. and Zurek, W. H. (1983). *Quantum Theory and Measurement*. Princeton University Press, New Jersey, USA.
-

-
- [Wilton, 2014] Wilton, L. V. (2014). *Quantum Mechanics in Everyday Life*. Rhodium Inc., Cambridge United States.
- [Zawisky et al., 2009] Zawisky, M., Springer, J., Farthofer, R., and Kuetgens, U. (2009). A large-area perfect crystal neutron interferometer optimized for coherent beam-deflection experiments: Preparation and performance. *Nucl. Instr. Meth.*, A1.
-

Curriculum Vitae

Hermann Geppert-Kleinrath

Address

Frauenberg, 25
3500-Krems
Austria

Phone: +43 650 205 205 9

Email: hermann.geppert@gmx.at

Personal details

Gender: Male

Date of Birth: 13. of February, 1986

Place of Birth: Krems, Austria

Citizenship: Austria

Spouse: Dr. DI Verena Geppert-Kleinrath

Education

- 2012-2017 TU Wien
 Doctor of Engineering Sciences in Physics, 2017
- 2004-2012 TU Wien
 Master in Physics
- 2000-2004 PORG Krems
 Graduation (Matura)

Languages

German
English
Latin

List of publications

T. Denkmayr, Geppert, H., H. Lemmel, W. Mordecai, and Y. Sponar S. Dressel J. Hasegawa. Experimental Demonstration of Direct Path State Characterization by Strongly Measuring Weak Values in a Matter-Wave Interferometer. In: Phys. Rev. Lett. 118 (2017), p. 010402.

M. Waegell, T. Denkmayr, Geppert, H., D. Ebner, T. Jenke, Y. Hasegawa, S. Sponar, J. Dressel, and Tollaksen J. Confined Contextuality in Neutron Interferometry: Observing the Quantum Pigeonhole Effect. In: arXiv

1609.06046 (2017).

S Sponar, T Denkmayr, H Geppert, and Y Hasegawa. Fundamental Features of Quantum Dynamics Studied in Matter-Wave Interferometry-Spin Weak Values and the Quantum Cheshire-Cat. In: *Atoms* 4.1 (2016), p. 11.

S Sponar, T Denkmayr, H Geppert, H Lemmel, A Matzkin, J Tollaksen, and Y Hasegawa. Full determination of complex weak values of a spin component of a spin-1/2 particle obtained in neutron-optical experiments. In: *Physical Review A* 92.6 (2015), p. 062121.

T Denkmayr, H Geppert, S Sponar, H Lemmel, A Matzkin, J Tollaksen, and Y Hasegawa. Observation of a quantum Cheshire Cat in a matter-wave interferometer experiment. In: *Nature Communications* 5.4492 (2014).

H Geppert, T Denkmayr, S Sponar, H Lemmel, and Y Hasegawa. Improvement of the polarized neutron interferometer setup demonstrating violation of a Bell-like inequality. In: *Nuclear Instruments and Methods in Physics Research Section A* 763 (2014), pp. 417423.

S Sponar, J Klepp, K Durstberger-Rennhofer, C Schmitzer, H Bartosik, H Geppert, M Both, G Badurek, and Y Hasegawa. High-efficiency manipulations of triply entangled states in neutron polarimetry. In: *New Journal of Physics* 14.053032 (2012).

H. Geppert, T. Denkmayr, S. Sponar, H. Lemmel, T. Jenke, and Y. Hasegawa "Which-way measurement in a double-loop neutron interferometer." In preparation. (2017)
